EXPERIMENTAL INVESTIGATION OF THE TURBULENT AXISYMMETRIC JET

BY

STEVEN P. CAPP

A DISSERTATION SUBMITTED TO THE FACULTY
OF THE GRADUATE SCHOOL OF THE STATE UNIVERSITY
OF NEW YORK AT BUFFALO IN PARTIAL FULFILLMENT
OF THE REQUIREMENTS FOR THE DEGREE OF
DOCTOR OF PHILOSOPHY

MAY 1983

DEDICATION

TO MY PARENTS

(OH, AND TO YOU TOO DEXTER)

TABLE OF CONTENTS

Acknowledgements		i
Abstract		ii
List of Figures		iii
List of Tables		vi
Chapter		Page
1	Introduction	1
2	Implications of the Equations of Motion for the Turbulent Axisymmetric Jet	4
	2.1 Review of Field and Deficiencies of Current Data	4
	2.2 Governing Equations for the Turbulent Jet in an Infinite Environment	6
	2.3 Volume Entrainment and Momentum Flux	13
	2.4 Derivation of Momentum Constraint	28
	2.5 Momentum Loss in a Confined Jet	36
	2.6 Summary of Basic Considerations	45
3	Experimental Equipment	47
	3.1 Jet Facility	47
	3.2 Optical and Signal Processing Equipment	52
4	The Jet Measurements	59
	4.1 Centerline Velocity Values	59
	4.2 The Mean Velocity Profile	67
	4.3 The Turbulent Velocity Fluctuations	70
	4.4 The Momentum Constraint Evaluation	74
	4.5 The Effect of the Return Flow	74
	4.6 Concluding Statements on the Experimental Results	81

5 Introduction to Part II: Analysis of the LDA Technique 82

6 The LDA Hardware 85

6.1 Fringe Model for Dual Beam Optical System 85

6.2 Hardware Configuration of Burst Processor 90

6.3 Hardware Configuration of Buffer and Coincidence Filter 95

7 The Measurement of Flow Properties by the LDA 101

7.1 Particle Effects on Measurements 101

7.2 Selection of Optical Package 106

7.3 Statistical Dependence of Flow Field and Particle Arrival Rates - The Problem of Bias 108

7.4 Bias Due to Dropout and Correction with Frequency Shift 116

7.5 Hardware Accuracy of Burst Time and Doppler Frequency 122

7.6 Hardware Accuracy of Sample Interval 132

8 Validation of Measurement Techniques 136

8.1 Software Programming Considerations and Relative Errors of Statistical Estimates 136

8.2 Particle Path Lengths in Optical Probe Volume 141

8.3 Probability Distribution Function for Particle Path Length in Laminar Flow 149

8.4 Probability Distribution Function for Fringe Count in Turbulent Flow 155

8.5 Software Verification Techniques 179

8.6 Summary and Conclusions 179

References 182

ACKNOWLEDGMENTS

I would like to use this opportunity to thank all who have helped me with this investigation and throughout graduate studies, the most important of them being my advisor, William K. George. I also wish to thank Bob Suhoke Jr. for his irreplacable contributions in the lab. Of course, I must admit it was our secretary, Eileen Graber, who was really responsible for getting anything done in the lab.

This research was supported by the Air Force Office of Scientific Research under contract number F4962080C0053 and the National Science Foundation under grant number ATM 8023699A01.

ABSTRACT

This work presents the results of a study of the turbulent axisymmetric jet which was initiated to resolve the unanswered questions first introduced by Baker (1980). Data taken with a laser Doppler anemometer using the burst-processor technique is reported and has been found to be in excellent agreement with the theoretical predictions of Seif (1981). Based upon a simple model for the back flow of a jet in a finite environment, it is concluded that the major source of error in previous experiments has been the flow facility itself and not primarily the measurement technique utilized.

The jet data is used to gain further insight into the appropriate methods for correctly utilizing the burst-processor. Following a brief description of hardware design and construction, the major difficulties in the implementation of counter measurements are reviewed. The concept of software verification is then introduced. The probability distribution function of the particle path length through the measuring volume is derived and its impact on verification techniques are explored. Procedures are described to give a rough guide for judging signal quality and particle seeding characteristics. Finally, a methodology is suggested for the programming of data acquistion routines.

LIST OF FIGURES

2.2.1	Coordinate System for Axisymmetric Jet	8
2.3.1	Comparison of Polynominal and Gaussian Fit/Mean Axial Velocity Profile	18
2.3.2	Comparison of Pllynominal and Gaussian Fit/Momentum Flux Integral	20
2.3.3	Comparison of Polynominal and Gaussian Fit/Volume Flux Integral	22
2.3.4	Local Turbulent Intensities and Intermittency Factor/Wygnanski and Fiedler - 1969	23
3.1.1	The Jet Facility	48
3.1.2	Jet Exit Profile	51
3.1.3	The Jet Enclosure	53
3.2.1	Optical Package	54
3.2.2	Signal Processing Equipment	57
4.1.1	Centerline Velocity Decay	61
4.1.2	Effect of Virtual Origin on Data of Wygnanski and Fiedler Modification of Centerline Decay Rate	64
4.1.3	Values for Centerline Decay Rate	66
4.2.1	Mean Velocity Profile	68
4.3.1	Axial Component of Reynolds Stress	72
4.3.2	Azimuthal Component of Reynolds Stress	73
4.5.1	Confined Jet Correction to Centerline Data Wygnanski and Fiedler (1969)	79
4.5.2	Confined Jet Correction to Centerline Data Present Investigation	80
6.1.1	Intersecting Laser Beams and Fringe Pattern	87
6.1.2	Effect of Frequency Shift on Fringe Pattern	89
6.2.1	Block Diagram of Disa Counter	91

6.2.2	Electronic Conditioning of Doppler Signal	93
6.3.1	Coincidence Filter Board Block Diagram	98
7.2.1	Optical Probe Volume	107
7.3.1	Velocity Signal for Burst Type LDA	109
7.4.1	Angular Bias	119
7.5.1	Digital Clock Measurement Error	124
7.5.2	Percentage Clock Error vs Doppler Frequency	127
7.5.3	Counter Truncation of Burst Time	129
7.5.4	Percentage Truncation Error vs Doppler Frequency	131
7.6.1	Sample Interval Floating Clock	134
7.6.2	Digital Clock Measurement Error - Sample Interval	135
8.1.1	Variation of Integral Scale Across Profile	138
8.2.2	Probe Volume Coordinate System	143
8.3.1	Probability Distribution Function of λ in a Laminar Flow	153
8.4.1	Theoretical Prediction of Fringe Count Histogram Variation with Higher Turbulence Intensity Levels	159
8.4.2	Theoretical Prediction of Fringe Count Distribution Function Shift from 1-D to 2-D Turbulent Flow Field	159
8.4.4	Probabiltiy Distribution of Fringe Count Theoretical and Experimental Results	164
8.4.5	Probability Distribution of Fringe Count Variation Across Jet Axis for Two Channel Data	165
8.4.6	Fringe Count Overflow	167
8.4.7	Fringe Count vs Doppler Frequency	170
8.5.1	Particle Concentration Seen by Counter	174

8.5.2 Residence Time-Velocity Correlation Coefficient 177

8.5.3 Residence Time-Residence Time Correlation Coefficient 178

LIST OF TABLES

2.3.1	Entrainment Parameters for Gaussian and Polynomial Functions	27
2.4.1	Momentum Balance	35a
3.1.1	Jet Facility Parameters	50
3.2.1	Parameters of Beam Intersection Intersection Volume	56
4.5.1	Parameters of Experimental Enclosure	76
6.3.1	Validation Rate Versus Data Rate	96
7.1.1	Particle Size Cut-off Frequencies	104
7.2.1	Physical Properties of Optical Geometry	105a
7.2.2	Calibration Properties of Optical Geometry	105b

Chapter 1: Introduction

This dissertation addresses two different areas of interest in the subject of experimental fluid mechanics. Its primary objective originated from the Ph.D. dissertation of C. Bruce Baker (1980). Baker's study of a numerical model for the heated axisymmetric turbulent jet revealed a serious error in previously accepted experimental data describing the mean velocity field. In Seif's (1981) numerical computations, the coefficients of the models for the turbulent stresses were selected from only grid turbulence and homogeneous strain experiments. His application of these models to the axisymmetric jet also showed significant deviation from current available measurements. In a collaborative effort, George, Seif and Baker (1982) explored the possible causes for the measurement errors. At the time this experimental project began, it was believed that the problems could be attributed to inherent difficulties in constant temperature anemometry (CTA or hot-wire) techniques in highly turbulent flows. Since laser Doppler anemometry (LDA) methods are not subject to the same limitations, they were selected to measure the jet.

The second subject of interest involves the correct application of the burst-processor as a measuring device in turbulent flows. The use of LDA equipment is increasing

steadily since this is the only hardware capable of taking measurements in many critical areas of research. Combustion, rotating machinery, turbine and internal combustion engine studies are major areas of interest where only the LDA can be of use for velocity measurements. Although LDA hardware is a very powerful and versatile tool, it is also a tool which can be difficult to successfully implement. The purpose of the second part of this dissertation is to present possible indicators by which an experimenter may simply demonstrate that his measurement program has been correctly executed. It must be noted that the difficulties in reconstructing the sources of error in the original jet experiments stimulated the motivation for this second half of the dissertation.

The first part of the dissertation deals with the problem of the axisymmetric turbulent jet. The second chapter introduces the mathematics and physics of the jet problem. It essentially provides the framework on which the data will be analyzed. Although the reader is undoubtedly familiar with this development, it is suggested that he pay close attention to this chapter. After a brief review of the literature, the basic equations for the jet are then reviewed in section 2.2. Next, implications of mass and momentum transport across a profile are discussed. In order to more accurately determine the momentum constraint, second order terms have been retained as shown in section 2.4.

These terms are normally neglected in most works addressing the subject, but have been shown by George et al. (1982) to be significant. The concept of an enclosed jet is also introduced here and the effect of a finite environment is explored. It is the finite environment which is believed to be the leading cause for the failure of the experimental measurements of other authors to satisfy the momentum constraint.

The third chapter documents the details of the jet facility. In addition, it contains specifications on the LDA equipment. Details on the computer system used for data collection and processing are also given here.

The fourth and last chapter of part I presents and analyzes implications of the LDA measurements. First and second moments are used to examine the momentum constraint and the difference between jets in finite or in infinite environments. Leading error sources in the measurement program are then identified. The study of the turbulent jet is concluded with a summary of what has been learned and what remains to be learned. A future experimental program is also suggested.

PART I: THE JET INVESTIGATION

Chapter 2: Implications of the Equations of Motion for the Turbulent Axisymmetric Jet

Section 2.1: Review of Field and Deficiencies of Current Data

Introductory background for anyone interested in the turbulent jet can be found in the fluid dynamic texts of Hinze (1975), Tennekes and Lumley (1972), and Schlichting (1968). Early investigations in the axisymmetric jet using pitot and total head tubes include the work of Reichart (1951), Corrsin (1943), Corrsin and Uberoi (1949, 1951), Hinze and van der Hegge Zijnen (1949), and Corrsin and Kistler (1954). The most comprehensive investigation published to date is the 1969 work of Wygnanski and Fiedler. The measurements taken using a linearized constant temperature hot-wire anemometer consisted of the following data: mean velocities, Reynold's stresses, third and fourth moments of the velocity field, correlations, time and length scales, frequency spectra and convection velocities. Following publication of this work, subsequent literature has accepted these results. Within the past decade, reports concerning the jet have focused in different areas. Concerned with either higher-order numerical modeling or large-scale structures, few investigators have bothered to seriously question the basic flow field measurements.

Fortunately, researchers perfecting new measurement techniques have turned to the jet to contrast the performances of CTA and or LDA methods. From these sources,

more information can be obtained concerning the flow field. Rodi (1975) investigated a new calibration technique for hot wires in the jet. Abbiss et al. (1976) used a photon correlator in combination with a Doppler difference optical layout. Reed's work (1977) also involved the use of LDA instrumentation in the jet. Rodi's work is the only printed material of experimental data which has challenged the results of Wygnanski and Fiedler. The lack of criticism present in the literature indicates the data of Wygnanski and Fiedler has been accepted by the scientific community.

Curiously enough, the most serious deficiency in the current experimental data was highlighted in a theoretical work. Baker's thesis (1980) studied the evolution of a hot axisymmetric jet into a turbulent plume. Using the eddy viscosity hypothesis, similarity scaling, and perturbation and asymptotic techniques, he presented a unified theory for the buoyant jet. During the course of his investigation, it was discovered that the data of Wygnanski and Fiedler failed to account for approximately 40% of the momentum. The data of Rodi was missing 16% of the source momentum. The work of Seif (1981) in two-equation modeling and Reynolds stress modeling produced numerical results that throws further doubts on existing measurements. In an unpublished paper critically examining available data, George, Seif, and Baker (1982) sought to identify possible sources of error. Hot wire calibration errors and non-uniform exit profiles are

facility dependent, therefore these two problems were not considered the primary cause of error since most of the existing data from different sites is in close agreement. The authors also examined the development of the flow as it leaves the jet exit. Analysis of measurements of Tutu and Chevray (1977), Khwaja (1980), and Nee (1983) reveal that in this region at least 97% of the equivalent top-hat momentum was conserved. The error was finally attributed to calibration difficulties and to nonlinear contamination by the high turbulent intensities of the flow.

To summarize, the data which has been accepted to date is seriously in error. In any record of experimental jet data, it should be clearly demonstrated that the equations of motion are satisfied and that momentum is conserved. The failure to verify the measurements in this manner has been a key factor in the failure to detect the inconsistency of the data. In section 2.5 of this chapter, a development is presented which clearly indicates the problem can in large part be attributed to flow facility related difficulties.

Section 2.2: Governing Equations for the Turbulent Jet in an Infinite Environment

The axisymmetric turbulent jet is a classic flow problem, displaying all the basic physical behavior patterns of turbulent flow. It is distinquished by the simple form to which the equations of motion reduce and the ease with

which it may be created in the laboratory. Figure 2.1.1 defines the coordinate system and nomenclature adopted in this paper. Far downstream of the jet exit, the flow can be treated as a point source of momentum. The location of the ideal source is defined as the virtual origin and the axial coordinate with respect to this point is defined as x. In general, the virtual origin and the physical location of the jet exit are not the same, the distance from the jet exit being denoted by x'. The distance between the two origins is x_o. This quantity is positive if the virtual origin is downstream of the jet exit. The radial coordinate is r. Assuming that there is no swirl, the derivatives of mean quantities with respect to the azimuithal coordinate and the mean aximuthal velocity are zero. For convenience the jet is placed in a quiescent medium so that the pressure gradient and velocity approach zero as r approaches infinity. We consider only isothermal Newtonian fluids in velocity ranges low enough so that the fluid may be considered inmcompressible.

The derivation of the equations governing this flow is reviewed below. First, the Reynolds decomposition is performed on the Navier-Stokes equations. The result for the continuity equation is

$$\frac{\partial \underline{U}}{\partial x} + \frac{1}{r}\frac{\partial (r\underline{V})}{\partial r} = 0 \qquad (2.2.1)$$

For high Reynolds number, the viscous terms in the

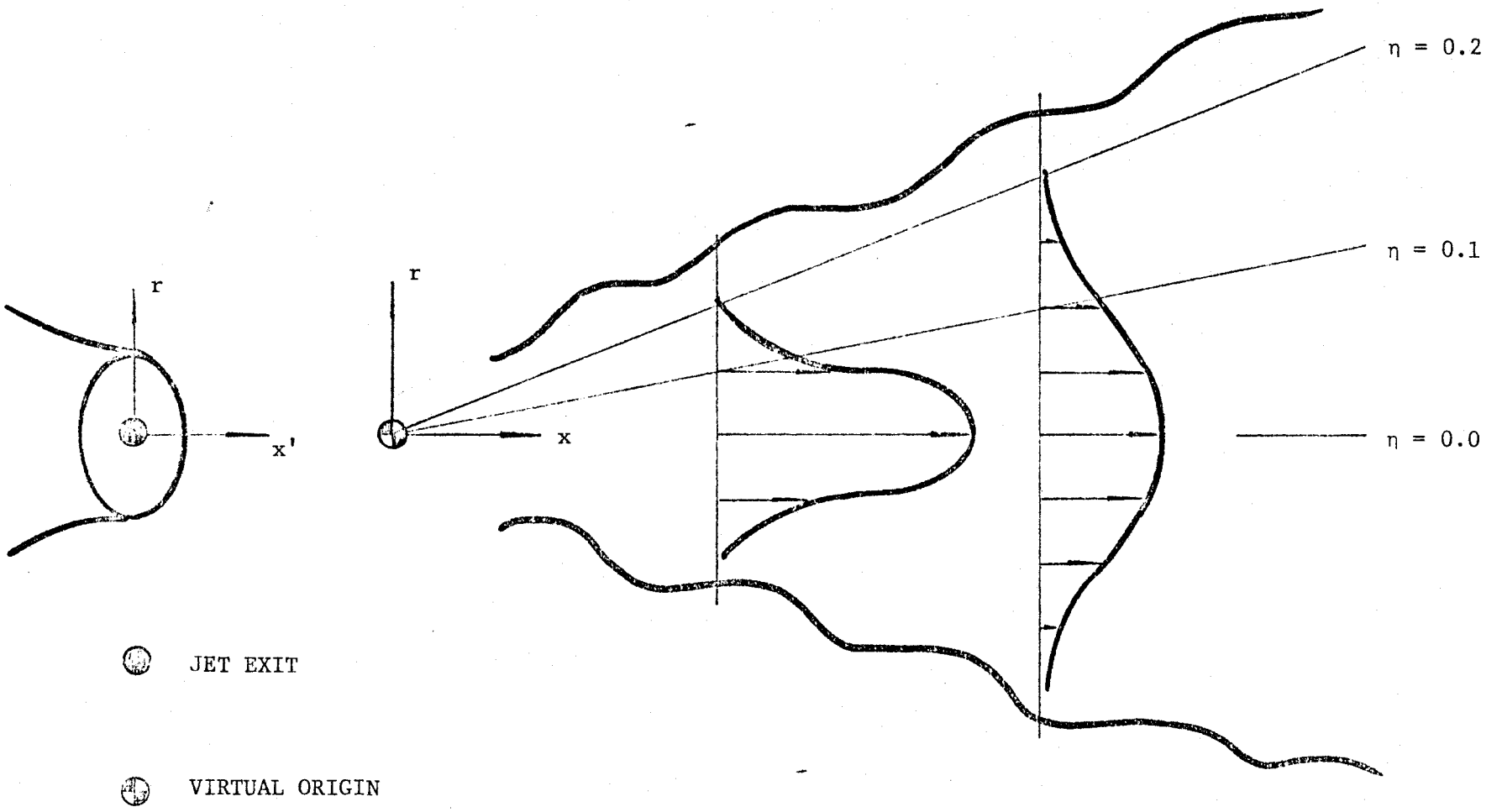

FIGURE 2.2.1

COORDINATE SYSTEM FOR AXISYMMETRIC JET

remaining equations of motion can be ignored. The axial component of the momentum equation is

$$U\frac{\partial U}{\partial x} + V\frac{\partial U}{\partial r} = \frac{-1}{\rho}\frac{\partial P}{\partial x} - \frac{1}{r}\frac{\partial (r\overline{uv})}{\partial r} + \frac{\partial \overline{u^2}}{\partial x} \qquad (2.2.2)$$

The viscous terms in the radial equation are also ignored. This equation is further simplified by an order of magnitude analysis. Lower order terms are neglected to give

$$0 = \frac{-1}{\rho}\frac{\partial P}{\partial r} - \frac{1}{r}\frac{\partial (r\overline{v^2})}{\partial r} - \frac{\overline{w^2}}{r} \qquad (2.2.3)$$

This equation is now integrated to obtain an expression for the pressure term. Substituting this relation into the mean momentum equation for the axial component produces

$$U\frac{\partial U}{\partial x} + V\frac{\partial U}{\partial r} = \frac{-1}{r}\frac{\partial (r\overline{uv})}{\partial r} + \frac{\partial}{\partial x}(\overline{v^2} - \overline{u^2}) + \frac{\partial}{\partial x}\int_r^\infty \frac{(\overline{w^2} - \overline{v^2})}{r'}\,dr' \qquad (2.2.4)$$

This equation is normally further reduced by dropping the axial gradients of the turbulent stresses which can be shown to be of second order. This simpler form is the equation most commonly found in literature.

$$U\frac{\partial U}{\partial x} + V\frac{\partial U}{\partial r} = \frac{-1}{r}\frac{\partial (r\overline{uv})}{\partial r} \qquad (2.2.5)$$

The equations of motion have been reduced to a simple form and only the boundary conditions remain to be specified. They are as follows

$$U(x,r) = 0 \qquad \text{as } r \text{ approaches } \infty$$

$$\overline{uv}(x,r) = 0 \qquad \text{at } r=0 \text{ and as } r \text{ approaches } \infty \qquad (2.2.6)$$

$$V(x,r) = 0 \qquad \text{at } r=0 \text{ and as } r \text{ approaches } \infty$$

The equation set requires one additional boundary condition. The continuity equation and the axial momentum equation may be combined into an integral constraint: this constraint requires the momentum swept past any cross-section to be constant for all axial positions. The final boundary condition is evaluated at the jet exit to yield*

$$M_o = 2\pi \int_0^\infty U^2 r \, dr \qquad (2.2.7)$$

The constant term M_o is called the kinematic momentum. Since momentum is conserved, this boundary condition provides an important quantitative check for measured velocity values. The importance of this boundary condition has been ignored by most experimenters - its impact will be discussed in detail in the following section and the next chapter. Recalling that we have taken boundary layer effects and turbulent intensities to be negligible, we use a top hat profile for the mean velocity profile. The subscript 'o' denotes a boundary condition at the jet exit.

$$M_o = (\pi D^2/4) U_o^2 = A_o U_o^2 \qquad (2.2.8)$$

The turbulent jet is easily scaled using dimensional

---

* A derivation of the momentum integral is presented in section 2.4. The form shown here is valid only if the contributions of the fluctuating quantities are negligible, as is the case at the exit.

analysis. The only two length scales present are x and r. The only non-zero boundary condition (equation 2.2.7) provides the remaining scale, the kinematic momentum, M_o. Thus, on dimensional grounds alone, we may expect the following functional form for the velocity distribution.

$$U = \frac{M_o^{1/2}}{x} f(\eta) \qquad \text{for} \quad \eta = r/x$$

$$\overline{uv} = \frac{M_o}{x^2} s(\eta) \tag{2.2.9}$$

The rate of decay of the centerline velocity, U_m, is determined by setting η equal to zero. This relationship is more commonly found expressed in terms of the exit velocity. The centerline decay rate has the following functional forms

$$U_m = \frac{B_M M_o^{1/2}}{x} \qquad \text{for} \quad B_M = f(\eta=0)$$

or

$$\frac{U_o}{U_m} = \frac{1}{B_U}\left[\frac{x'}{D} - \frac{x_o}{D}\right] = \frac{1}{B_U}\,(x/D) \tag{2.2.10}$$

where $B_U = (\pi/4)^{1/2} B_M$ for top hat exit profile

The equations of motion are further simplified when mapping the system of equations into similarity variables. The continuity equation can be used to determine the radial velocity as a function of the axial velocity.

$$V = \frac{M_o^{1/2}}{x} k(\eta) = \frac{M_o^{1/2}}{x}\left(\eta f - \frac{1}{\eta}\int_o^\eta \eta f \, d\eta\right) \tag{2.2.11}$$

The result is an ordinary differential equation

relating the mean axial velocity to the Reynold's stress:

$$f^2 + \frac{f'}{\eta} \int_0^\eta f\eta \, d\eta = (\eta s)' \qquad (2.2.12)$$

It can be easily shown that the boundary conditions reduce to

$$\begin{aligned} f(\eta) &= 0 \qquad \text{as } \eta \text{ approaches } \infty \\ f'(\eta) &= 0 \qquad \text{at } \eta = 0 \\ 2\pi \int_0^\infty f^2(\eta)\, \eta \, d\eta &= 1 \end{aligned} \qquad (2.2.13)$$

Following the first theoretical treatment by Tollmien, investigators have applied a wide variety of closure schemes to the jet. The success of zero-equation models may be attributed to the fact that the jet is not a multiple scale flow problem. The relation between the local stress and the local rate of strain can be shown to be a dimensional necessity.* For such cases, a simple proportionality relationship between turbulent 'stress' and mean velocity gradient can be assumed. The constant of proportionality is the eddy viscosity, μ_e and is defined as follows

$$-\rho \overline{uv} = \mu_e \frac{\partial U}{\partial r} \qquad (2.2.14)$$

The substitution of an eddy viscosity model into the

---

* Hinze's text provides an excellent summary of these models. That of Tennekes and Lumley gives physical interpretation of when we may expect them to be applicable. Schlichting provides a short, concise account of the derivation of the polynomial profile.

similarity equation provides a guide in choosing the functional form fitted to the measured velocity profiles. An exact solution produces a polynomial profile.*

$$f(\eta) = \frac{B_M}{(1 + A_p\eta^2)^2}$$

$$k(n) = \frac{B_M}{2} \frac{\eta - A_p\eta^3}{(1 + A_p\eta^2)^2} \qquad (2.2.15)$$

On a purely empirical basis, a Gaussian profile may be selected as a solution for the mean axial velocity. The mean velocity profile might thus be approximated using

$$f(\eta) = B_M\, e^{-A_G\eta^2}$$

$$k(n) = \frac{B_m}{\eta} \left(\eta\, e^{-A_G\eta^2} + \frac{1}{2A_G} \left(e^{-A_G\eta^2} - 1\right)\right) \qquad (2.2.16)$$

Section 2.3: Volume Entrainment and Momentum Flux

A full understanding of the physics of the turbulent jet is possible only if all the implications of the volume and momentum flux are understood. The equations of motion require the momentum flux at any cross-section to be constant. For a similarity solution to exist, it is easily shown that the volume flux must grow linearly with x, that is

$$m = M_o^{1/2} x \int_0^\infty f(\eta)\, 2\pi\eta\, d\eta$$

$$m = K\, M_o^{1/2} x \qquad (2.3.1)$$

where

$$K = \int_0^\infty f(\eta)\, 2\pi\eta\, d\eta$$

As a result of the above expression for the volume flux, it is clear that the volume flux at the origin must be zero! The mathematical model for the source of the turbulent jet is therefore a point source of momentum.

In reality, there is always a finite volume flux at the source. It is reasonable to expect that a turbulent jet assumes the properties of its theoretical idealization when the volume of entrained air is much greater than the initial volume flux at the origin. For the circular jet with a top hat velocity exit profile, the volume flux at the origin is

$$m_o = U_o \pi D^2/4 = M_o/U_o \qquad (2.3.2)$$

From equation 2.3.1, the ratio of the volume flux at x to the source volume flux can be determined.

$$\frac{m}{m_o} = \frac{K x U_o}{M_o^{1/2}} = 2\frac{K}{\pi}\frac{x}{D} \qquad (2.3.3)$$

Seif's values of $B_m = 6.5$ and $\eta_{1/2}=0.095$ are used with a Gaussian fit to evaluate K. The above relation becomes

$$\frac{m}{m_o} = 0.17\,\frac{x}{D} \qquad (2.3.4)$$

Viewed in this manner, it is not suprising that Wygnanski and Fiedler reported that the turbulent

intensities did not attain similarity until an x/D value of seventy. At this axial location, the entrained fluid is only twelve times greater than the volume flux at the source.

What non-dimensional parameter should be used to scale the downstream coordinate, x, in those cases where the jet does not have either a uniform velocity profile or a noncircular exit area? The answer again lies with the exit volume and momentum flux. Using these parameters, an effective length scale D_* can be defined as

$$D_* = m_o / M_o^{1/2} \tag{2.3.5}$$

$$\frac{x}{D_*} = \frac{x M_o^{1/2}}{m_o}$$

The correct downstream scaling can be viewed as the ratio of the entrained volume flux to the original volume flux at the jet source. For the classical case of the circular jet with a uniform velocity profile, the scaling value is proportional to the exit diameter of the jet.

$$D_* = (\pi/4)^{1/2} D = 1.57 D \tag{2.3.6}$$

Unfortunately, existing measurements have not been scaled using this argument. To avoid confusion with other authors, this work will continue to represent the nondimensional axial coordinate as x/D.

Accurate determination of both volume entrainment and momentum flux are critical for the study of the axisymmetric

jet. The volume flux is important for two reasons. First, it is very sensitive to the profile width and shape. Because of this, it is sensitive to how the Reynolds stress is modeled. The second reason involves practical purposes where it is a key parameter in determining the rate at which the jet is mixing with the ambient environment. The importance of the momentum flux has been discussed in the preceding chapter - it is a crucial boundary condition by which the accuracy of experimental data may be judged.

Recall the two functional forms fitted to the mean axial velocity profile (equations 2.2.14 and 2.2.15). In both the polynomial and Gaussian forms, the height of the profile is set by the constant B_m while the width of the profile is determined by A. The jet half-width ($\eta_{1/2}$) is defined as that point where the mean axial velocity is half the centerline value, i.e.

$$f(\eta=\eta_{1/2}) = 1/2 \qquad (2.3.7)$$

Because this quantity is easy to measure and provides a convenient reference, it can be used to quickly establish the value of the constants A_P and A_G, given the measured half width. Thus

$$A_G = \left(\frac{0.833}{\eta_{1/2}}\right)^2 \qquad (2.3.8A)$$

while

$$A_P = \left(\frac{0.643}{\eta_{1/2}}\right)^2 \qquad (2.3.8B)$$

For convenience in switching from one functional form

to another, the above two equations are are used to find A_p as a function of A_G. Eliminating the half-width gives

$$A_p = (0.598)\, A_G \quad \text{or} \quad A_G = (1.67)\, A_p \qquad (2.3.9)$$

A comparison of the fit of these functions to the mean profile is depicted in Figure 2.3.1. The experimental data points are a product of this investigation and have an axial positon corresponding to an x/D equal to 67 (more will be said about these results in chapter three). The polynomial and exponential fits are evaluated using Seif's predicted value for the half-width of 0.095. Of the two forms, the polynomial fits best near the center, but does not roll off quickly enough with increasing radius. The Gaussian curve is slightly high near the center, but gives much better agreement at the edges of the velocity profile.

The selection of a function to fit the profile becomes crucial if that function is used to evaluate the momentum flux or entrainment. There are two basic difficulties with such a procedure. First, both quantities are integrated, so any nonrandom error is summed. Second and more importantly, when evaluating the transport of any quantity across a profile, errors at the outer edge carry an increased significance because of the $2\pi r$ associated with the integral.

Consider first the momentum flux (equation 2.2.13). Assume the constant B_m is determined from the centerline

FIGURE 2.3.1

COMPARISON OF POLYNOMIAL AND GAUSSIAN FIT
MEAN AXIAL VELOCITY PROFILE

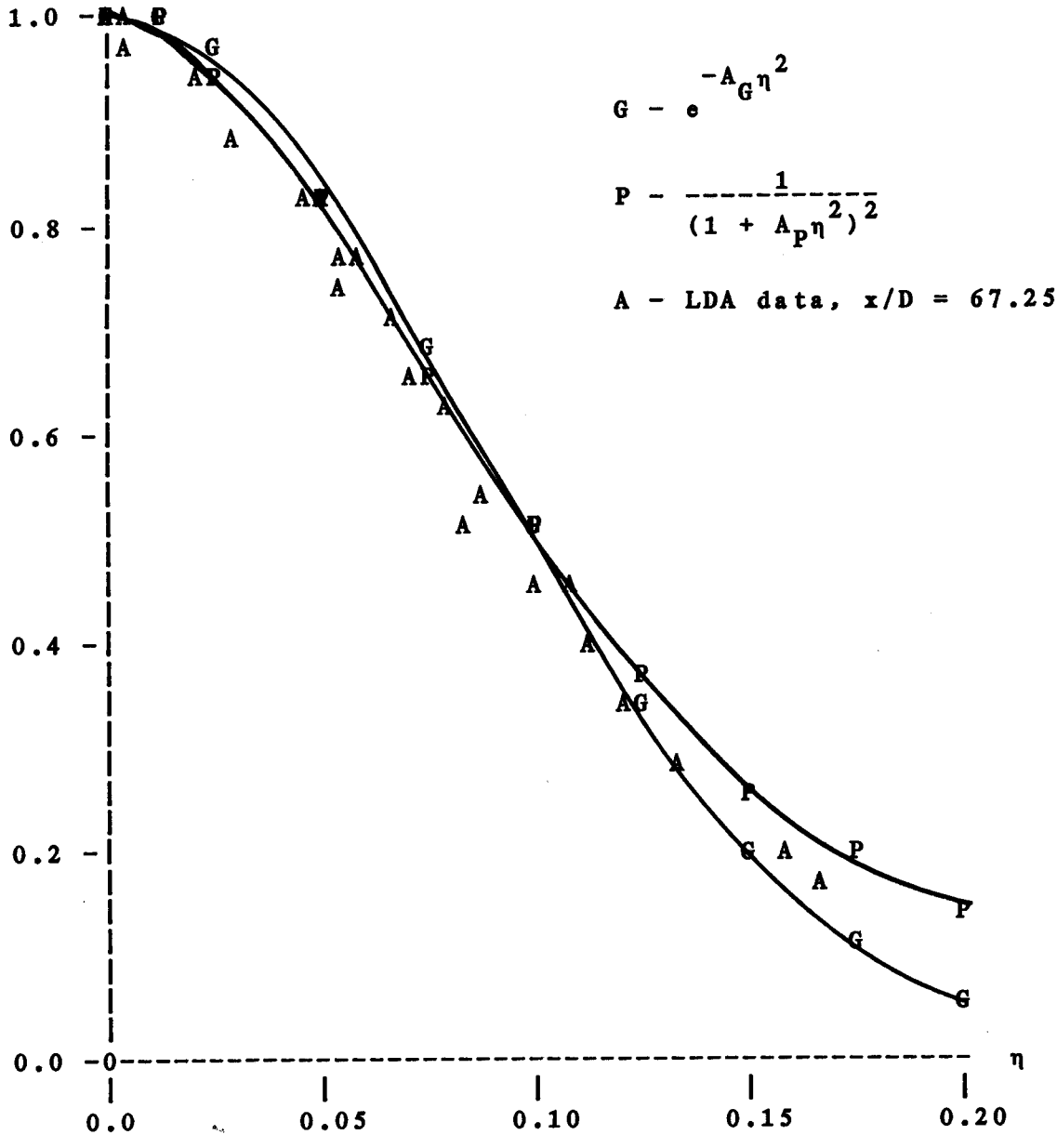

A_P and A_G selected so that $\eta_{1/2} = 0.095$

velocity decay rate. As before, the half-width is used to determine A_p and A_G. The integral may be expressed in terms of B_m and A or B_m and the jet half-width. The polynomial and Gaussian functions are substituted into this equation to obtain

$$2\pi \int_0^\infty f^2(\eta)\, \eta\, d\eta = 1 \qquad \text{momentum conservation}$$

$$= \frac{1.05\, B_m^2}{A_p} = 2.53\, (B_m \eta_{1/2})^2 \qquad \text{poly.}$$

$$= \frac{1.57\, B_m^2}{A_G} = 2.26\, (B_m \eta_{1/2})^2 \qquad \text{Gauss.}$$

(2.3.10)

The polynomial prediction for the momentum flux exceedes the Gaussian value by 12%. The predominate source of this disparity lies in the differing behavior of the functions at the outer edge. This is clearly illustrated in Figure 2.3.2 where the integrand of equation (2.3.10) is plotted. The values of the integrand due to the Gaussian and polynomial fits begin to diverge at an η of 0.15. For both functions, the integrand is effectively zero for any values of η greater than 0.25. It is also interesting to note that even if the profile could be fitted exactly by either of these functions, any error in the determination of the constants B_m or $\eta_{1/2}$ would double when evaluating the momentum flux. For example, if these two constants were determined to an accuracy of 2%, the uncertainty in the momentum integral would be 4%.

FIGURE 2.3.2

COMPARISON OF POLYNOMIAL AND GAUSSIAN FIT
MOMENTUM FLUX INTEGRAL

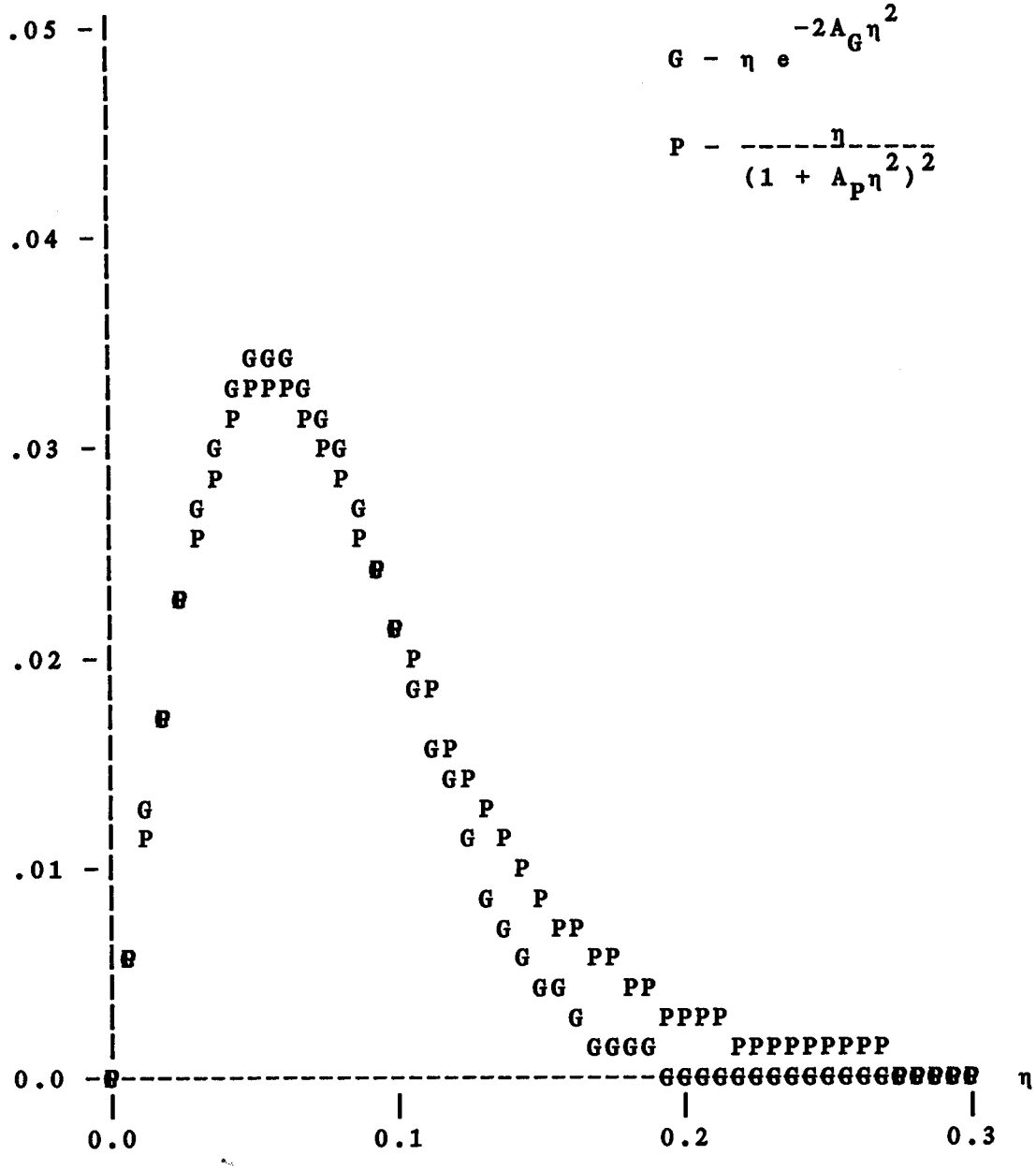

A_P and A_G selected so that $\eta_{1/2} = 0.095$

The volume flux and entrainment prove to be more sensitive to the profile shape than the momentum flux. Again, the polynomial and Gaussian functions are fitted into the integral

$$m = \left(\frac{\pi B_m}{A_P}\right) M_o^{1/2} x = (7.60\, B_m \eta_{1/2}^2)\, M_o^{1/2} x \qquad \text{polynomial}$$

$$= \left(\frac{\pi B_m}{A_G}\right) M_o^{1/2} x = (4.53\, B_m \eta_{1/2}^2)\, M_o^{1/2} x \qquad \text{Gaussian} \qquad (2.3.11)$$

The volume flux computed using a polynomial profile is 68% greater than that due to a Gaussian form! As in the case for the momentum flux, this behavior is a result of the rate of decay of the profiles at large η. Figure 2.3.3 clearly shows a significant divergence in the values of the integrand for η greater than 0.10. More importantly, note that a substantial portion of the integral using a polynomial fit is obtained from values of η beyond 0.25. Examination of the intermittency factor for the turbulent jet (see Figure 2.3.4) and the mean velocity profile (Figure 2.3.1) indicates that the region of activity for the jet is within a value of η less than 0.25 and any contribution past this radius to the net momentum or volume flux is necessarily small. Clearly, the polynomial curve cannot be used to estimate the volume flux.

It is possible to make the following conclusions. First, either function satisfactorily traces the mean profile. Up to an η of 0.15, there is little noticeable

FIGURE 2.3.3

COMPARISON OF POLYNOMIAL AND GAUSSIAN FIT
VOLUME FLUX INTEGRAL

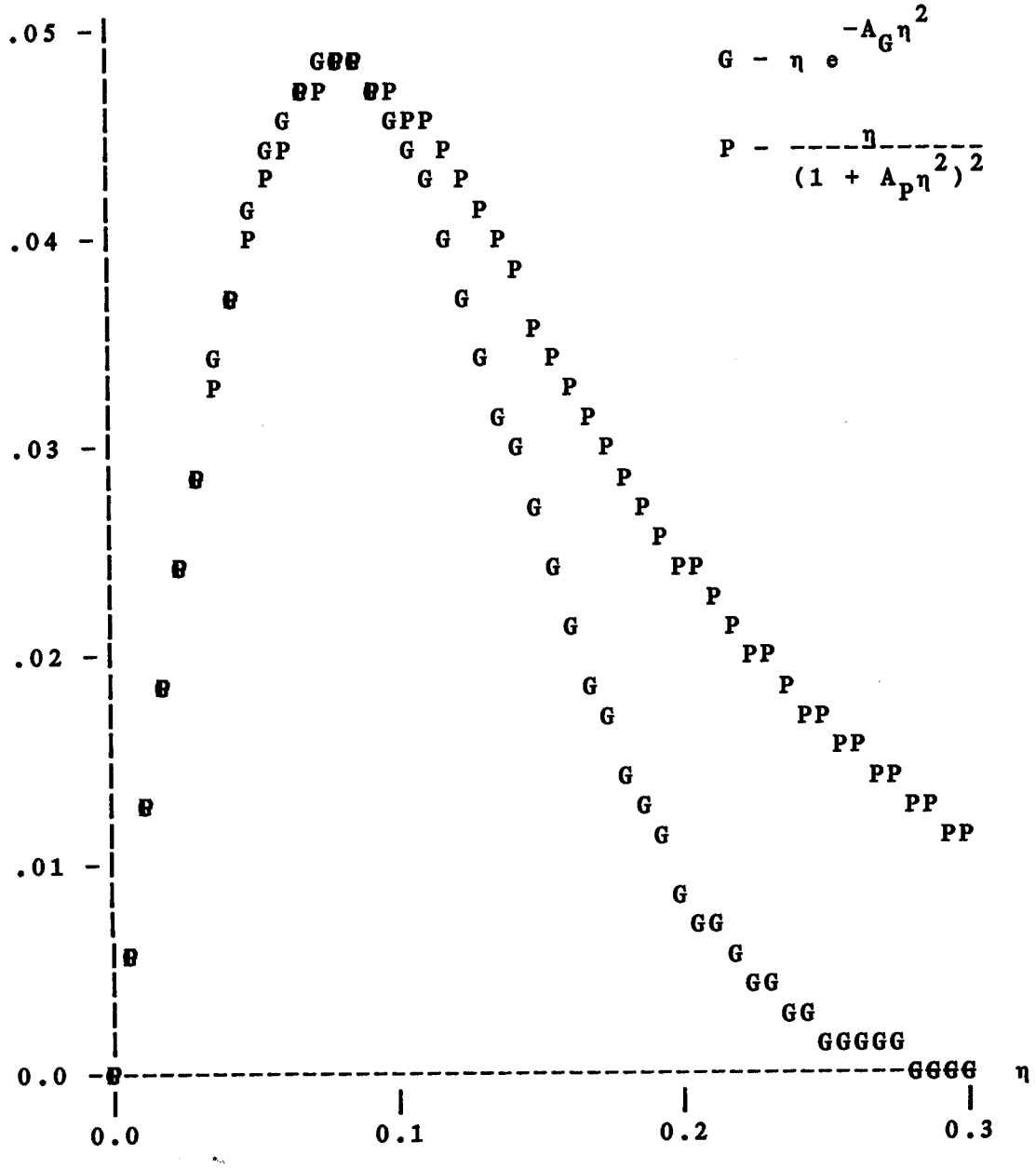

A_P and A_G selected so that $\eta_{1/2} = 0.095$

FIGURE 2.3.4

LOCAL TURBULENT INTENSITIES AND INTERMITTENCY FACTOR
WYGNANSKI AND FIEDLER - 1969

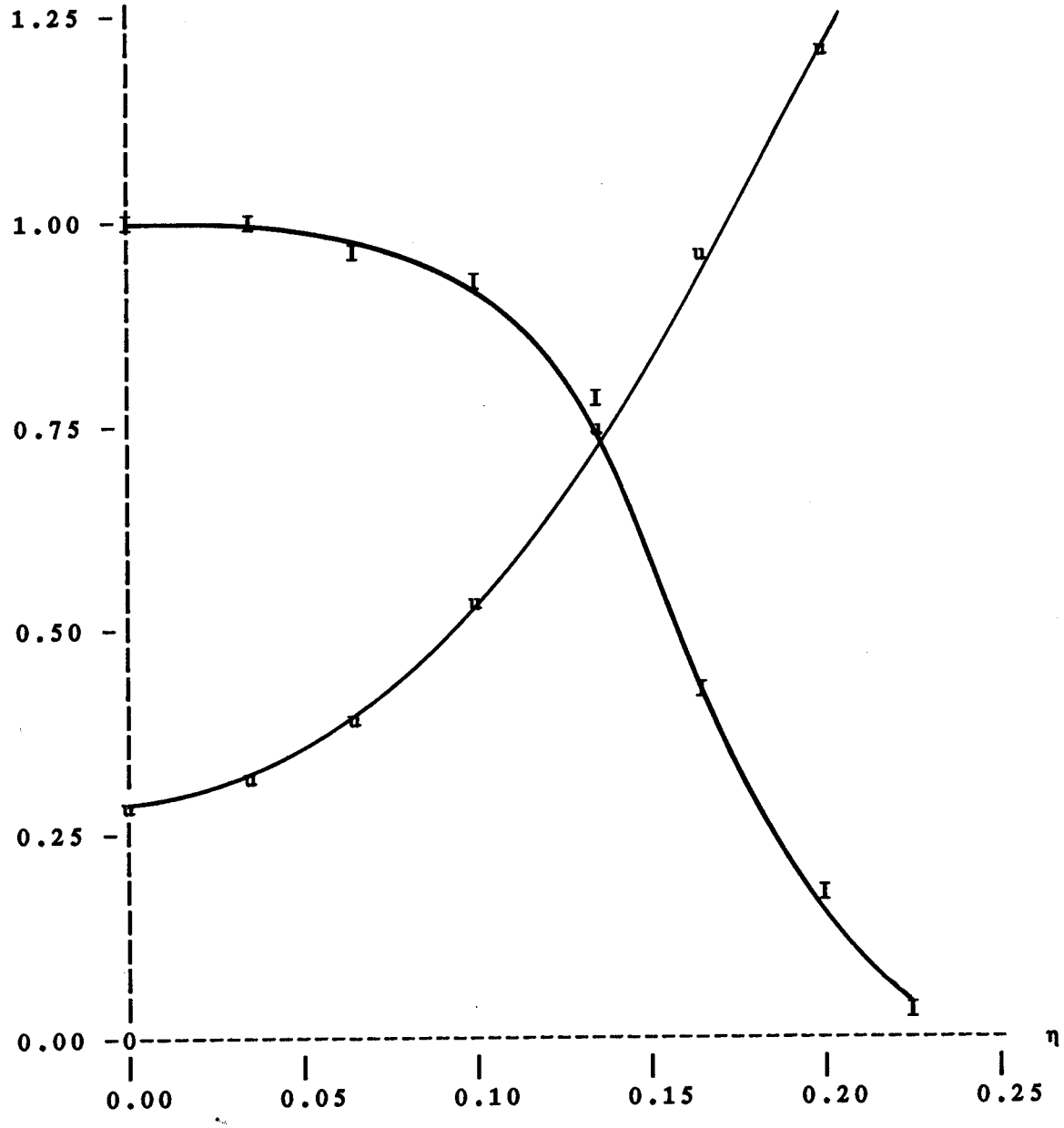

difference in the two forms. Past this point, the Gaussian underestimates the profile while the polynomial overshoots the mean velocity. Secondly, both the polynomial and Gaussian functions prove of equal utility in evaluating the momentum constraint since they may be viewed as upper and lower limits, respectively. Finally, only the Gaussian function is useful for estimating the volume flux, even then it probably should be viewed as a lower limit. The polynomial fit badly overestimates the volume flux and under no circumstances should be considered as a reliable estimate for the entrainment.

To make a reliable estimation of the entrainment, the profile shape at the outer edges must be accurately determined. Unfortunately, this is extremely difficult to do when relying on CTA techniques. Figure 2.3.4 shows the relative turbulent intensities according to the data of Wygnanski and Fiedler. Levels above 50% are reached at the half-width of the jet. Because of cross-flow or reverse-flow errors, rectification, prong effects, etc., the profile measurements taken by CTA systems are highly suspect near the outer edges.* LDA measurements are not subject to such error and may be relied upon to provide greater accuracy at the outer edges of the flow. However, both

---

* For a more detailed discussion of the problems due to CTA measurements, see Beuther (1980).

methods are handicapped by the long averaging times needed to accurately compute averages at the outer edges of the flow field (see section 8.1).

At this point it is convenient to pause and review the definition of the entrainment coefficient, α. Integral methods used by a number of authors rely on an accurate determination of this value. Their approach begins by multiplying the equations of motion by $2\pi r$ and integrating from zero to infinity. The result for the momentum equation is the familiar requirement of momentum conservation.**

$$\frac{d}{dx} \int_0^\infty U^2 \, 2\pi r \, dr = 0 \qquad (2.3.12)$$

The final form for the continuity equation after the integration has been carried out has a simple physical interpretation. It equates the volume of fluid entrained per unit length of the jet as a result of the inward directed radial velocity, V, to the rate of change of the volume flux in the axial direction, thus

$$E = \lim_{r \to \infty} (-2\pi r V) = \frac{d}{dx} 2\pi \int_0^\infty U \, r \, dr \qquad (2.3.13)$$

Since the volume flux scales linearly with x (see equation 2.3.11) the entrainment is constant. A local length, b, and velocity scale, U_*, can be defined using an equivalent top hat profile and by requiring this profile to

---

** See footnote in section 2.2

have the same volume and kinematic momentum flux as the jet. Thus

$$b^2 U_* = 2 \int_0^\infty U \, r \, dr$$

$$b^2 U_*^2 = 2 \int_0^\infty U^2 \, r \, dr \qquad (2.3.14)$$

The equation set is closed by assuming the entrainment is determined exclusively by these local parmeters. The constant relating the entrainment to these flow scales is the entrainment coefficient, α, defined from

$$E = 2\alpha b U_* \qquad (2.3.15)$$

Using the polynomial and Gaussian functions, values for b, U_*, α and E can be computed as a function of M_o, B_M and A. The results are listed in Table 2.3.1. Although the actual magnitudes of b and U_* differ according to the selected function, this feature is not of critical importance since the exact shape of the top hat profile has little physical meaning. It should be noted that the length scale b is directly proportional to x and the velocity scale U_* is inversely proportional to x. This behavior is in agreement with the linear spreading of the jet and the 1/x dependence of the centerline velocity. It is the value of the entrainment and entrainment coefficient that is of crucial importance here. For a quantitative comparison of the entrainment and entrainment coefficient, the relationship between A_P and A_G (see equation 2.3.9) must

TABLE 2.3.1

ENTRAINMENT PARAMETERS FOR GAUSSIAN AND POLYNOMIAL FUNCTIONS

	POLYNOMIAL	GAUSSIAN
$\frac{b}{x}$	$(3/A_P)^{1/2}$	$(2/A_G)^{1/2}$
$\frac{U_* x}{M_o^{1/2}}$	$B_M/3$	$B_M/2$
$\frac{E}{M_o^{1/2}}$	$\pi B_M/A_P$	$\pi B_M/A_G$
α	$\frac{\pi}{2}$ $(3/A_P)1/2$	π $(2/A_G)^{1/2}$

When both functional forms intersect at the half width, the constant coefficients A_P and A_G may be related using

$$A_P = (0.598)\ A_G$$

be employed. The values of the entrainment and entrainment coefficient are just as sensitive to the functions fit at the outer edge of the flow as is the volume flux. The same conclusions concerning the use of these functions in evaluating the volume flux applies to their use in evaluating the entrainment. It is therefore suggested that the Gaussian profile be used in computing the lower limit of the entrainment. Further discussions concerning experimental values for this estimate can be found in section 4.1.

Section 2.4: Derivation of Momentum Constraint

The derivation for the equations of motion for the turbulent jet has already been outlined in section 2.2. If the reader desires more detail, he may reference Tennekes and Lumley (1972). The momentum constraint as presented in most works begins with the simplified equation set as represented by equations (2.2.1) and (2.2.5). The simplified form of the x-momentum equation is then multiplied by $2\pi r\, dr$ and integrated across the profile. In general, it can not be assumed that if the contribution of an individual term to the differential equations of motion is negligible over most of the flow, then the contribution of that term integrated across the flow is also negligible. Because of this, the derivation for the momentum conservation constraint is reexamined in this section. It

will be shown that the neglected terms account for up to eight percent of the source momentum.

The steady state ($\partial/\partial t = 0$) Navier-Stokes equations in cylindrical coordinates for incompressible and isothermal turbulent flow are well known. For the axisymmetric jet with no swirl, the mean azimuthal component (W) and the turbulent shear stress uw and wv are all zero. For these conditions, the continuity and momentum equations reduce to

$$\frac{1}{r}\frac{\partial}{\partial r}(rV) + \frac{\partial U}{\partial x} = 0$$

$$U\frac{\partial U}{\partial x} + V\frac{\partial U}{\partial r} = \frac{-1}{\rho}\frac{\partial P}{\partial x} + \frac{\mu}{\rho}D^2[U] - \frac{\partial \overline{u^2}}{\partial x} - \frac{1}{r}\frac{\partial}{\partial r}(r\overline{uv})$$

$$U\frac{\partial V}{\partial x} + V\frac{\partial V}{\partial r} = \frac{-1}{\rho}\frac{\partial P}{\partial r} + \frac{\mu}{\rho}\left(D^2[V] - \frac{V}{r^2}\right) - \frac{1}{r}\frac{\partial}{\partial r}(r\overline{v^2}) - \frac{\partial}{\partial x}(\overline{uv}) + \frac{\overline{w^2}}{r}$$

where

$$D^2[\ ] = \frac{\partial^2}{\partial r^2} + \frac{1}{r}\frac{\partial}{\partial r} + \frac{\partial^2}{\partial x^2} \qquad (2.4.1)$$

The first step is to solve for the pressure field by multiplying the V momentum equation by dr and then integrating from some reference r to infinity. The functions R_1, R_2 and R_3 are defined as

$$R_1 = \int_r^\infty \frac{\mu}{\rho}\left(D^2[V] - \frac{V}{r^2}\right) dr$$

$$R_2 = \int_r^\infty \left(U\frac{\partial V}{\partial x} + V\frac{\partial V}{\partial r}\right) dr \qquad (2.4.2)$$

$$R_3 = \int_r^\infty \frac{\partial}{\partial x}(\overline{uv})\, dr$$

The pressure field is then

$$\frac{P_\infty - P}{\rho} = R_1 - R_2 - R_3 + \int_r^\infty \frac{\overline{w^2}}{r}\, dr - \int_r^\infty \frac{1}{r}\frac{\partial}{\partial r}\, r\overline{v^2} \qquad (2.4.3)$$

The last term on the right hand side is integrated by parts to give

$$\frac{P_\infty - P}{\rho} = R_1 - R_2 - R_3 + \overline{v^2} + \int_r^\infty \frac{\overline{w^2} - \overline{v^2}}{r}\, dr \qquad (2.4.4)$$

The pressure gradient is determined by differentiating with respect to x. Since P_∞ is constant

$$-\frac{1}{\rho}\frac{\partial P}{\partial x} = \frac{\partial}{\partial x}(R_1 - R_2 - R_3) + \frac{\partial \overline{v^2}}{\partial x} - \frac{\partial}{\partial x}\int_r^\infty \frac{\overline{v^2} - \overline{w^2}}{r}\, dr \qquad (2.4.5)$$

This expression for the pressure gradient is substituted into the U momentum equation. The U momentum equation is multiplied by r dr and integrated from zero to infinity. With the aid of the continuity equation, the result can be written as follows

$$\underbrace{\frac{\partial}{\partial x}\int_o^\infty (U^2 + \overline{u^2} - \overline{v^2})r\, dr}_{i} + \underbrace{\int_o^\infty \frac{\partial}{\partial r}(UV)\, dr}_{ii} + \underbrace{\int_o^\infty \frac{\partial}{\partial r}(r\overline{uv})\, dr}_{iii}$$

$$+ \underbrace{\int_o^\infty \frac{\partial}{\partial x}\int_r^\infty \frac{\overline{v^2} - \overline{w^2}}{r'}\, dr'\, r\, dr}_{iv} - \underbrace{\int_o^\infty \frac{\partial}{\partial x}(R_1 - R_2 - R_3 + R_4)\, r\, dr}_{v} = 0$$

where $R_4 = \mu/\rho\, D^2[U]$ (2.4.6)

Term ii integrates to zero since the mean radial velocity is zero at the limits of integration. Term iii also integrates to zero since the Reynolds stress is also zero at both the centerline and at infinity. Using integration by parts, term iv can be represented as

$$(iv) = \frac{r^2}{2} \int_r^\infty \frac{\overline{v^2} - \overline{w^2}}{r} \Big|_o^\infty - \int_o^\infty \frac{r^2}{2} \frac{(\overline{w^2} - \overline{v^2})}{r} dr$$

$$= \int_o^\infty \frac{\overline{v^2} - \overline{w^2}}{2} r \, dr \qquad (2.4.7)$$

The momentum integral becomes

$$\frac{\partial}{\partial x} \int_o^\infty (U^2 + \overline{u^2} - (\frac{\overline{v^2} + \overline{w^2}}{2})) r \, dr$$

$$= \frac{\partial}{\partial x} \int_o^\infty (R_1 - R_2 - R_3 + R_4) r \, dr \qquad (2.4.8)$$

Up to this point, all the original terms in the equations of motion have been retained. The convection and viscous terms arising from integration of the V-momentum equation are contained on the right hand side. The viscous term from the U-momentum equation is also on this side. It will be shown that these terms can be ignored and that the momentum constraint is governed only by those terms on the left hand side. The influence of the pressure field on the momentum constraint is represented by the radial and azimuthal normal Reynolds stresses since these are the only terms remaining from the integration of the V-momentum

equation.

An order of magnitude analysis is now carried out. Choose δ as a characteristic scale for the width of the jet and L as the scale for streamwise variations. The jet half-width can by used as the ratio of these two length scales so that $\delta/L \sim 0.1$. The local centerline velocity U_m is used to scale the mean axial velocity. From continuity, the radial velocity scale is $U_m\delta/L$. The value of the turbulent intensity at the centerline can be used to determine the magnitude of the local turbulence velocity scale, u, that is $u/U_m = 0.25$. The source momentum flux is approximated as $M_o \sim (U_m\delta)^2$.

First, consider the two viscous stress terms. Both of these terms involve the Laplacian operator, $D^2[\ ]$ as given by the last equation in equations (2.4.1). The radial derivative term is larger in magnitude by order $(L/\delta)^2$ so only it will be considered. The ratio of the integration of R_1 to the source momentum flux is

$$\frac{1}{M_o}\int_o^\infty R_1\, r\, dr = \frac{1}{M_o L}\frac{\mu}{\rho}\frac{U_m\delta}{L}\delta^2 = \frac{\mu/\rho}{U_m L} = 10^4 \rightarrow 10^5 \qquad (2.4.9)$$

A similar procedure is carried out for the second viscous term, R_4. Direct integration of the radial term shows this portion of the integral is zero.

$$R_4 : \quad \frac{1}{M_o L}\frac{\mu}{\rho}\frac{\delta^2}{L^2}\delta^2 = \frac{\mu/\rho}{U_m L} = 10^4 \rightarrow 10^5 \qquad (2.4.10)$$

Since the similarity forms require the centerline

velocity to be inversely proportional to the axial length scale, the Reynolds number is constant. Typical values of the Reynolds number for available sets of experimental data run from 10^4 to 10^5. It can be safely concluded that the viscous terms can be ignored in the integrand of the right hand side.

The off-diagonal Reynolds stress term, R_3, is scaled as

$$R_3 : \frac{1}{M_o} \frac{u^2}{L} \frac{\delta^3}{} = \left(\frac{u}{U_m}\right)^2 \frac{\delta}{L} = 0.006 \qquad (2.4.11)$$

The estimate for the contribution due to the 'force' exerted by the streamwise gradient of the Reynolds stress is small enough so that it also can be safely ignored.

The final term to be examined is the convection term from the V-momentum equation as represented by R_2. An order of magnitude analysis for this term produces

$$R_2 : \frac{1}{M_o L} U_m \left(\frac{U_m \delta}{L}\right) \delta^3 = 0.01 \qquad (2.4.12)$$

The radial transport terms could only hold at most a few percent of the source momentum. It can therefore be concluded that the contribution to the momentum constraint by the terms on the right hand side of equation (2.4.8) is negligible. Failure to consider these terms should at most add only a few percent error to the estimation for the momentum integral.

The left hand side of equation (2.4.8) can be

multiplied by 2π and then integrated with respect to x to yield the final form for the momentum integral. The constant of integration is the kinematic momentum added at the source.

$$M_o = \int_o^\infty (U^2 + \overline{u^2} - \frac{(\overline{v^2} + \overline{w^2})}{2}) \, 2\pi r \, dr \qquad (2.4.13)$$

Standard jet design attempts to acheive a top hat profile at the exit. Published literature cites no correction for boundary layer effects at the nozzle lip or mentions any overshoot in the velocity profile. Experience in the jet facility used in this experimental work (see chapter 3) indicates the worst error condition in using a top hat profile to measure the exit momentum flux would be an underestimation of only two percent. As stated in section 2.1, measurements have indicated that the momentum of the top hat profile is conserved in the developing region of the jet again with an error of around 2-3%. Considering the difficulties in determining the integral at the outer edge of the jet (see section 2.3) there seems to be little point in seeking greater accuracy for this value.

What is the role of the fluctuating terms on the left hand side? First, consider only the ratio between the mean axial velocity, U, and the normal turbulent stress, u^2. Using 25% as the estimate for the centerline turbulence intensity, the contribution of u^2 is only six percent of the mean velocity. But figure 2.3.4 reveals that this is a

low estimate for the relative turbulence intensity increases away from the axis. This is because the mean velocity profile rolls-off faster with r than does u^2. The effect of the turbulence intensity on the integral using the above scaling argument would be underestimated. Note the negative contribution of v^2 and w^2 tends to reduce the influence of u^2 upon the integral. Based upon the available data and computer models, George et al. (1982) have estimated the combined effect of all the turbulent stress terms to be between seven to eight percent.

The behavior of this integral has been carefully examined in Seif's dissertation. Figure 2.4.1 plots the contributions of the individual terms of the momentum constraint for the data of Wygnanski and Fiedler and of Rodi. The net contribution of each term is listed in Table 2.4.1. This table also lists the values according to Abbiss et al. (1976) and the numerical solution of Seif (1982). The failure of the data to conserve momentum is clearly revealed. Wygnanski and Fiedler fail to account for 40% of the source momentum. Rodi's CTA data and the LDA data of Abbiss et. al. lack only 16% of the momentum. With the exception of the pulsed wire measurements, the experiments have all recorded a jet half width of $\eta_{1/2}=0.086$. Suprisingly, the measurements fail to agree upon the centerline decay rate. This is unexpected, since the turbulent intensity is lowest along the jet axis so that it

Reference	B_U	$M_o^{-1}\int_o^\infty (\frac{U}{U_m})^2(\frac{r}{x})d(\frac{r}{x})$	$M_o^{-1}\int_o^\infty (\frac{\overline{u^2}}{U_m^2})(\frac{r}{x})d(\frac{r}{x})$	$M_o^{-1}\int_o^\infty (\frac{\overline{v^2}}{U_m^2})(\frac{r}{x})d(\frac{r}{x})$	$M_o^{-1}\int_o^\infty (\frac{\overline{w^2}}{U_m^2})(\frac{r}{x})d(\frac{r}{x})$	$\frac{M(\infty)}{M_o}$
Wygnanski & Fiedler	5.0	.540	.122	.060	.064	.60
Rodi	6.0	.770	.17	.091	.106	.84

TABLE 2.3.1

MOMENTUM BALANCE

is this region where one should expect the data to be reliable. Yet it is here that the measurements have their strongest disagreement. This matter will be discussed in greater detail in chapter 4. At this point, it is sufficient to state that the data does provide the evidence to prove that the normal turbulent stress terms account for anywhere from six to eight percent of the source momentum. As a result, when evaluating the validity of the jet measurements based on the momentum constraint, the momentum constraint as first presented in equation (2.2.7) should not be used. The correct form of the momentum constraint is that given by equation (2.4.13).

Section 2.5: Momentum Loss in a Confined Jet

The previous section has demonstrated that the current measurements in the far-field region of the axisymmetric jet fail to conserve momentum. In this section it will be hypothesized that the primary problem with existing data is due to the physical facility. Some critical features of the return flow must first be identified. To begin with, a confined or enclosed jet is defined as jet in a finite environment. For convenience in the analysis, it is assumed that the cross-sectional area of the room, A_R, is a constant and independent of x. The room cross-section is much larger than the area swept out by the jet. The return flow velocity, U_∞ is therefore much smaller in magnitude

then the velocity associated with the jet. Conservation of mass requires the net volume flow across a cross section to be zero. Since the volume flux increases downstream, the return flow velocity increases with x. An unfavorable pressure gradient must exist to drive this back flow. With a simple flow model it is possible to demonstrate this effect.

It will be shown that although the back flow and adverse pressure gradient are much smaller in magnitude than any of the physical quantities found in the turbulent jet, their effect is not neglible. Because of the large area involved in the return flow, there is a reduction of axial momentum swept downstream at any cross section. The analysis begins with the momentum constraint as derived in the preceding section. Because of the reverse flow in the confined jet, the ambient pressure is no longer uniform. The ambient pressure gradient is no longer zero and must be included in the momentum balance. The difference in the momentum constraint between the jet and the confined jet lies in the addition of the external pressure gradient caused by the reverse flow. It is assumed the pressure gradient is small enough so that its magnitude is negligible when substituted into the equations of motion, thus ensuring that a similarity solution still exists. However, it is large enough to be of significant importance when integrated in the momentum constraint. The balances for the ideal and

confined jet are respectively,

$$\frac{\partial}{\partial x} \int_0^\infty (U^2 + \overline{u^2} - (\frac{\overline{v^2} + \overline{w^2}}{2})) \, 2\pi r \, dr = 0 \tag{2.5.1}$$

and

$$\frac{\partial}{\partial x} \int_0^R (U^2 + \overline{u^2} - (\frac{\overline{v^2} + \overline{w^2}}{2}) + \frac{1}{\rho} \frac{\partial}{\partial x}(P_\infty)) \, 2\pi r \, dr = 0$$

Note the confined jet is not integrated out to r equals infinity, but rather to some finite radius, R. To determine the integration constants, evaluate the boundary condition at the jet exit. For the ideal jet, the velocity field is zero everywhere except within the top hat profile. Here, only U is nonzero.

$$\int_0^\infty (U^2 + \overline{u^2} - (\frac{\overline{v^2} + \overline{w^2}}{2})) \, 2\pi r \, dr = M_o$$

$$M_o = U_o^2 \, A_o \tag{2.5.2}$$

For the confined jet, the return flow is assumed to be constant across the room's area. The development will assume that the area swept out by the jet flow is small compared to the return flow. As a direct result, the back flow at any cross section may be set equal to the product of the return flow velocity and the room's cross-sectional area. To illustrate the magnitude of these values, consider the experiment of Wygnanski and Fiedler (1969). His experiment is chosen because his data has the greatest contamination due to return flow effects. The wire cage

enclosing their jet had dimension of 2.3 by 2.4 meters for a room area of 5.6 square meters. These boundaries are accepted as the worst case conditions. Consider the axial position of seventy diameters downstream (the exit diameter is 2.54 cm. with an exit velocity of 51 meters/second). If the outer edge of the jet is taken at a value of η equal to 0.20 (or r = 0.36 meters), the jet area is 0.40 square meters. At this point, the jet occupies only seven percent of the room's cross-sectional area. To calculate the volume flux at this point, their predicted values of $B_U = 5.0$ and $\eta_{1/2} = 0.086$ (it shall be later demonstrated that these values are incorrect for the ideal jet) are used in conjunction with a Gaussian profile to predict the volume flux at this point as 0.11 cubic meters/second. The return flow velocity is 26 cm/second at this point versus a centerline velocity of 3.6 meters/second.

For the inviscid flow regime of the return flow, Bernoulli's equation relates the return flow velocity to the pressure gradient.

$$-\frac{1}{\rho}\frac{\partial}{\partial x}(P_\infty) = U_\infty \frac{\partial}{\partial x}(U_\infty) = \frac{\partial}{\partial x}(U_\infty^2/2) \qquad (2.5.3)$$

This relation for the ambient pressure gradient can be substituted into the momentum constraint for the confined jet to yield

$$\frac{\partial}{\partial x}\int_0^R (U^2 + \overline{u^2} - (\frac{\overline{v^2} + \overline{w^2}}{2}) - U_\infty^2/2)\, 2\pi r\, dr = 0 \qquad (2.5.4)$$

It is this form which may be used to determine the constant of integration for the enclosed jet. For the confined jet, the velocity field is equal to U_o within the top hat profile. Because of the back flow, the velocity field is now nonzero outside of the exit. Calculating the constant at the jet exit plane yields

$$\int_o^R (U^2 + \overline{u^2} - (\frac{\overline{v^2} + \overline{w^2}}{2}) - U_\infty^2/2)\, 2\pi r\, dr = M_o + U_\infty^2 A_R/2$$

where as before, $M_o = U_o^2 A_o$ (2.5.5)

Mass continuity can be used to relate the return flow velocity to the jet exit velocity. Typically, the ratio of the jet exit area to the room area is roughly less than or equal to 10^{-4}. This factor may be used to further simply the result.

$$U_o A_o = U_\infty (A_R - A_o)$$
$$= U_\infty A_R \qquad \text{for } A_R >> A_o \qquad (2.5.6)$$

This expression for the return flow velocity is substituted back into the right hand side of equation (2.5.5) with the result,

$$M_o + U_\infty^2 A_R/2 = M_o + (U_o A_o)^2/(2A_R)$$
$$= M_o\,(1 + A_o/2A_R)$$
$$= M_o \qquad \text{for } A_R >> A_o \qquad (2.5.7)$$

When the room area is much larger then the jet exit area, the integration constants for both the ideal and confined are the same.

$$\int_0^\infty \left(U^2 + \overline{u^2} - \left(\frac{\overline{v^2} + \overline{w^2}}{2}\right)\right) 2\pi r \, dr = M_o$$

$$\int_0^R \left(U^2 + \overline{u^2} - \left(\frac{\overline{v^2} + \overline{w^2}}{2}\right) - U_\infty^2/2\right) 2\pi r \, dr = M_o$$

$$M_o = U_o^2 \, A_o \qquad (2.5.8)$$

The constraint for the confined jet differs from the ideal jet in two ways. First, there is an ambient pressure gradient as a result of the return flow (represented by the U_∞ term of the integrand). Second, the integral over the mean velocity must now include the effect of the return flow. For the confined jet, decompose the velocity field shown into two independent components. The radial coordinate R_e is the separation point between the region of the laminar backflow and the zone of the turbulent jet. Under this scheme, the integral of equation (2.5.8) is broken into two parts.

$$\underset{i}{\int_0^{R_e}} \left(U^2 + \overline{u^2} - \left(\frac{\overline{v^2} + \overline{w^2}}{2}\right) - U_\infty^2/2\right) 2\pi r \, dr + \underset{ii}{\int_{R_e}^{R}} \left(U^2 - U_\infty^2/2\right) 2\pi r \, dr = M_o \qquad (2.5.9)$$

The only way in which these regions are coupled is through the mass conservation requirement - any fluid swept downstream by the jet must be returned by the back flow. Rigorously speaking, such a decomposition is incorrect for a

nonlinear system of equations. However, if the return flow is only weakly coupled to the jet it is possible to proceed in this manner in order to qualitatively understand how the confined jet differs from the ideal.

Since R_e is much less than R, terms i thru iii can be combined to give

$$\int (i + ii + iii)\, 2\pi r\, dr = U_\infty^2\, A_R/2 \qquad (2.5.10)$$

Recombining with the turbulent terms of the jet region, the boundary condition is now

$$\int_o^{R_e} (U^2 + \overline{u^2} - (\frac{\overline{v^2}}{2} + \frac{\overline{w^2}}{2})) \, 2\pi r\, dr = M_o - U_\infty^2 A_R/2 \qquad (2.5.11)$$

The first term on the left hand side is the contribution due to the turbulent jet. Since the return flow is x dependent, the momentum integrated across the turbulent jet is also a function of x and is denoted as M(x), the local jet momentum flux.

$$M(x) = \int_o^{R_e} (U^2 + \overline{u^2} - (\frac{\overline{v^2}}{2} + \frac{\overline{w^2}}{2})) \, 2\pi r\, dr$$

$$= M_o - U_\infty^2 A_R/2 \qquad (2.5.12)$$

Examine the behavior of the terms on the right hand side of the above equation. The increasing mass entrainment results in a return flow velocity which is steadily increasing in the downstream direction. Since the source momentum, M_o, is a constant and the return flow velocity

is increasing with x, the right hand side of equation (2.5.12) is decreasing with x. The momentum across the confined jet profile is no longer constant but is instead steadily decreasing in magnitude due to the presence of the return flow.

To procede any further, the concept of self-preservation or local invariance must be used. Consider a simple flow situation like the jet where the time and length scales vary gradually downstream. Let the time scales of the energy transfer processes be fast enough so that past events (i.e. upstream conditions) do not influence the flow dynamics. Since the flow has no difficulty in adjusting to a slowly changing environment, the flow should be dynamicly similar when plotted with the local time and length scales. Using dimensional anyalysis, the volume flux can be related to the kinematic momentum flux. The relationship is the same as that of the ideal jet, only the local momentum flux, M(x), replaces the source momentum flux, M_o (see equation 2.3.1).

$$m(x) = K\,[M(x)]^{1/2}\,x \qquad (2.5.13)$$

Since the volume flux swept downstream by the turbulent jet is equal to the volume flux of the return flow, the local momentum flux may be expressed in terms of the return flow velocity, room area, and downstream position.

$$m(x) = U_\infty A_R \qquad (2.5.14)$$

Equations (2.5.13) and (2.5.14) can be combined to

express the return flow velocity as a function of the local jet momentum flux.

$$U_\infty = \frac{Kx\,[M(x)]^{1/2}}{A_R} \qquad (2.5.15)$$

The momentum constraint given by equation (2.5.12) can now be combined with equation (2.5.15) and the terms rearranged to express the local jet momentum flux as a function of the source kinematic momentum flux, the axial coordinate and the room area.

$$M(x) = \frac{M_o}{1 + (Kx)^2/A_R} \qquad (2.5.16)$$

The final expression for the local jet momentum flux nondimensionalizes the axial position using the jet's exit diameter. In this form, the local momentum flux is a function of x/D, A_o/A_R, and the source momentum flux,

$$M(x) = \frac{M_o}{1 + (2/\pi)\,K^2\,(x/D)^2\,(A_o/A_R)} \qquad (2.5.17)$$

As expected, the local momentum flux decreases with increasing values of x. The behavior of this model is consistent in two key limits: first, in the limit as the room area becomes large ($A_R \rightarrow \infty$) and secondly as the axial coordinate approaches the jet exit ($x/D \rightarrow 0$). In both cases the confined jet approaches ideal jet behavior - *the local momentum flux becomes independent of axial* position and is equal to the source momentum flux. It must be noted that the model must be used with caution. The

initial decoupling of the velocity field assumed limited interaction between the turbulent jet and the return flow. Dimensional scaling for the confined jet uses the same basic relationships as for the ideal jet, the only change being the replacement of the source momentum with the local momentum. This procedure also implicitly relies upon a weak coupling between the two flows. It is this constraint which determines the upper limit on x/D or A_o/A_R to which this model may be applied. Intuitively, we expect this constraint to be violated when the area of the turbulent jet flow begins to occupy a significant area of the enclosure.

Section 2.6: Summary of Basic Considerations

In this chapter, several critical concepts have been presented with regard to the momentum balance in the jet. When fitting a predetermined function to profile data, the form of the function has crucial signifigance if used to calculate volume flux or kinematic momentum flux integrals across the profile. Next, a momentum balance was derived containing lower order terms. This balance was examined for both a confined and an ideal jet and the general results presented in equation (2.5.8). At this point, the velocity field for the confined jet was decoupled into two components: the turbulent jet and the return flow field. Using the concept of local invariance, a relationship between the volume flux and the local jet momentum flux was

hypothesized. The local momentum flux was shown to be a decreasing function with respect to x and was represented in final form by equation (2.5.17). These predictions will be compared with experimental data in chapter 4. These results, together with the computational work of Seif, will be used to explain the inconsitencies in published literature and suggest empirical profiles for the turbulent jet.

Chapter 3: Experimental Equipment

Section 3.1: Jet Facility

The jet facility used was an adaptation of an existing structure originally constructed to investigate the jet mixing layer. Modifications were made to duplicate the boundary conditions of the jet flow of Wygnanski and Fiedler (1969). This was done not only because we wished to repeat their experiment as closely as possible, but also because we faced the same design criteria. It is desirable to maximize the exit velocity, U_o, since both the exit Reynolds number, Re_o, and the centerline velocity, U_m, measured at a fixed x/D are proportional to U_o. An upper limit on U_o is imposed in terms of the Mach number - we must ensure compressibility effects are negligible. Selecting the exit diameter involves a similar trade off. Recall the appropriate axial length measure is x/D. The smaller the diameter, the smaller the length of the facility. However, Re_o is also proportional to the exit diameter. We also wish the exit area of the jet, A_o, to be large enough so that the boundary layer at the nozzle exit is insignificant when determining the source mass and momentum flux.

The physical dimensions of the jet are shown in Figure 3.1.1. Driving the flow was a 1 h.p. motor and high pressure, paddle type blower. Swirl, spatial inhomogeneities in the mean flow and turbulence intensities

ALL DIMENSIONS
IN INCHES

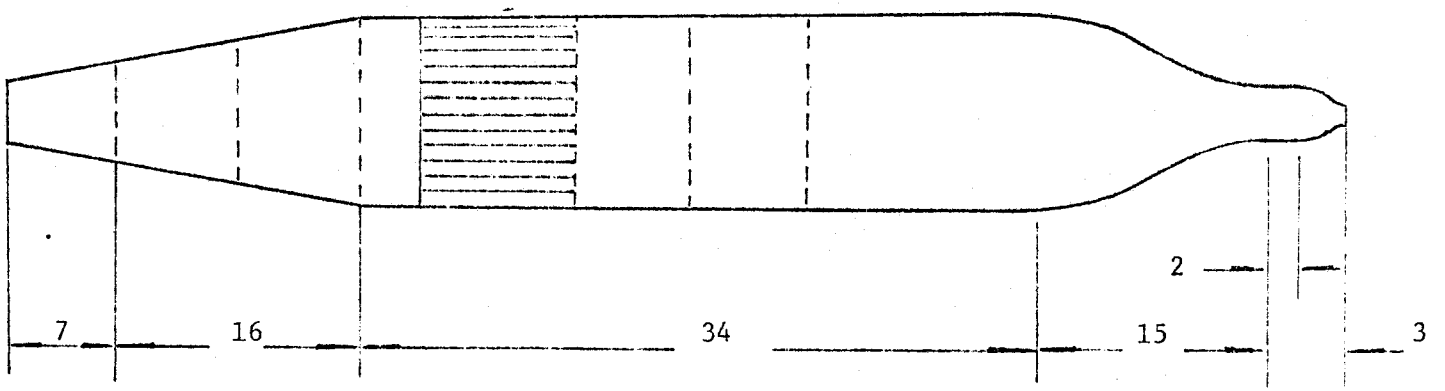

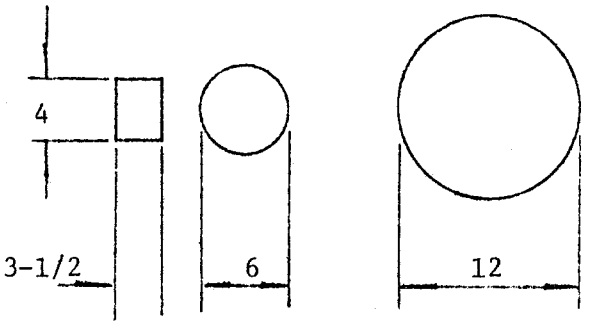

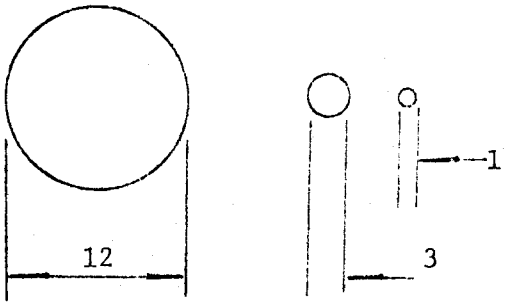

FIGURE 3.1.1

THE JET FACILITY

WIRE SCREENS

PLASTIC STRAWS

were removed using wire screens and one section of plastic straws. The first contraction of 16:1 was from the original facility. Its geometry was two matched cubics optimized for minimum pressure gradient as suggested by Morel (1975). To repeat the conditions of Wygnanski and Fiedler, a second contraction of 9:1 was added to bring the exit to the required one inch diameter. The last contraction was constructed using a fifth order polynomial. As demonstrated by Tan-Atichat (1980), such a curvature produces a more uniform mean velocity distribution over a shorter length. The exit profile is shown in Figure 3.1.2. The measured profile had a velocity overshoot at the jet edges of 3% relative to the centerline velocity. This effect was balanced by the boundary layer thickness (approximately 2% of the exit radius). The error terms arising from the adoption of a top hat profile based upon the centerline line velocity and the exit diameter may be accepted with an error of less then 3%. The exit conditions listed in Table 3.1.1 were used for all experimental measurements reported in this thesis. In chapter four a more serious problem with the facility will be discussed: it is for this reason the exit parameters were not determined with a greater degree of accuracy.

Figure 3.1.3 depicts the construction of the jet enclosure. Our wish to provide a symmetrical enclosure was compromised by construction cost and available physical

TABLE 3.1.1

JET FACILITY PARAMETERS

QUANTITY	SYMBOL	VALUE
EXIT DIAMETER (inches)	D	1.0
VELOCITY (m/s)	U_o	55.0
VOLUME FLUX (m**3/s)	m_o	0.277
MOMENTUM FLUX/UNIT MASS (m**4/s**2)	M_o	1.51
REYNOLDS NUMBER	Re_o	9.2 E+04

A subscript 'o' denotes a boundary condition at the jet exit plane. Abbreviations for units are as follows: 'm' for meters and 's' for seconds. The value for the momentum flux is accurate to within three percent.

FIGURE 3.1.2

JET EXIT PROFILE

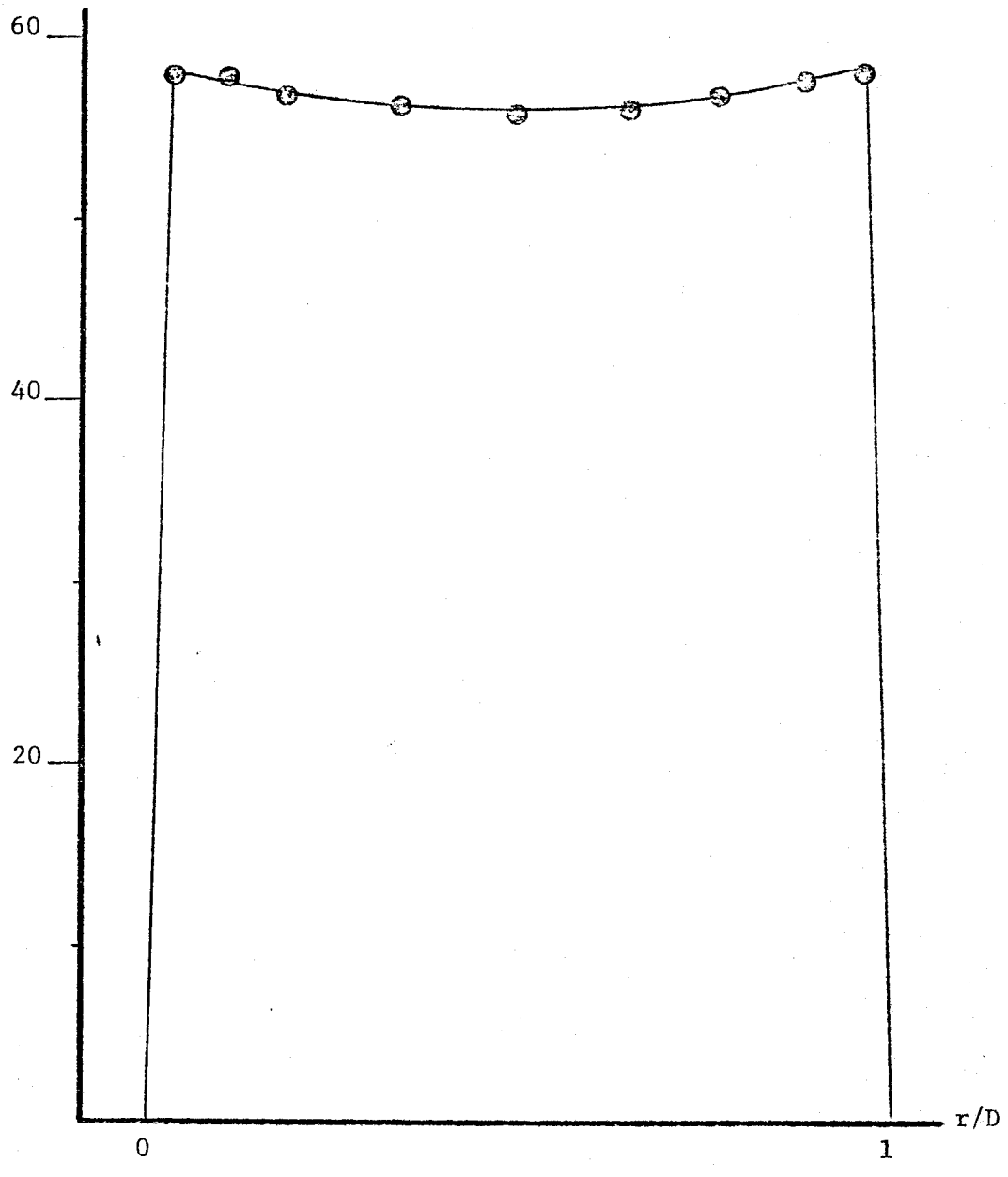

space. The length from the jet exit to the far wall was 21 ft. (about 250 diameters), ceiling height 8 ft., and the distance from jet centerline to the closest wall 5 ft. The jet axis was equidistant from floor and ceiling. The enclosure was sealed in plastic to ensure a uniform seeding distribution. The region at which the measurements were taken is indicated in Figure 3.1.3. Centerline velocity measurements were taken from x/D of 70 to 120. Since it is well established that mean profiles collapses for x/D greater then 20, and the second moments for x/D greater then 70, profiles were measured at an x/D of 71 and 101.* In the non-dimensional radial direction, r/x, these measurements spanned from -0.05 to 0.15.

Section 3.2: Optical and Signal Processing Equipment

The optical package (Figure 3.2.1) was a DISA two-color modular optical system used in a forward scatter mode to maximize signal quality. An Argon-ion model 165 Spectra-Physics laser was mounted on a bench in line with the optical components. The optical configuration utilized the 488 (blue) and 514 (green) nanometer wavelengths. Quarter-wave plates were mounted at the exit of the laser and the entrance of the optics to allow beam rotation. By introducing a 40 MHz frequency shift, the Bragg Cell permitted accurate determination of reverse flow velocities.

---

* Reference the 1969 paper by Wygnanski and Fiedler

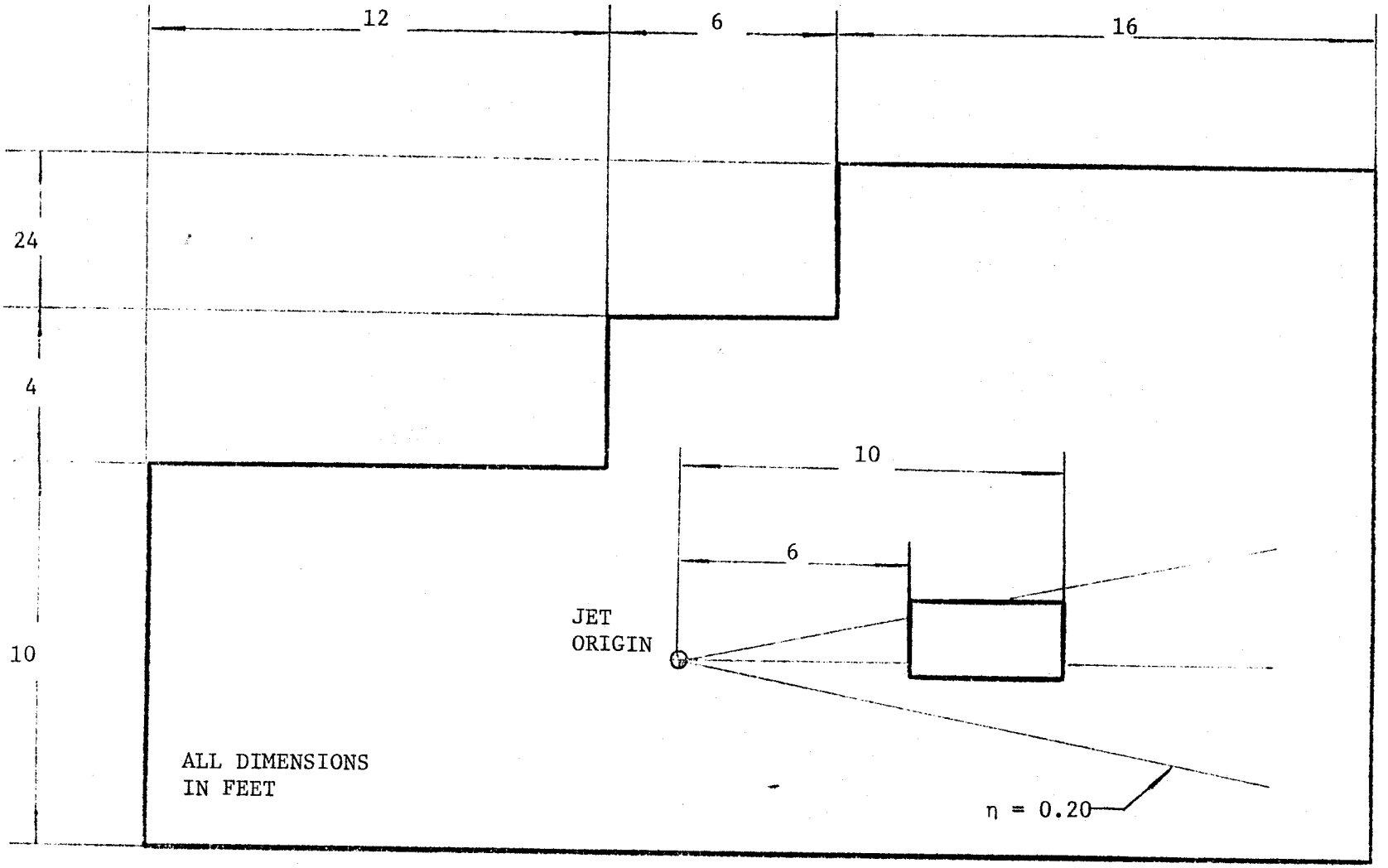

FIGURE 3.1.3

THE JET ENCLOSURE

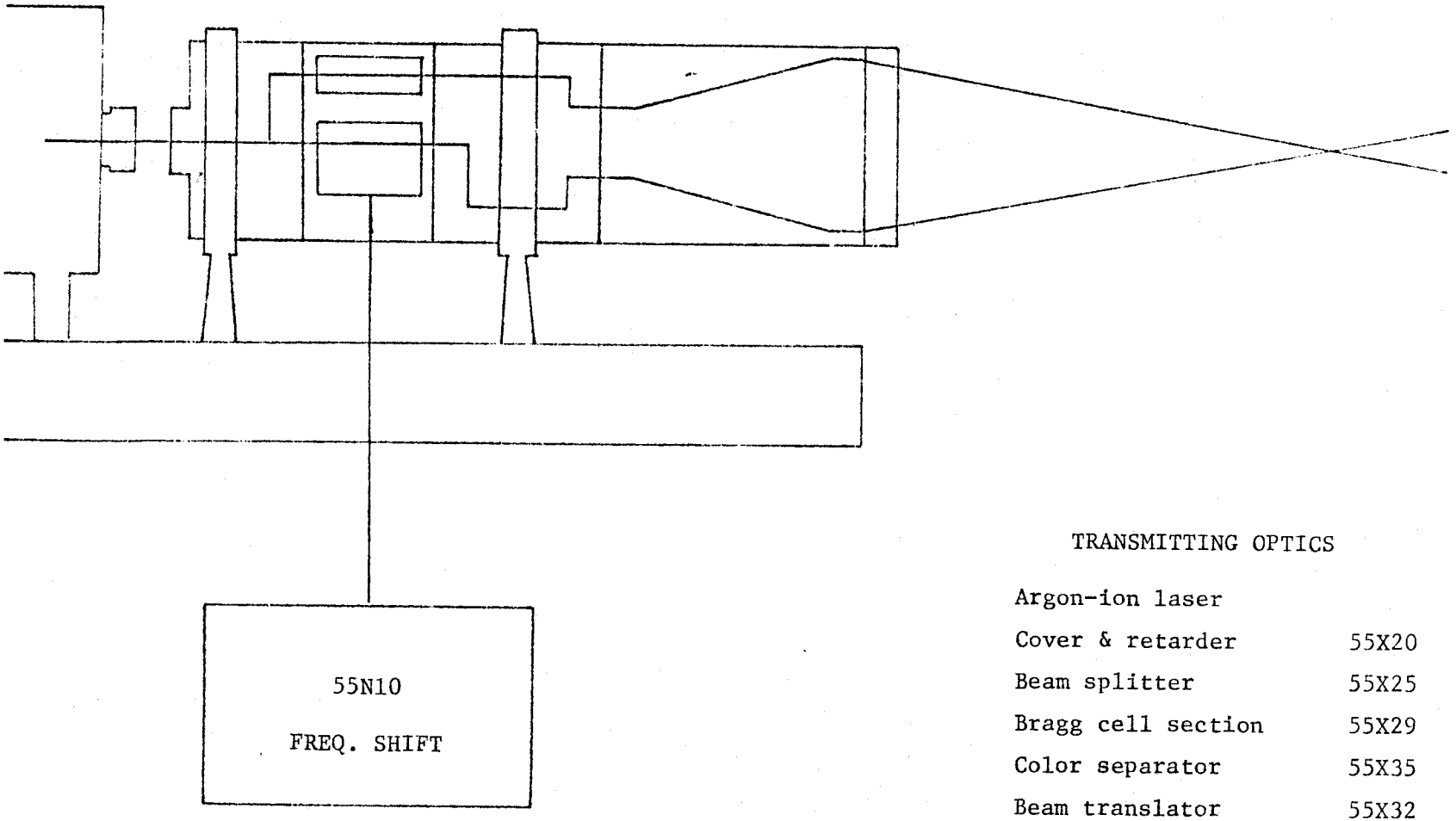

TRANSMITTING OPTICS

Argon-ion laser	
Cover & retarder	55X20
Beam splitter	55X25
Bragg cell section	55X29
Color separator	55X35
Beam translator	55X32
Beam expander	55X12
1.2 meter lens	55X59

FIGURE 3.2.1

OPTICAL PACKAGE

The beam expander enlarged the aperture by a factor of 1.9. As a result, the collected light intensity is approximately multiplied by a factor of 14 and the signal-to-noise ratio increased by 7. All measurements were taken using a 1.2 meter lens. The characteristics of the beam intersection volume are given in Table 3.2.1. Since the receiver optics were mounted close to the optic axis, the measuring volume defined by the pin hole of the receiving optics is coincident with the beam intersection volume. The values listed in Table 3.2.1 may thus be considered valid approximations for the measuring volume size.

The optical bench and laser were mounted on a manual traversing system with two degrees of freedom in the horizontal plane. The limits of the traverse system were identical to the range over which measurements were taken. This equipment was placed within the enclosure.

The particle seed used was glycerin smoke. This was generated using a heater element in a vessel of glycerin. The seed concentration was monitored from the data acquisition rate and monitor output on the counter equipment. These outputs were used to manually adjust the seed generation rate.

The signal processing equipment (Figure 3.2.2) also consisted of DISA components. Each output from the two photo-multiplier tubes was individually shifted using a 55N10 Frequency Shifter. For the frequency ranges

TABLE 3.2.1

PARAMETERS OF BEAM INTERSECTION VOLUME

QUANTITY	VALUE	UNITS
BEAM INTERSECTION ANGLE	2.60	degrees
BEAM WAIST DIAMETER	.31	mm
PROBE VOLUME LENGTH	16.	mm
FRINGE SPACE	10.9, 11.5	m
FRINGE NUMBER	28	
CALIBRATION FACTOR	10.9, 11.5	(m/s)/(Mhz)

Abbreviations for units are as follows: m - micrometers, mm - millimeters, m - meters, Mhz - megahertz, s - seconds.

SIGNAL PROCESSING EQUIPMENT

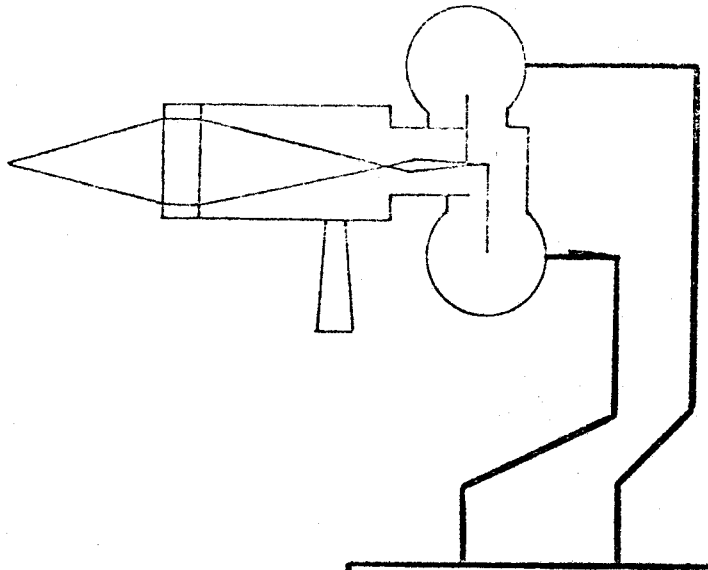

55N10
FREQ. SHIFT

55L90a
COUNTERS

OSCILLOSCOPE

57G149 COINCIDENCE
FILTER

57620 BUFFER AND
INTERFACE

PDP 11/34

TERMINAL

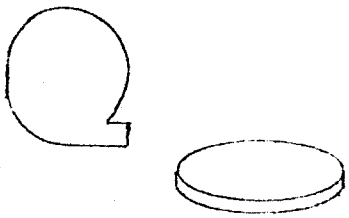

TAPE OR DISK STORAGE

encountered in this experiment, the resultant incremental shift was 100 KHz, corresponding to a fringe velocity of approximately 1.1 meters/second. Following down shifting, the signals were sent to two 55L90a counters. During the course of the experiment, all measurements were taken in the combined mode. This made available in digital form the burst time for eight fringes (P_8), the total fringe count (N), and the sample interval between successive samples (T). The output of the counter was interfaced to the computer using a DISA 57G20 Buffer Interface. The 57G149 Coincidence Filter Board was included in the interface and was progammed as an additional validation device. It ensured that the measurements successively stored in the buffer from each counter were coincident in time and from the same particle. This permitted an instantaneous realization of the Reynolds stresses and filtered out invalid samples. Additional information on signal processing equipment and methods is presented in chapters seven to nine.

Data was transferred using a parallel interface to a DEC PDP 11/34 minicomputer. The minicomputer was used both to store and process the data. A 16 bit machine, it was capable of an accuracy of roughly 7 decimal digits for a single precision variable and 17 digits for double precision. The operating system was RSX11M.

Chapter 4: The Jet Measurements

Section 4.1: Centerline Velocity Values

The starting point in the evaluation of the jet data is the centerline velocity decay rate. As previously mentioned (see equation 2.2.10) the centerline velocity value, U_m, is inversely proportional to x. Since almost all authors to date have chosen to express the centerline decay rate in terms of the jet exit velocity, U_0, and exit diameter, D, that nondimensionalization is adopted. It is again emphasized that on the basis of section 2.3 (in particular, equations 2.3.5 and 2.3.6) such scaling is not the most appropriate way to scale turbulent jet data. It is useful in collapsing data only when the jet source is a circular jet with a uniform velocity (top hat) profile. When presented in this form, the data cannot be contrasted with that from jets with different source conditions. However, since the primary purpose of this dissertation is to identify the errors present in existing data, the data is presented in its original form to avoid confusion.

If the ratio of the centerline velocity to the exit velocity, U_m/U_0, is selected as the dependent variable, a 1/x dependence would be displayed on the plot. This is an inappropriate selection of variables, since far downstream of the jet the dependent variable would quickly approach zero and the plot would provide little visual information.

Instead, the inverse, U_o/U_m is chosen as the dependent variable since this value is directly proportional to the downstream position and the resulting plot is a straight line. The following curve is expected

$$\frac{U_o}{U_m} = \frac{1}{B_U} \left(\frac{x'}{D} - \frac{x_o}{D}\right) \qquad (4.1.1)$$

As defined in Figure 2.2.1, the number of exit diameters from the jet exit, x'/D is the independent coordinate. Recall the distance from the virtual origin is the difference between x'/D and x_o/D. When plotted in these scales, the virtual origin is the intercept with the independent axis when the straight line describing the decay rate is projected back to the origin. The data when plotted in this manner are shown in Figure 4.1.1. The straight line behavior of the points is evident, thus confirming the 1/x dependence of the centerline velocity. All of the measurements agree to an x/D of 60. Note that past this position, the data of Wygnanski and Fiedler begins to deviate from the straight line behavior as established by data points closer to the origin. The LDA data taken during this investigation shows similar behavior, although the deviation occurs farther downstream. Only Rodi's data is consistent in its straight line behavior, although no data are reported beyond $x'/D = 80$. In their paper, Wygnanski and Fiedler explained this behavior as follows:

> 'Judging from the mean velocity (profile) alone, it would appear that the jet is already self-preserving at some 20 nozzle

FIGURE 4.1.1

CENTERLINE VELOCITY DECAY

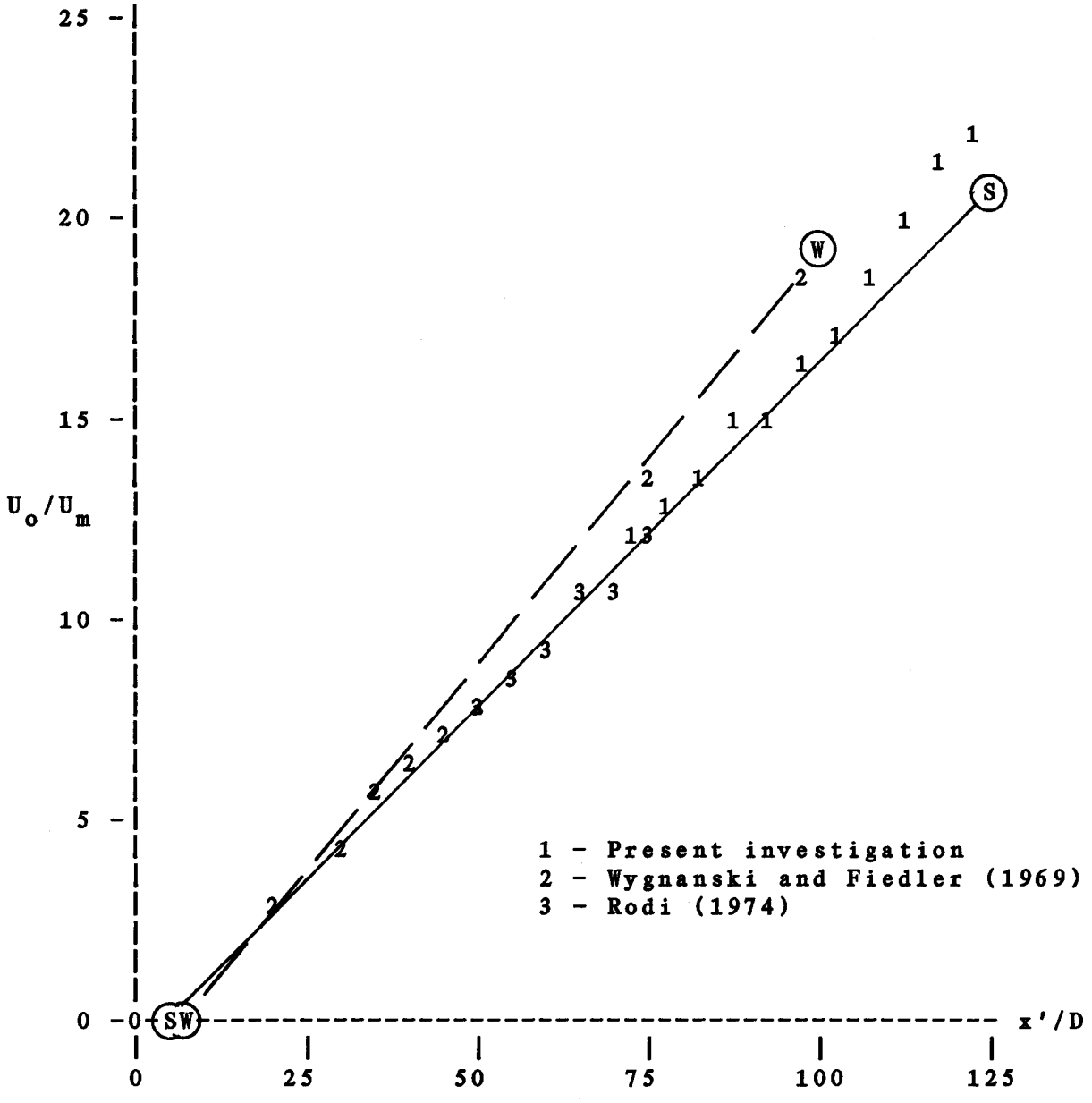

Seif's predicted decay rate ('S', solid line) is plotted using a virtual origin four diameters downstream and his recommended value of B_U = 5.8. Value of centerline decay suggested by Wygnanski and Fiedler ('W', dashed line) is for a virtual origin seven diameters downstream and B_U = 5.0

> diameters downstream of the nozzle. If the measurements were concluded at x/D<50 the hypothetical origin of the flow would appear to be located 3 diameters in front of the nozzle. Taking into account measurements at x/D>50, the hypothetical origin was moved to 7 diameters in front of the nozzle. A similar observation was made by Townsend (1956) for the small-deficit wake, and it may be concluded that the rate of growth of the jet is sensitive to conditions of self-preservation, while the shape of the normalized velocity profile is not.'

The authors of this paper did not document a value for the decay rate, so their value of B_U=5.0 has been approximated from the straight line as drawn on their plot for centerline values. This exact value of this constant is obviously controversial, for Hinze's text believes it to be B_U=5.4. For values of x/D<50, Hinze cites B_U=5.9 as the correct value to be read from Wygnanski's and Fiedler's data. The confusion present in what should be a well accepted value becomes more apparent when Rodi's paper is read. Concerning the centerline decay and his measured values, Rodi writes

> 'The data points follow the linear distribution required by the theory for self-preserving flow. The virtual origin is at x/D=4. Except for a small shift in the virtual origin, Wygnanski and Fiedler's results obey the same decay law down to x/D=57, when the slope of their decay curve changes. This is difficult to understand.'

Rodi's paper fails to document any further explanation for this phenomena. This paper also fails to document a specific value for the constant describing the centerline decay, thus increasing the confusion.

How serious is this departure from straight line behavior? Since the ratio of the exit velocity to centerline velocity is higher than predicted, the value of the centerline velocity is lower than would be expected. Obviously, this effect has serious consequences in the momentum constraint.

The importance of the centerline decay rate to momentum conservation can be seen another way. Since the normalized profile of Wygnanski and Fiedler collapses satisfactorily for an $x/D>20$ the jet half-width should be a well established constant for any axial position past this location. Therefore instead of U_o/U_m, B_U is chosen as the dependent variable as shown in Figure 4.1.2. The data points should fall on a horizontal line. For now, focus on the value of B_U as predicted for the virtual origin recommended by Wygnanski and Fiedler ($x_o/D=3$). Even if one allows for significant error in the retrieval of their data from the published figures, there is a clear tendency for B_U to decrease with downstream distance. If B_U is decreasing while the jet half-width remains constant, momentum is being lost (see equations 2.3.10 and 2.4.13). As an example, calculating B_U at an x/D of 50 and 98 based on a virtual origin of seven diameters gives a value for B_U of 5.4 and 5.0 respectively. This 8% difference in B_U indicates a 16% drop in momentum between these two locations. The continuous drop in the value of B_U implies

FIGURE 4.1.2

EFFECT OF VIRTUAL ORIGIN ON DATA OF WYGNANSKI AND FIEDLER
MODIFICATION OF CENTERLINE DECAY RATE

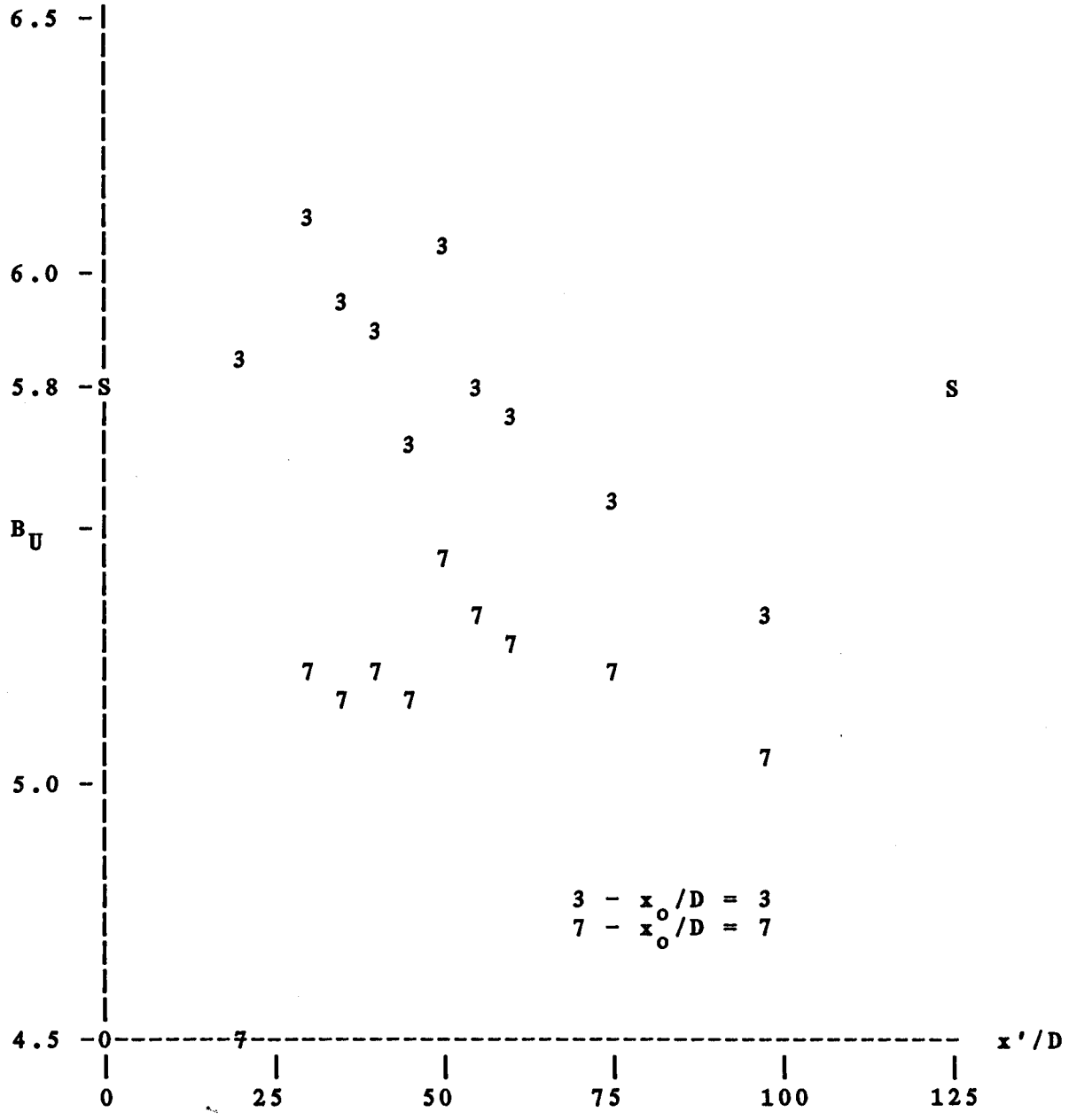

an increasing amount of lost momentum as one goes downstream! It is suggested that this shift away from the initial centerline decay rate and the subsequent loss of momentum is due to the return flow difficulties as predicted in section 2.5.

If this is so, then the centerline decay constant measured by Wygnanski and Fiedler in the initial region of the jet is near the correct value. If a virtual origin of x_o/D equal to three is accepted instead of x_o/D equal to seven, the values of B_U will increase. The jump in the predicted value of B_U is shown by those points labeled '3' in the plot. This small shift in the virtual origin increases the value of B_U by 10% at an x'/D of 40 to 4% at an x'/D of 98. In terms of the momentum integral, this implies a jump of 20% and 8% respectively. Note that even with these changes in interpretation the asymptotic forms are missing 15-20% of the momentum. This loss can only be related to the profile itself. This will be discussed later in detail

Results from all three investigations along with the theoretical prediction of Seif are shown in figure 4.1.3. Rodi's value of B_U=6.0 is in good agreement with the corrected value of Wygnanski and Fiedler of 5.9. The LDA data taken during the course of this investigation has a slightly lower value of B_U, agreeing with Seif's predicted value of 5.8. The lower value of B_U indicates lower

FIGURE 4.1.3

VALUES FOR CENTERLINE DECAY RATE

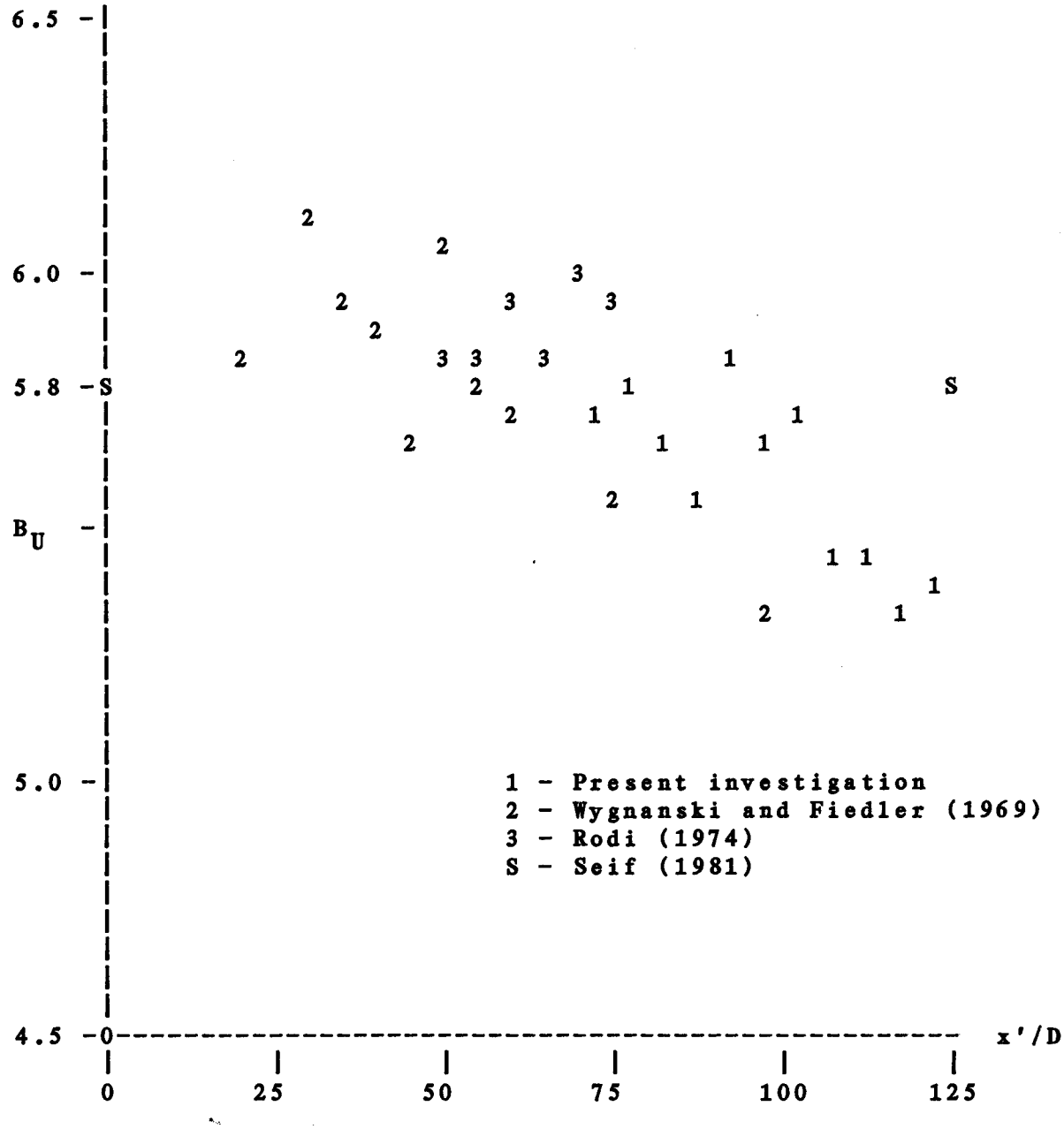

values for the centerline velocities than predicted by the CTA measurements, a fact which is consistent with the amount of the crossflow contamination on hot wires at turbulence intensities corresponding to the jet centerline.

Section 4.2: The Mean Velocity Profile

The mean velocity profile, normalized by the centerline velocity, is presented in Figure 4.2.1. The data of Wygnanski and Fiedler and of Rodi are in excellent agreement with each other so their values are represented by the single curve labeled 'W'. The line representing Seif's numerically generated profile has been labeled with an 'S'. The LDA measurements from this investigation were taken at an x/D of 70 and 100.

Rodi's paper suggests 0.086 as the appropriate half-width value for the jet profile. Recall the corrected centerline decay rate of Wygnanski and Fiedler (B_u = 5.9 instead of 5.0) matches that of Rodi. Seif has shown that for their data, the mean axial velocity term in the momentum constraint accounts for 77% of the source momentum. An exact breakdown of the momentum balance is shown in Table 4.2.1. When all the terms in the momentum constraint are evaluated, roughly 16% of the source momentum is missing for Rodi's measurements and 40% for the uncorrected (see preceeding section) data of Wygnanski and Fiedler.

FIGURE 4.2.1

MEAN VELOCITY PROFILE

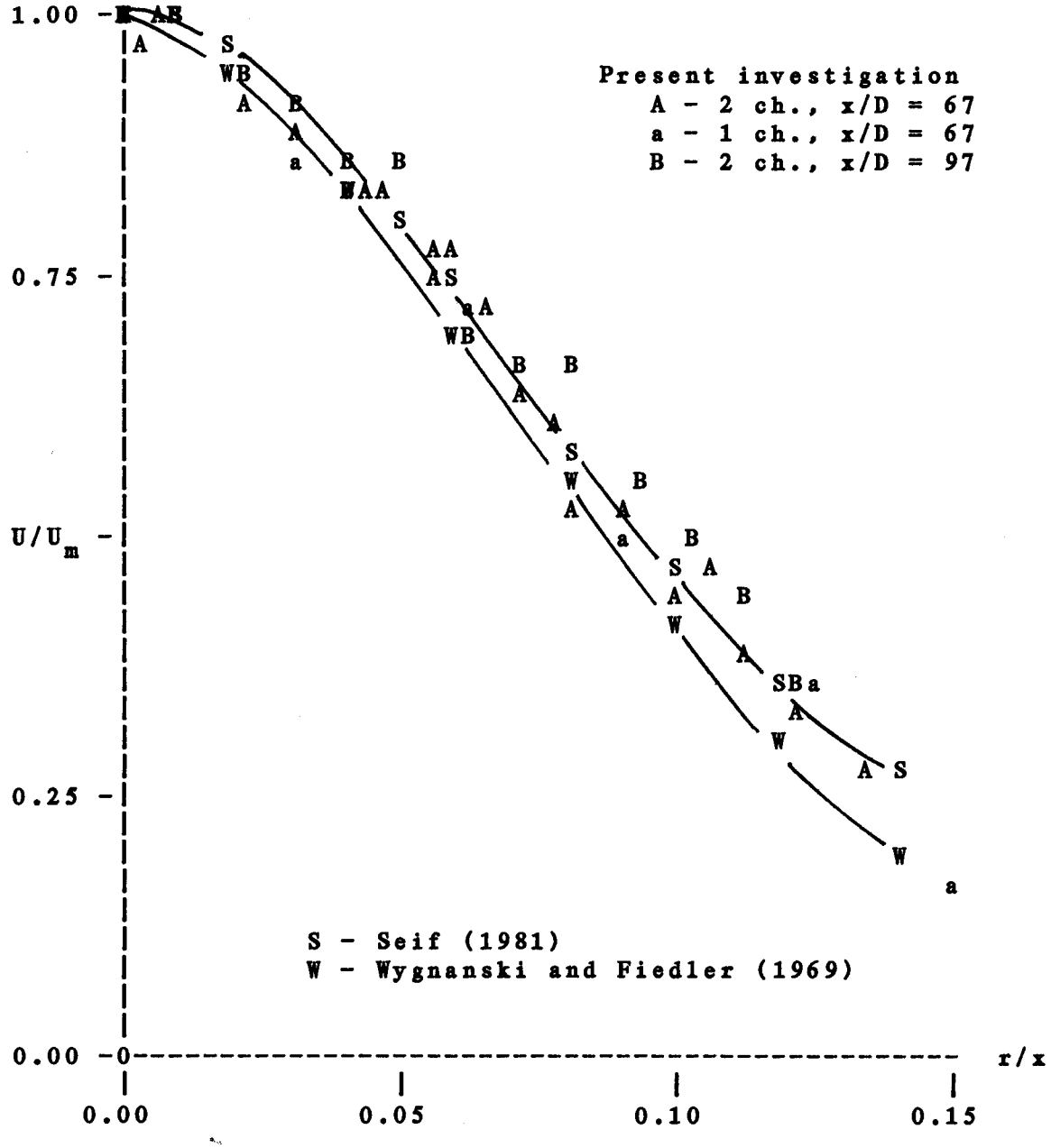

Although there is considerable scatter in the LDA measurements, they indicate a wider profile than the other data. There is also a slight tendency of the data to widen at an x/D of 100. Given the scatter in the data of $\pm$2% near the centerline, this behavior can be attributed to a selection of a centerline velocity which is too low. Further discussion concerning error estimates will be introduced later. The LDA data does match the suggested profile of Seif, so his half-width prediction of 0.095 is recommended. With a centerline decay rate of $B_u = 5.8$ and a half-width of $\eta_{1/2} = 0.095$, the LDA data satisfies the momentum constraint to within the 3% accuracy limits of the investigation (c.f. section 4.4). Note that since v^2 was not measured directly it was assumed to be equal to w^2, a fact consistent with the earlier measurements.

These results present one critical question. It is expected that mean values computed using LDA techniques are in general lower than CTA methods (see Buchhave 1980). The centerline velocity values display this pattern (see Figure 4.1.3 and recall that a lower value of B_u implies a lower velocity value). Why then is the LDA profile wider than those taken using CTA measurements? At this point, a completely satisfactory answer has not been formulated. It is possible to justify these LDA measurements through the momentum constraint, for if the centerline decay rate of $5.8 < B_u < 6.0$ is accepted the jet profile must have a half

width around $\eta_{1/2} = 0.095$ to conserve momentum.

One possible explanation for Wygnanski and Fiedler's profile being narrower is that because of the back flow, the flow was not really a jet, a fact consistent with the momentum loss. Drawing quantitative facts from their profile becomes even more questionable if one accepts that their virtual origin was off by four diameters. If this is true, then the value of x would be incorrect in their profile plots with serious consequences for those profiles measured closer to the source. It becomes questionable if their profiles do in fact collapse! Rodi's profiles, on the other hand, do collapse which would seem to indicate that the problem is intrinsic to the hot-wire technique, although a straightforward examination of the effect of cross-flow errors on a hot-wire always leads to positive errors. Hussain (1981) in a private communication has discussed measurements of the jet in which the momentum appears to be greater than that added at the source. This is, what would be expected from hot wire measurements.

Section 4.3: The Turbulent Velocity Fluctuations

To complete the analysis of the momentum constraint, only the normal turbulent stress terms need be considered. These terms are normalized by the square of the centerline velocity. Both components do not roll off as fast as the mean velocity, staying roughly constant out to $\eta = 0.06$.

The axial component is plotted in Figure 4.3.1. Based on the current investigation, the centerline value for the turbulence intensity, u/U_m, is 27%. Both Rodi and Wygnanski and Fiedler measured slightly higher values of 28% to 29%, the difference again being attributable to the cross flow errors on the CTA results. Unlike the earlier measurements, the present results show a pronounced off-axis peak. Buoyant plumes also exhibit this behavior which can readily be attributed to the production of turbulent kinetic energy caused by the higher shear rates off the jet centerline (Beuther 1980).

For the most part, the LDA turbulence measurements show good agreement with the hot wire results. This is consistent with the observations of Buchhave (1979) where the primary differences between the LDA and CTA were in the mean velocity results whereas the streamwise velocity fluctuations were quite similar.

The values for the azimuthal normal turbulent stress, w^2, are plotted in Figure 4.3.2. These values agree quite well with Rodi's results, but do differ from those of Wygnanski and Fiedler's. The agreement with Rodi's data can be explained by the the improved methods used to minimize for the cross flow errors and to perform the angle calibration. Seif's predictions are only slightly higher than those of the current investigation. These measurements indicate a centerline turbulence intensity, w^2/U_m^2, of

FIGURE 4.3.1

AXIAL COMPONENT OF REYNOLDS STRESS

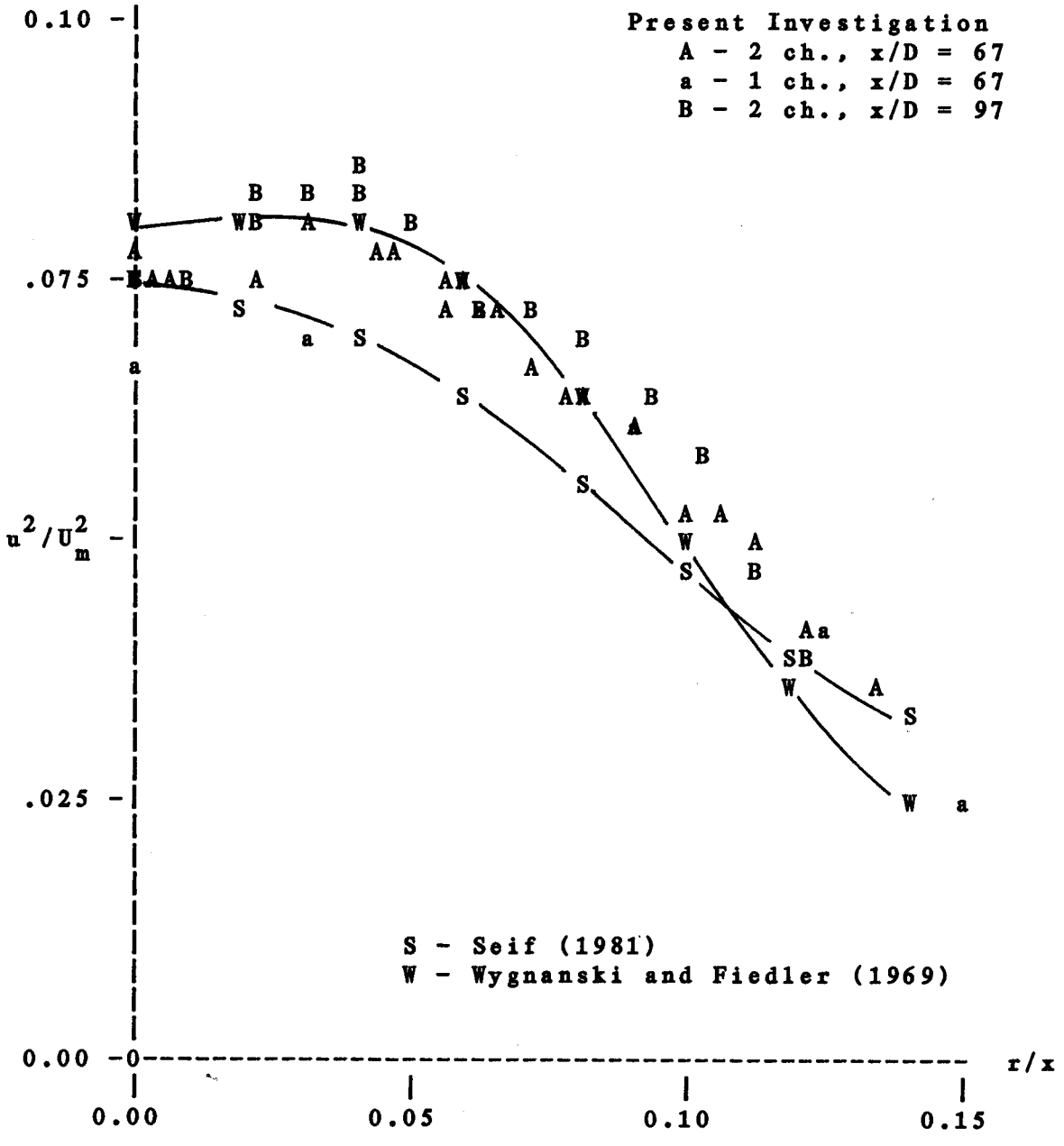

FIGURE 4.3.2

AZIMUTHAL COMPONENT OF REYNOLDS STRESS

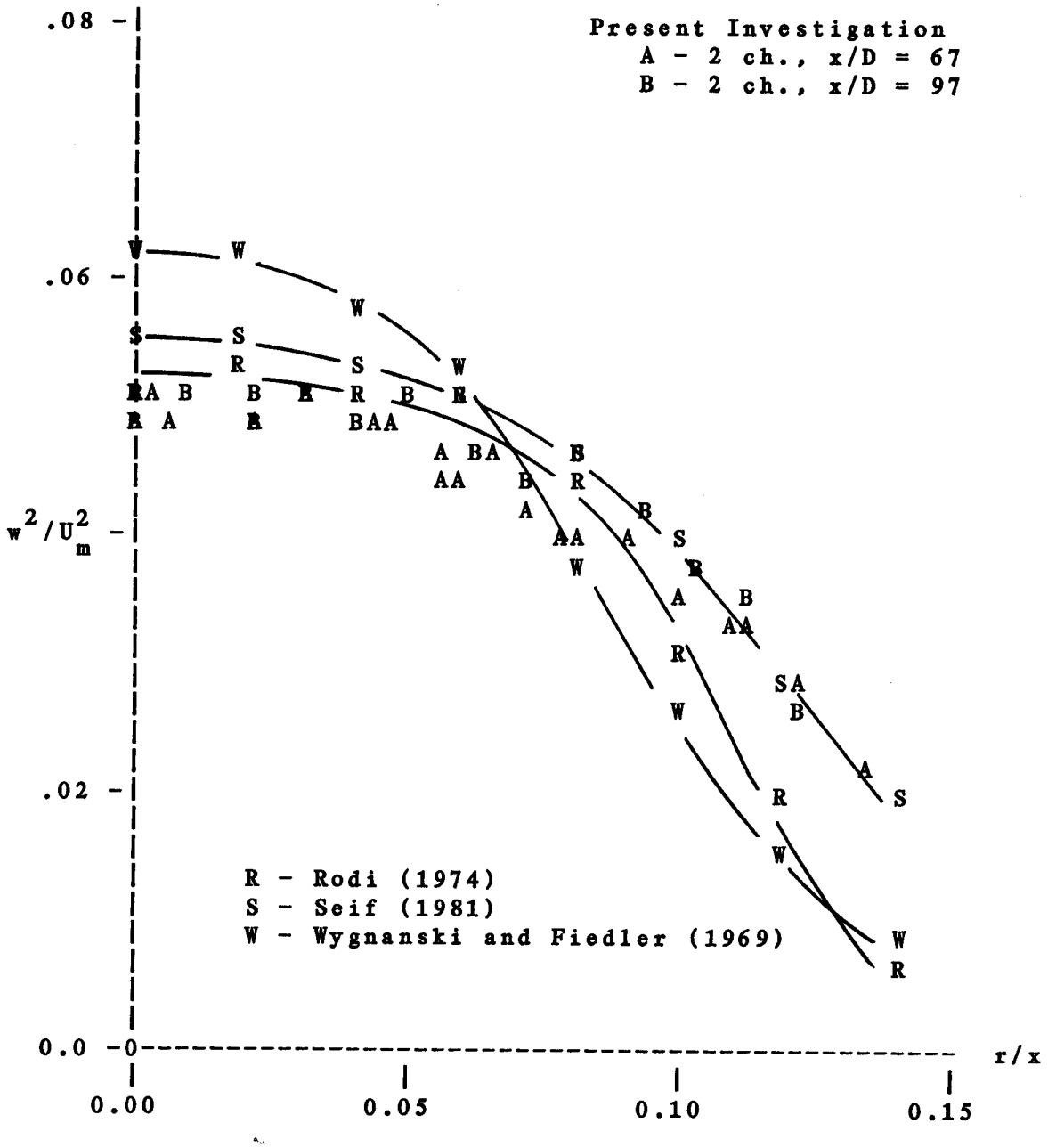

22% to 23%.

Section 4.4: The Momentum Constraint Evaluation

It is now possible to complete the momentum integral. The LDA mean profile, which is in agreement with Seif's theory, holds 92% of the source momentum. The axial component of the normal turbulent stress, which is only slightly higher than that of Wygnanski and Fiedler and Rodi, would contribute 19% of the momentum. The remaining normal stress terms subtract from this quantity. The azimuthal component, agreeing with Rodi's measurements, is roughly 10%. Assuming the radial component contributes the same amount, their net contribution is approximated as 10%. The balance is too high by only 1%, an amount well within the experimental error.

Section 4.5: The Effect of the Return Flow

At this point, it is appropriate to reexamine the analysis of the momentum loss caused by the return flow. From section 2.5, the momentum constraint for a confined jet is given by

$$M(x) = \frac{M_o}{((1 + (2/\pi)K^2 (x/D)^2(A_o/A_R))} \qquad (4.5.1)$$

Where A_o is the jet exit area, A_R the 100 m area, and K a constant relating the mass flux to the local momentum flux (see equation 2.5.13). It is unfortunate the

ratio A_o/A_R cannot be exactly determined for any of the experiments. The enclosure used by Wygnanski and Fiedler was a wire cage with a cross-sectional area of 8 ft. x 7.5 ft. It is therefore impossible to accurately predict the interplay between entrainment through the screen and return flow inside the screen. The facilities used in this investigation present similar problems of interpetation. The LDA experimental investigation was concluded before the development of the confined jet theory. The sealed enclosure was designed around available floor space in the laboratory in conjunction with the spatial requirements of the laser and traverse system. As a consequence, the room's cross-sectional area was not constant. Still, rough approximations can be made. Environmental conditions are summarized in Table 4.5.1. Note Wygnanski and Fiedler have the least favorable ratio of A_o/A_R, thus explaining why their measurements begin to lose momentum first. Although data on Rodi's enclosure was unavailable, it should be noted that his exit diameter/area was one half/fourth that of Wygnanski and Fiedler. This probably explains why Rodi's centerline data displayed consistent centerline behavior.

It is possible to make a correction for the confined jet effects on the centerline data? Begin with the ideal jet, where the mean velocity is isolated from the turbulent stress terms in the momentum constraint. This is accomplished by defining Q as that fraction of the momentum

TABLE 4.5.1

PARAMETERS OF EXPERIMENTAL ENCLOSURE

	D	A_R	A_o/A_R
Rodi	0.5	?	?
Wygnanski and Fiedler	1.0	7.5 X 8	9 X 10-5
Present investigation	1.0	10 X 14	5 X 10-5

The exit diameter, D, is expressed in inches. The dimensions of the room are in in feet. The enclosure of Wygnanski and Fiedler was wire cage, making exact determination of an effective room area impossible. The current investigation faced similar difficulties since the room cross section varied with axial position.

constraint contributed by the mean axial velocity.

$$M_o = Q \int_0^\infty U^2 \, 2\pi r \, dr \qquad \text{ideal} \tag{4.5.2}$$

For a polynominal fitted to a half-width of $\eta_{1/2} = 0.095$, and equation (2.3.10) is thus modified to

$$M_o = 2.53 \, (B_M \eta_{1/2})^2 \, Q \qquad \text{ideal} \tag{4.5.3}$$

This procedure is repeated for the confined jet. Again Q is that fraction of the momentum constraint contributed by the mean axial velocity. For both the ideal and confined jet, Q is assumed to be the same constant value

$$M(x) = Q \int_0^\infty U^2 \, 2\pi r \, dr \qquad \text{confined} \tag{4.5.4}$$

$$= 2.53 \, (B_m^* \, \eta_{1/2}^*)^2 Q$$

The superscript '*' indicates data taken from the confined jet.

In Wygnanski and Fiedler's measurements, the profile seems to continue to scale in similarity variables even though the centerline decay rate has been strongly influenced by the backflow. Even allowing for the uncertainty in the virtual origin and its effect upon the profile, the major effect of the return flow seems to be in the magnitude of the profile but not its shape. Therefore, it seems reasonable to assume that

$$\eta_{1/2}^* = \eta_{1/2} \tag{4.5.5}$$

It now remains only to relate the decay rate constant

B_M^* as measured in the confined jet to the value of B_m for the ideal jet. This can be done by using the results of the momentum constraint analysis.

$$M(x) = 2.53\ (B_m^* \eta_{1/2})^2\ Q = \frac{M_o}{(1 + 2/\pi\ K^2 (x/D)^2\ (A_o/A_R)} \tag{4.5.6}$$

Substitute equation (4.2.3) for the source momentum, M_o. After cancelling common terms, the resulting expression relates B_U to B_U^*.

$$B_U^* = \frac{B_U}{(1 + 2/\pi\ K^2 (x/D)^2 (A_o/A_R))^{1/2}} \tag{4.5.7}$$

As expected, this expression indicates that for the confined jet, the centerline decay rate constant will be underestimated. Since B_U and B_M are directly proportional (see equation 2.2.10) this relation holds regardless of the dimensional form in chich the centerline decay rate constant is formulated. The final form for an equation to correct for the effect of the enclosure is

$$B = B^* (1 + (2/\pi)\ K^2 (x/D)^2 (A_o/A_R))^{1/2} \tag{4.5.8}$$

Values for the centerline decay rate corrected using the above scheme for data taken in a confined jet is shown if Figures 4.5.1 and 4.5.2 The constant value relating the mass flux to the momentum flux is calculated using equation (2.3.11) and a Gaussian fit based on Seif's results. This would underestimate K and the effect of the return flow on B. Enclosure values are those listed in Table 4.5.1. It is

FIGURE 4.5.1

CONFINED JET CORRECTION TO CENTERLINE DATA
WYGNANSKI AND FIEDLER (1969)

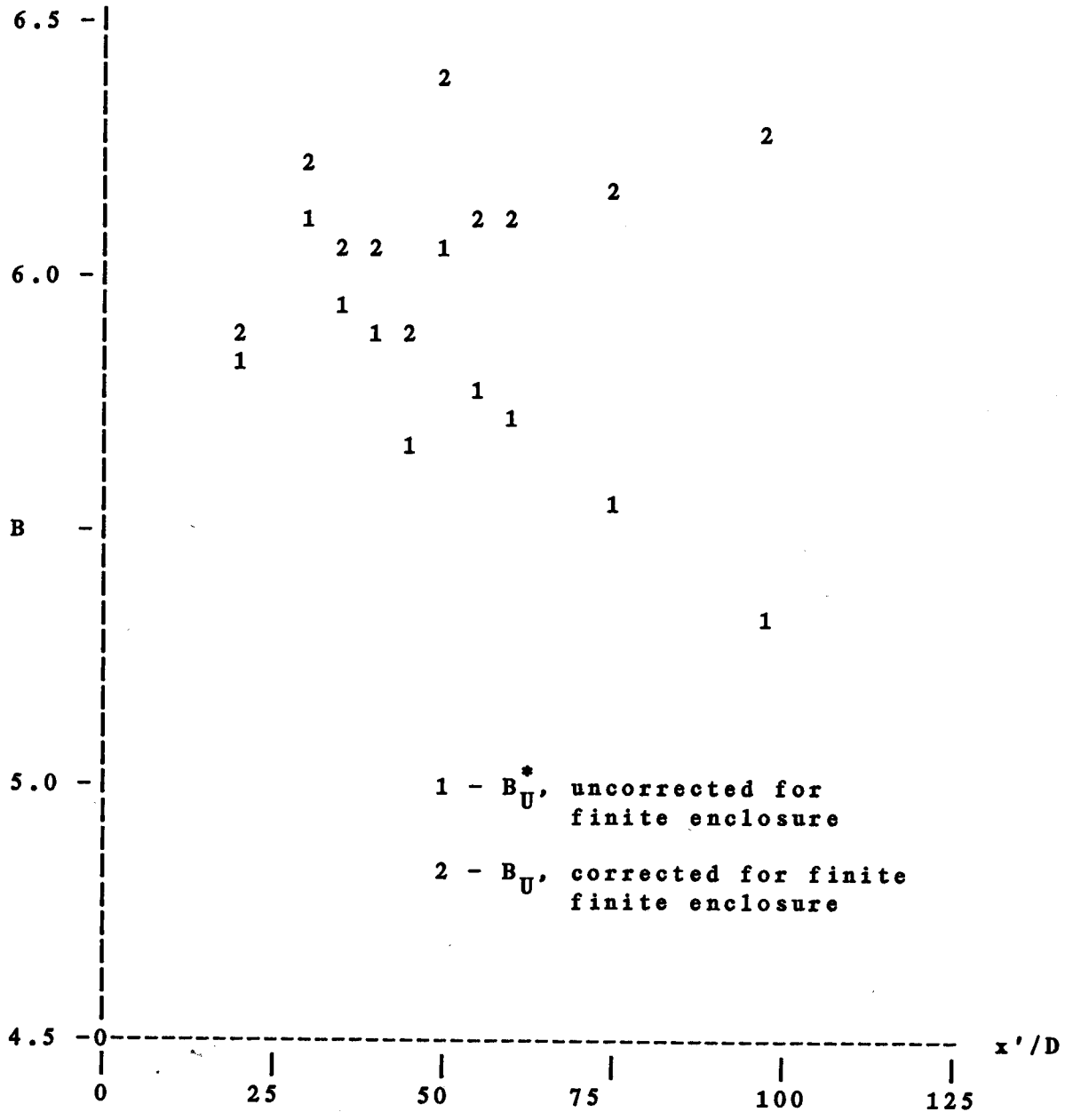

FIGURE 4.5.2

CONFINED JET CORRECTION TO CENTERLINE DATA
PRESENT INVESTIGATION

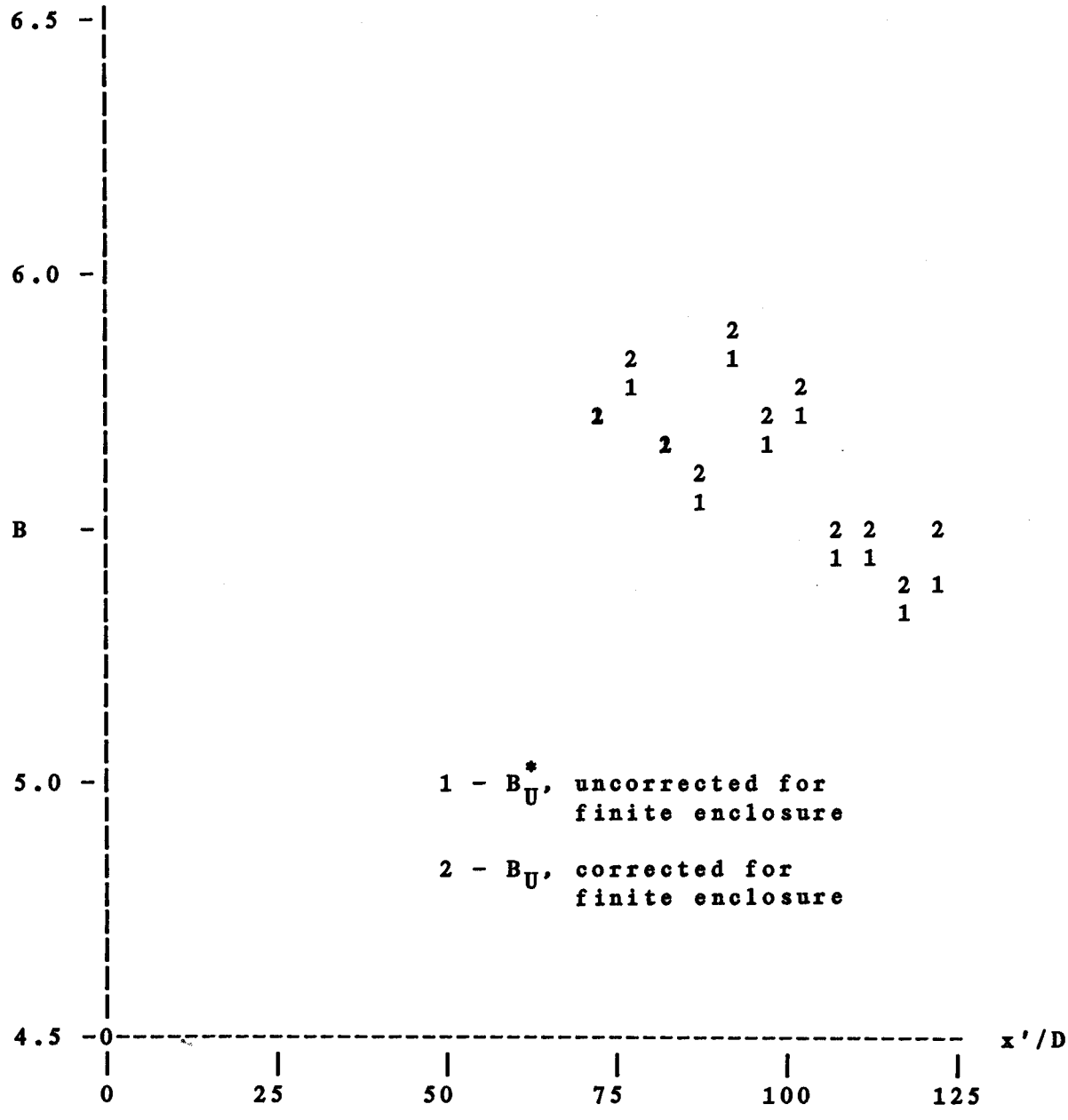

difficult to make qualitative judgements based on this scheme. When applied to the data of Wygnanski and Fiedler, the method seems to overestimate return flow effects. This is expected, for their experiment was not completely sealed. Corrections to the current investigation seem to underestimate the backflow effect. This is suprising, since the selected room area was chosen to maximize backflow effects (i.e. the narrowest area of the room was selected). Based on these results, the anslysis of the confined jet seems to have a limited qualitative application. It is however, the only model available by which one can design an enclosure for jet experiments. If the enclosure is large enough so that the denominator of equation (4.5.7) is one, there is no effective difference between the ideal and the confined jet.

Section 4.6: Concluding Statements on the Experimental Results

In conclusion, the LDA measurements at an x/D of 70 and 100 have been shown to satisfy the momentum constraint even though this flow shows evidence of being contaminamted by the return flow for x/D greater than 100. The major difference between the LDA results and the CTA techniques is found to be in the measurement of the width of the mean profile. Although both Rodi and Wygnanski and Fiedler have measured jet half-widths of $\eta_{1/2} = 0.86$, the results of this current experimental program suggest a value closer to

0.095. It is not yet clearly understood why the CTA techniques should produce a narrower velocity profile since previous experience would suggest the opposite. A centerline decay rate of $B_U = 5.8$ is recommended versus the corrected value for Wygnanski and Fiedler of 5.9 and Rodi's value of 6.0. This discrepency in values is believed due to cross flow errors on the CTA instrumention.

PART II: ANALYSIS OF THE LDA TECHNIQUE

Chapter 5: Introduction to Part II: Analysis of the LDA Technique

Within the past decade, LDA counter measurement techniques have seen widespread acceptance. Their quick adoption by the experimentalists is due to a number of reasons. It's calibration is linear, and is only sensitive to one velocity component. In addition, if equipped with frequency shift, it is capable of sensing reverse flow. As a final benefit, the LDA is non-invasive, it does not disturb the flow patterns. Because of these characteristics, the LDA is the only measurement tool capable of providing answers in many primary research areas. LDA systems have been used for measurements in recirculating flow, combustion studies, internal combustion engine studies, two-phase flows, rotating machinery, and capillary blood flow. The introduction of complete LDA systems by commercial manufacturers has permanently established them as a primary tool in the study of fluid mechanics.

Unfortunately, although the LDA is an extremely versatile tool, it is also more complicated then conventional CTA techniques. Unfortuantely, measurements may be corrupted through errors arising from a wide variety of sources. For a newcomer to the field, proper alignment of the optics may sometimes appear to be more of an art than a science and the improper adjustment of the optics may result a high noise signal. Incorrect settings on the

hardware can lead to angular bias. Particle size and seeding distribution may contaminate LDA measurements. Because of the many aspects associated with the implementation of burst processing, the second part of this dissertation has been designed in part as a primer for the novice in LDA measurements. In addition, suggestions are made by which one can judge the quality and accuracy of LDA measurements.

The first chapter begins with a review of the LDA hardware and defines the basic functions of the components in an LDA system. The next chapter introduces the major sources of bias or error in LDA measurements. First, it must be determined if the particle follows the flow. Section 7.2 gives guidelines for the selection of an optical package. Because the particle arrival rate is dependent upon the velocity field, a simple arithmetic average cannot be relied upon to evaluate the flow field. Instead, residence time weighting must be used. A rigorous derivation for this technique is reviewed in section 7.3. In the succeeding section, Buchhave's (1979) investigation of angular bias is summarized. Criteria for the correct selection of the amount of frequency shift is presented here. In the remaining two sections of chapter seven, the accuracy of the counter hardware is evalnated.

The purpose of the final chapter is to present various methods by which one can judge the signal quality of an LDA

system. To begin, Buchhave's analysis of particle path lengths in in the optical probe volume is reviewed. His results are then used to derive a probability distribution function for counter statistics in a uniform laminar flow. To extend these results to turbulent flows, the distribution function is viewed as a conditional probabilty distribution function. On the basis of this development, the distribution function of the fringe count and its applications are discussed in section 8.4. Other techniques to gain a qualitative impression of the signal quality is discussed in section 8.5. In addition, qualitative measurements of particle concentration are also given. The final section summarizes the results and suggests certain guidelines to be followed in data axquisition.

Chapter 6: The LDA Hardware

This chapter presents a cursory review of LDA theory and the hardware configuration of the equipment used in the measurements presented in this dissertation. The LDA theory presented here is by no means either complete or rigorous, for its purpose is only to provide enough information so that the reader can develop a physical feeling for the concepts introduced in the following two chapters. Readers interested in more background into LDA theory can consult such references as Durst, Melling and Whitelaw (1976), Greated and Durrani (1977), and Adrian (1980). The equipment description is presented to provide a foundation for the understanding of the fundamental sources of error arising from hardware design in LDA measurements.

Section 6.1: Fringe Model for Dual Beam Optical System

For the dual beam optical configuration of the DISA 55-X modular optics package, the operating principles of the burst processor, or counter, will be examined using the fringe model as first proposed by Rudd (1969). It must be noted that this model is not entirely correct and does not successfully predict the signal strength for particle sizes of the same order of magnitude as the fringe spacing*.

Reference Farmer (1972), Robinson and Chu (1975), Roberds (1977), and Adrian and Orloff (1977)

However, the model does satisfactorily explain the signal characteristics (frequency and burst time) output by available commercial counter packages. The physical principles underlying the fringe model are also much easier to conceptualize then the Doppler shift phenomena.

As shown in Figure 6.1.1, the intersecting laser beams interfere to form a set of fringes within the control volume where the two beams meet. The distance between the fringes can easily be determined from the intersection angle of the beams (Ω) and the wavelength of the laser line (λ).

$$\delta_f = \frac{\lambda}{2 \sin(\Omega/2)} \qquad (6.1.1)$$

The frequency at which a particle traverses the fringes is identical to the Doppler frequency (f_D). As a result, the Doppler frequency measured by the counter is directly proportional to the component of velocity perpendicular to the fringe pattern. The constant of proportionality (or calibration factor, C) is again only a function of the beam intersection angle and the wavelength of the laser. This feature makes the LDA system much easier to use than conventional hot wire systems.

$$f_D = \frac{U_x}{\delta_f} = 2U_x \frac{\sin(\Omega/2)}{\lambda} \qquad (6.1.2a)$$

$$U_x = C\, f_D \qquad C = \frac{\lambda}{2 \sin(\Omega/2)} \qquad (6.1.2b,c)$$

Consider a particle with a velocity vector perpendicular to the x-axis. Since the particle's path does not travel across the fringe pattern, a measurable Doppler

FIGURE 6.1.1

INTERSECTING LASER BEAMS AND FRINGE PATTERN

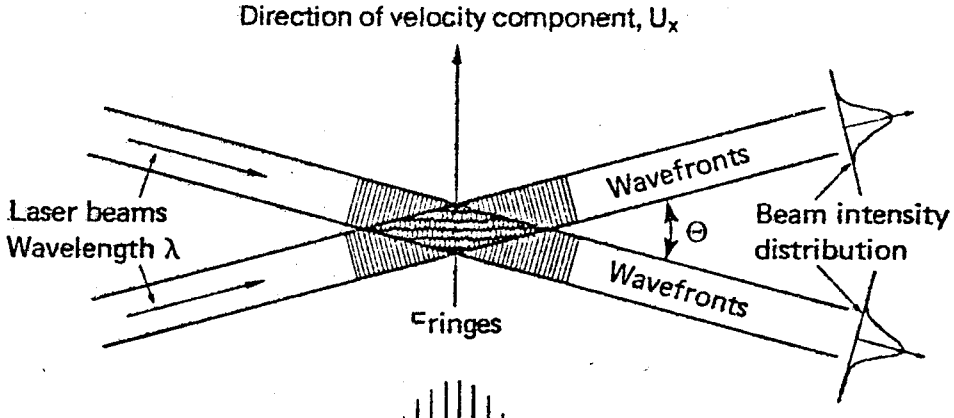

Fringe spacing $\delta_f = \dfrac{\lambda}{2 \sin \dfrac{\Theta}{2}}$

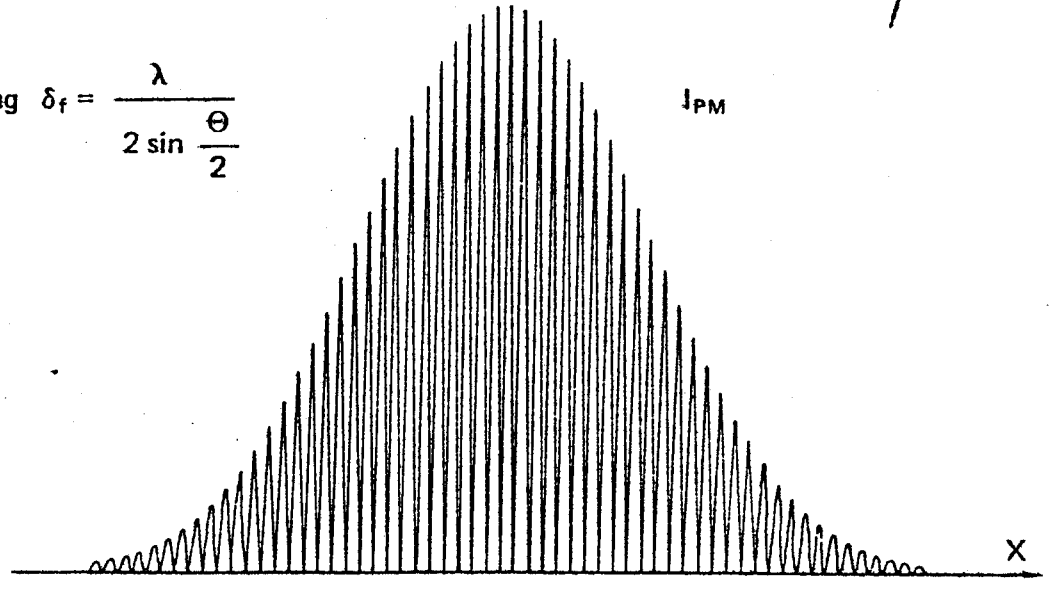

signal will not be produced. In addition there is no discernable difference in signal characteristics between velocity values equal in magnitude but opposite in direction. This situation can be remedied by the introduction of a frequency shift, f_s, into one of the incident laser beams, as depicted in Figure 6.1.2. Under these conditions the fringe spacing remains unchanged, but the fringes now have a constant velocity directed along the x-axis given by

$$U_s = \delta_f f_s \qquad (6.1.3)$$

The frequency processed by the counter is now related to the particle velocity relative to the fringe pattern

$$f_d = f_D + f_s = (U_x + U_s)/\delta_f \qquad (6.1.4)$$

Thus, the appropriate selection of frequency shift enables the accurate determination of velocity values even in cases of reverse flow. This important feature is lacking in most conventional hot-wire techniques. In addition, the presence of shift enables the conditioning of the Doppler signal to a frequency range in which the electronics of the counter can achieve optimum performance.

FIGURE 6.1.2

EFFECT OF FREQUENCY SHIFT ON FRINGE PATTERN

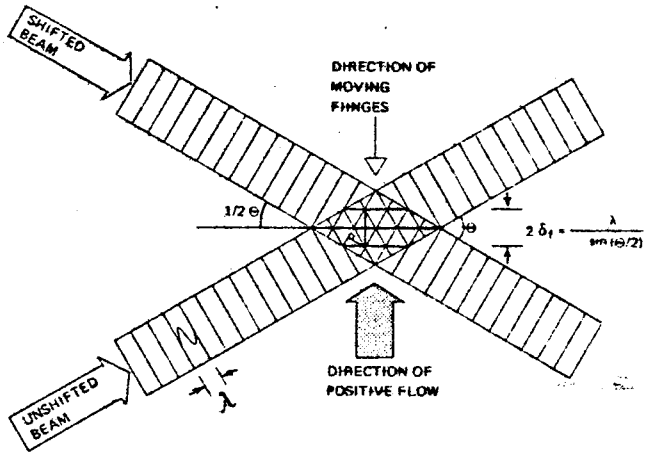

Fig. 51. Frequency shifting may be described as a movement of the fringes with the velocity $v_o = f_o \cdot \delta_f$

Section 6.2: Hardware Configuration of Burst Processor.

The DISA 55L90a counter may be viewed as a high speed digital 'stop watch'. The key to the stop watch is a 500 MHz clock. This clock emits a continuous train of logic pulses at a frequency of 500 MHz. To measure an interval of time, the pulses from the 500 MHz clock are counted and stored in a register. Since the number of ticks and the time period between ticks is known, the product of these two quantities is the desired time interval. The stop watch is capable of measuring two critical values: the time of flight for a particle to pass thru a preset number of fringes (this value is called the burst time and is denoted by P_8) and the sample time interval between successive particle arrivals, T. In addition, the 55L90a counter counts the number of fringes the particle encounters in passing through the measuring volume. For most of the measurements taken during this experiment, the output stored from the counter consisted only of the burst time for eight cycles and the total fringe count.

To identify the error inherent in the hardware design of the counter, it is necessary to gain a rudimentary understanding of how the stop watch works. The circuit diagram of the counter is presented in Figure 6.2.1. The first step is to transform the analog Doppler signal into a form which can be easily processed using digital electronic techniques. The shifted signal from the receiver optics is

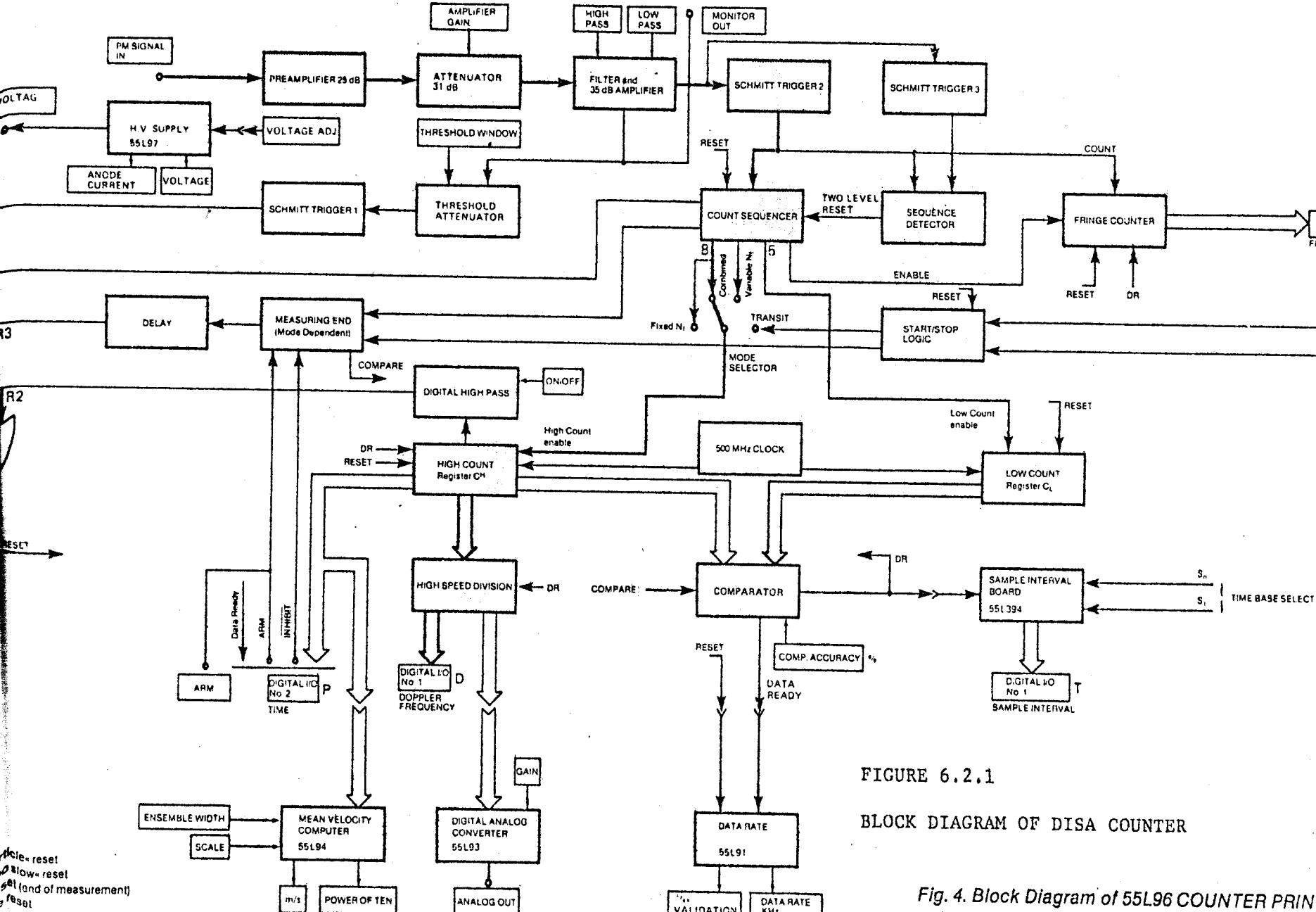

FIGURE 6.2.1

BLOCK DIAGRAM OF DISA COUNTER

Fig. 4. Block Diagram of 55L96 COUNTER PRIN

first amplified to the desired level, and then the high frequency noise and Doppler pedestel is removed using a band-pass filter. A typical Doppler signal is shown at the top of Figure 6.2.2. The filtered signal is shown immediately below. This filtered signal is then input to a Schmitt trigger. The output of the trigger is initially set at logical '0'. Whenever the input signal excedes 200 mV, the trigger output jumps to logical '1' and remains at that level as long as the filtered Doppler signal is positive. The result is a train of logic pulses, presented at the bottom of Figure 6.2.2. The period of the pulses is the time of flight to cross one fringe, so that the frequency of the pulses is that of the filtered Doppler signal.

These logic pulses are fed to the count sequencer. The pulses are used by the count sequencer to determine when the stop watches are to be turned on and off. To prevent the acceptance of realizations distorted by high noise levels, the DISA 55L90a counter was used in a mode which enabled two independent measurements of the Doppler frequency within the counter (this feature is the 5:8 validation scheme). The low and high count registers shown in the counter's schematic diagram are enabled for five and eight fringe crossings respectively. The count sequencer enables both registers to begin counting on the leading edge of the second pulse from Schmitt trigger-2. The count sequencer disables the low/high count register on the leading edge of

FIGURE 6.2.2

ELECTRONIC CONDITIONING OF DOPPLER SIGNAL

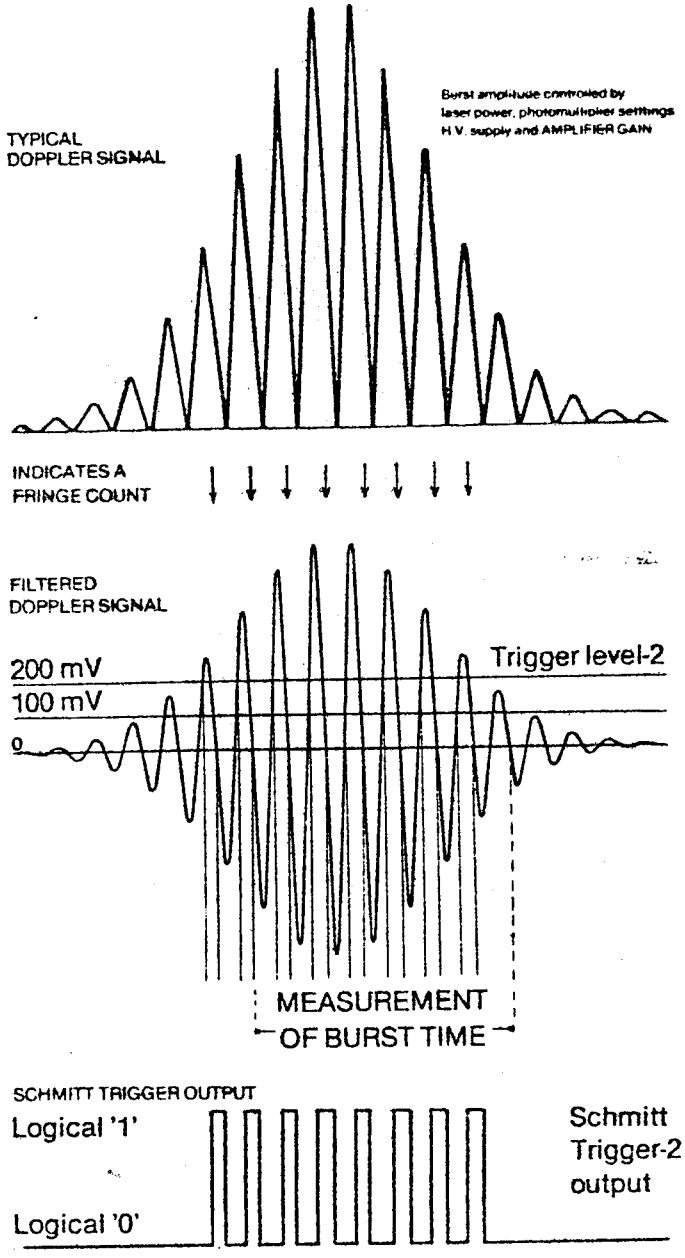

Fig. 8. Doppler signal from a signal scattering particle and the output from the Schmitt Triggers.

the seventh/tenth pulse. If the Doppler frequencies based upon the two registers do not agree to within a user selectable accuracy, the measurement is rejected and the 55L90a is reset. For all measurements presented in this thesis, the tolerance was +1.5%. The value for the time of flight from the high count register is recorded and output in digital form to the buffer as P_8, the burst time for eight cycles. The magnitude of the burst time is hardware limited to a discrete range between 64 nsec and 4.2 msec.

At the same time the count sequencer enables the low and high count registers, the fringe count register is also enabled. The fringe count register counts the number of logic pulses (i.e. fringe crossings) output from Schmitt trigger-2. A two level validation circuit (consisting of Schmitt trigger-3 and the sequence detector) detects the end of the burst and triggers a reset for the 55L90's hardware. At this point, the value of the fringe count register (N) is made available at the output. A data ready (DR) signal then indicates that the measurement is complete. The total number of cycles seen by the counter is N minus one.

Both burst time and fringe count are always positive quantities. The burst time is formatted as a real variable in normalized floating point format (i.e. the most significant bit, the MSB, is always one). The fringe count is provided in integer format. Thus, the information obtained from the counter is output in base two as follows

Burst Time for Eight Cycles

$$P_8 = P_m7P_m6 \ldots P_m0.P_m{-}1P_m{-}2 \quad 2^{P_x3P_x2P_x1P_x0} \qquad (6.2.1)$$

Total Number of Fringe Crossings

$$N = F7F6 \ldots F0 \qquad (6.2.2)$$

Section 6.3: Hardware Configuration of Buffer and Coincidence Filter

The validation rate is defined as the number of realizations per second accepted by the counter as reliable measurements. The data transfer rate to the computer may be up to six times this value for a two-color system (see Table 6.3.1). Since the counter must wait for a particle to pass through the intersecting beams to output a measurement, the validation rate is not constant, but fluctuates in a random fashion (see section 7.3). High spatial densities in particle seeding or high velocity values (which sweep the particles through the measuring volume at a higher rate) may cause two or more particles to arrive almost simultaneously. The data rate may temporarily achieve very high peaks. When measuring two or more components of velocity, data from the counters arrives at nearly the same moment in time, so the data rate becomes even greater. Because of these effects, certain experimental configurations can involve data rates high enough to prohibit the transfer of digital output from the counter to the computer.

The basic function of the buffer is thus to serve as

TABLE 6.3.1

VALIDATION RATE VERSUS DATA RATE

	DIGITAL OUTPUTS	VALIDATION RATE	DATA RATE
ONE COUNTER	N1,P1	f	2f
	N1,P1,T	f	4f
TWO COUNTERS	N1,P1,N2,P2	f	4f
	N1,P1,N2,P2,T	f	6f

For N = fringe count, P = burst time, T = sample interval

high speed temporary storage. While the buffer is storing the LDA data, the computer is free to perform other operations. In case of multi-channel measurements, the buffer is also capable of identifying the source of the data (i.e. from which counter the measurement originated).

For multi-channel measurements, the DISA 57G149 coincidence filter (see Figure 6.3.1) may also be installed with the buffer. The coincidence filter has two functions. The primary function of the module is to ensure the measurements consecutively stored within the buffer are from the same particle. Recall that at the end of a burst, the 55L90a's inform the buffer the data is available at the counter's output using the DR signal. Ideally, all the counters on line should provide the DR signal at the same instant in time. Unfortunately, the presence of multiple particles within the measuring volume disrupts the sequence of data collection. The coincidence filter acts as an intelligent gate, which will not permit the information to be passed on from counter to buffer unless all the counters emit a DR pulse within a user programmed period of time.

Besides guaranteeing that the realizations stored from all counters are synchronous in time, the coincidence filter also has it's own stop watch to measure the sample time interval, T, between accepted data realizations. The time base (i.e. period of time between the ticks of the master clock) for the floating point clock system is user

FIGURE 6.3.1

COINCIDENCE FILTER BOARD, BLOCK DIAGRAM

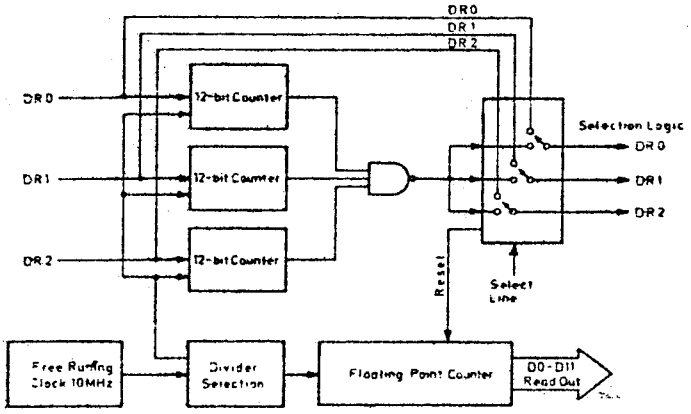

selectable. The sample time interval is available in digital format as a non-normalized floating point binary variable.

$$T = T_m 7 T_m 6 \ldots T_m 0 \; 2^{T_x 3 T_x 2 T_x 1 T_x 0} \qquad (6.3.1)$$

An additional benefit of the coincidence filter board is that it functions as an additional validation device. If one counter has for some reason produced a validated measurement from noise, the chances are negligible that the second counter has also validated a false signal. Therefore, the coincidence board also filters invalid realizations.

The selection of the coincidence window is crucial. When the window becomes too small, the data acquistion rate will begin to drop. Low velocity, long residence time realizations will be filtered out first. For the jet measurements of this investigation, the window was set between 10 to 50 microseconds, depending on the radial coordinate. To get a feel for this value, consider a detected frequency in the middle of the dynamic range (the low pass filters of the counters was consistently kept at 1 MHz during the investigation) of the counter at 500 kHz. For a coincidence window of 20 microseconds, the board would demand that both bursts end within 10 cycles of one another. Since the fringe count probability distribution functions (Figure 8.4.5) indicate that in most cases the fringe count rarely exceded 75, this would seem to be a reasonable

requirement. The measurements taken using a single channel LDA verified that the coincidence board was not filtering ont the low velocity realizations. It is emphasized that these measurements were taken in forward scatter with an excellent signal to noise ratio. In cases of increased noise levels, it will be necessary to widen the coincidence window.

Chapter 7: The Measurement of Flow Properties by the LDA

Section 7.1: Particle Effects on Measurements

A proper choice of particle seed is the most crucial decision facing the experimenter using an LDA system. Possible seeding sources may easily be found by consulting the available literature. Obviously, the most important criterion is that the Doppler signal produced must have adequate signal strength and a good signal-to-noise ratio.* The seeding particle must not only produce a clear signal, but must produce a velocity realization which is an accurate indicator of the immediate velocity of the fluid. Larger particles, with an inertia greater then a fluid element, will not be able to accelerate as quickly as the fluid. As a result, the larger particles will be insensitive to the high frequency oscillations of the turbulent flow field.

Consider the case where the particle concentration is low enough so that the flow field is not affected by their presence and each particle is alone in the turbulent field. The particle is considered to be spherical and smaller then the turbulence microscale, so that its behavior is as though it was immersed in a uniform velocity field. When the ambient velocity field changes, the acceleration of the

---

* A number of models have been suggested to determine signal quality given the optical characteristics of the measurements system and the particle parameters. Reference Adrian (1979), Brockmann (1979), Agarawal and Keady (1980).

particle is driven by the Stokes drag force acting due to the velocity difference between the particle and the surrounding fluid.

$$\frac{\pi}{6} d_p^3 \rho_p \frac{dU_p}{dt} = 3\pi\mu\rho_f d_p (U_f - U_p)$$

$$\alpha \frac{dU_p}{dt} = U_f - U_p$$

where $$\alpha = (d_p \rho_f)^2 / (18\mu\rho_p) \qquad (7.1.1)$$

The relationship between the particle and fluid velocities may thus be approximated as a linear, first order system with time constant α. The results can be more clearly examined using the frequency response function, $H(\omega)$, to relate the spectrum of the two velocities.

$$S_p(\omega) = |H(\omega)|^2 S_f(\omega)$$

$$= \frac{1}{1 + (\alpha\omega)^2} S_f(\omega) \qquad (7.1.2)$$

The frequency response function is a simple low pass filter. This is the expected result, confirming that for certain higher frequencies, the particle will be unable to respond to fluctuations in the ambient flow field. To ensure the particle velocity is equivalent to the fluid velocity, the following criterion is established

$$\alpha\omega_c < 0.1 \qquad (7.1.3)$$

where ω_c is the lowest frequency at which attenuation is acceptable.

For turbulent flows, the Lagrangian velocity provides the appropriate frequency value to substitute into the above

equation. Using the Kolmogorov microscales of length and velocity (expressed in terms of the kinematic viscosity ,μ/ρ, and the dissipation rate ,ε) the cut-off frequency needed to measure the smallest flow scales may be estimated:

$$\eta_K = ((\mu/\rho)^3\varepsilon)^{1/4} \qquad \text{length scale}$$

$$v_K = (\varepsilon(\mu/\rho))^{1/4} \qquad \text{velocity scale}$$

$$\omega_K = 0.74\ v_K/\eta_K \qquad \text{frequency cut-off}$$

$$= 0.74(\varepsilon(\rho/\mu))^{1/2}$$

(7.1.4)

From the data of Champagne (1978), the dissipation at the jet centerline is approximated as

$$\varepsilon = (0.38)\ U_m^3/x \qquad (7.1.5)$$

for $U_m = 5.8\ U_o D/x$

Since the centerline velocity is inversely proportional to x, both the dissipation rate and the cut-off frequency decay with x ($1/x^4$ and $1/x^2$ respectively). The Kolmogorov length scale increases linearly with x. Table 7.1.1 lists the dissipation rate, length scale, and cut-off frequencies calculated using the above formulas at three centerline positions.

For experiments in which only the rms velocities are of interest, the cut-off frequency may be relaxed and fixed at a higher value within the inertial subrange, e.g.

$$\omega_I = 20\ u/l \qquad (7.1.6)$$

The estimate of this quantity may be made by using the centerline turbulence intensity as the appropriate velocity

TABLE 7.1.1

PARTICLE SIZE CUT-OFF FREQUENCIES

Cut-off Frequency Based on Kolmogorov Microscales

x/D	U_m m/s	ε m^2/s	η mm	ω_K hz
75	4.6	20.	.11	140
95	3.4	6.0	.15	74
120	2.7	2.3	.18	47

Cut-off Frequency Based on Inertial Subrange

x/D	U_m m/s	u m/s	l m	ω_I hz
75	4.6	1.3	0.10	40
95	3.4	0.95	0.14	22
120	2.7	0.76	0.18	14

x/D axial position (D = 1 inch)
U_m centerline mean velocity
ε dissipation rate
η_K Kolmogorov length scale
u turbulent velocity at centerline
l large eddy length scale

scale (i.e. $u = 0.28\ U_m$). Since the dissipation ,ε, is equal to u^3/l, equations (7.1.5) may be used to show the proper choice for the length scale is $l = (0.058)x$. The results of these calculations are also listed in Table 7.1.1.

The diameter of the glycerin smoke particles has been estimated by Nee (1983) to be between 0.1 to 1.0 microns. The particle size is clearly much smaller then the expected range of Kolmogorov microscales (see Table 7.1.1). However, since the mean free path in air is approximately 0.1 micron, the applicability of the continuum hypothesis underlying Stoke's Law is questionable for the range of smaller particle sizes. The response time of the particle may still be roughly estimated using the equations presented above. The density ratio between the glycerin particles and air is roughly a thousand to one. Using these values, the time constant and cut-off frequency are evaluated.

$$\tau_c = 0.37 \times 10^{-5} \text{ sec}$$

$$\omega_c = 2.7 \times 10^4 \text{ rad/sec} \quad \text{or} \quad f_c = 4.3 \text{ khz} \qquad (7.1.7)$$

The cut-off frequency is clearly above the highest Lagrangian frequency predicted. The particles have a fast enough response time so that the difference between fluid and particle velocity is negligible even for the smallest turbulence length and time scales. It may be concluded that glycerin smoke may be used with confidence in the axisymmetric jet to provide accurate flow measurements.

TABLE 7.2.1

PHYSICAL PROPERTIES OF OPTICAL GEOMETRY

f	Lens Focal Length	1200 mm
D_2	Beam Separation	53 mm
Ω	Intersection Angle	2.60 deg
S	Sensitivity	.09 MHz/m/s
	Counter Bandwidth	64 kHz to 1MHz 9 meter/sec
d_f	Beam Waist Diameter	0.32 mm
2c	Probe Volume Length	14.3 mm

TABLE 7.2.2

CALIBRATION PROPERTIES OF OPTICAL GEOMETRY

Ω	Intersection Angle	2.60 deg
λ_B	Wavelength (BLUE line)	488 nm
δ_{fB}	Fringe Spacing	10.8 m
N_{fB}	Fringes in Optical Probe Volume	28
C_B	Calibration Factor	10.8 m/s/MHz
λ_G	Wavelength (GREEN line)	514 nm
δ_{fG}	Fringe Spacing	11.3 m
N_{fG}	Fringes in Optical Probe Volume	28
C_G	Calibration Factor	11.3 m/s/MHz

Section 7.2: Selection of Optical Package

The critical parameter of the transmitting optics is the selection of the beam intersection angle. The probe volume, the volume within the $1/e^2$ boundary of the optical fringe modulation, is depicted in Figure 7.2.1. The vertices of the ellipsoidal probe volume are a function of the beam intersection angle , Ω, and the beam waist of the focused laser beam, d_f,

$$2a = \frac{d_f}{\cos(\Omega/2)} \quad , \quad 2b = d_f \quad , \quad 2c = \frac{d_f}{\sin(\Omega/2)} \qquad (7.2.1)$$

Since the beam intersection angle is commonly less then 45 degrees for most configurations, the dimension largest in magnitude is c, the length along the optic axis (z-axis in the figure). Obviously, the probe volume is minimized and the spatial resolution maximized by choosing an intersection angle as large as possible.

Recall from chapter seven that the calibration constant relating the Doppler frequency to the velocity is also a function of the beam intersection angle. Even if frequency shift is present, the inverse of the calibration constant can also be viewed as a sensitivity factor relating the change in Doppler frequency per unit change in velocity. Equation 7.2.2 demonstrates that this sensitivity factor increases with the beam intersection angle and is inversely proportional to the wavelength of the laser line.

FIGURE 7.2.1

OPTICAL PROBE VOLUME

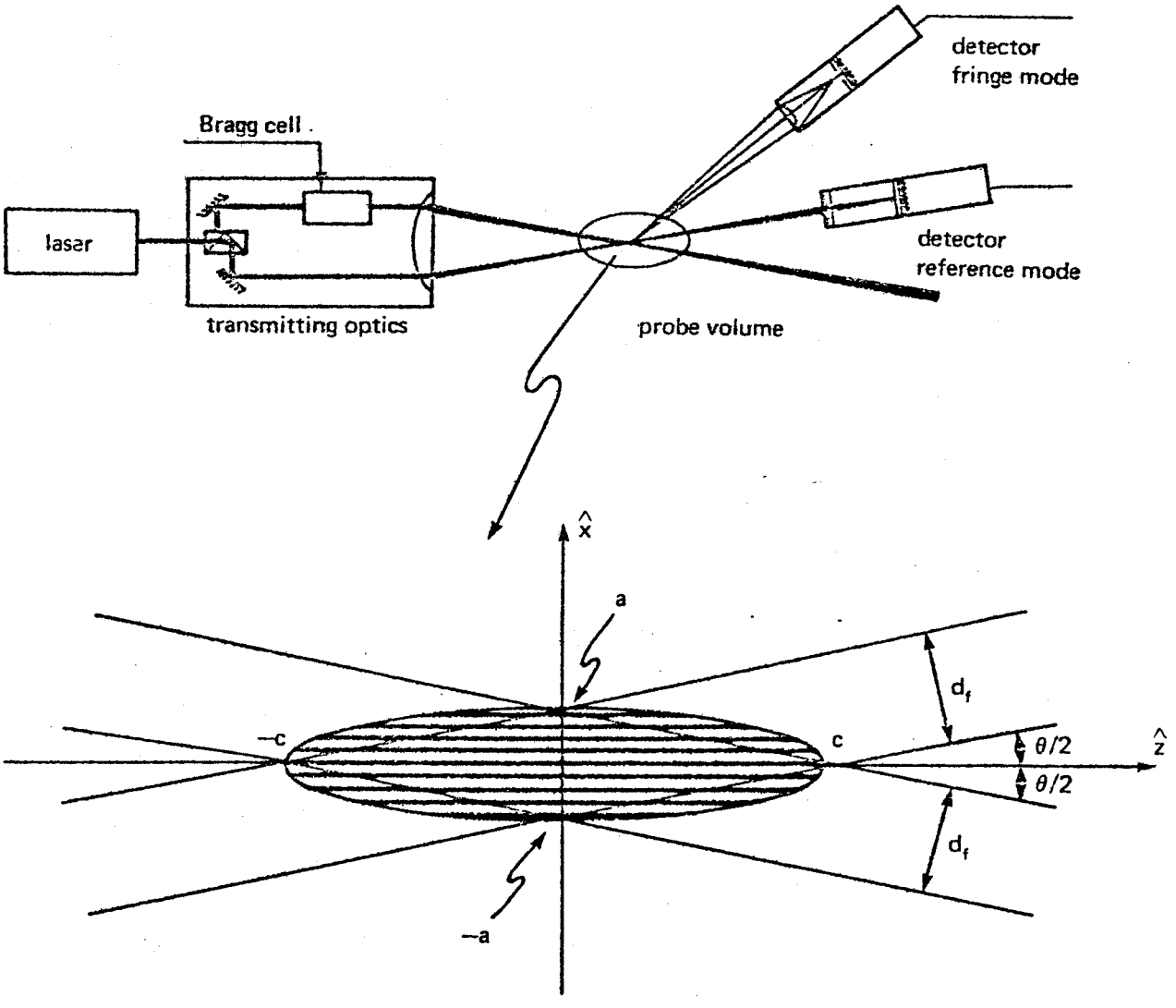

$$\Delta f_D = \Delta U_x / C = S \, \Delta U_x$$
$$S = \frac{2 \sin(\Omega/2)}{\lambda} \qquad (7.2.2)$$

Thus, to increase the sensitivity of the LDA measurement system to changes in velocity and to maximize spatial resolution, the beam intersection angle should be as large as possible. This intersection angle is determined by the focal length of the front lens (standard sizes range from 80 to 1200 mm. for the DISA 55-X optics system) and the beam separation diameter (this value could be varied from 18 to 55mm.). For a commercial optical package, the upper limit for the magnitude of the beam separation is fixed. The user may modify the beam intersection angle through the appropriate selection of the front lens.

Two other factors may also influence the selection of the beam intersection angle. In chapter seven, it was shown that the Doppler signal must be band-pass filtered to reduce noise. Thus, once the filters in the counter hardware have been set, the sensitivity factor must be such that the range of velocities lies within the filter band. Unfortunately, the predominate factor in the determination of the lens focal length (and therefore the beam intersection angle) is the physical geometry of the flow field and measurement system. For the axisymmetric jet the primary problem is ensuring that the system is sufficiently far removed from the flow so as not to interfere with it. For a value of

x/D=100, or x=100 inches, the radial coordinate at the edge of the field is n= 0.20 or y=20 inches. As a result, even a focal length of 600 mm. on the front lens would place the optical bench and laser in a position where it might affect the entrainment flow field. Because of this, a 1200 mm. lens was used for all measurement points. Table 7.2.1 lists the optical parameters used in this experiment. Those parameters dependent upon wavelength are presented in Table 7.2.2.

Section 7.3: Statistical Dependence of Flow Field and Particle Arrival Rates - The Problem of Bias

Consider a seeding distribution which is controlled so that only one particle is within the measuring volume at any instant in time. This constraint requires a low particle seed rate, so that rather than having a continuous flow of data available, the information comes as a series of discrete points. Figure 7.3.1 depicts such a situation. Even for incompressible flow where the particle seeding is distributed statistically uniformly, the sampling process is, in general, not independent of the process being sampled (i.e. the velocity field). Measurements have shown (see McLaughlin and Tiederman (1973) and Erdmann and Gellert (1976) that the arrival rate and the flow field are strongly correlated. During instances of higher velocity, a larger volume of fluid is swept through the measuring volume, and a greater number of discrete data points will be recorded. As a direct result, an attempt to evaluate the statistics of

FIGURE 7.3.1

VELOCITY SIGNAL FOR BURST TYPE LDA

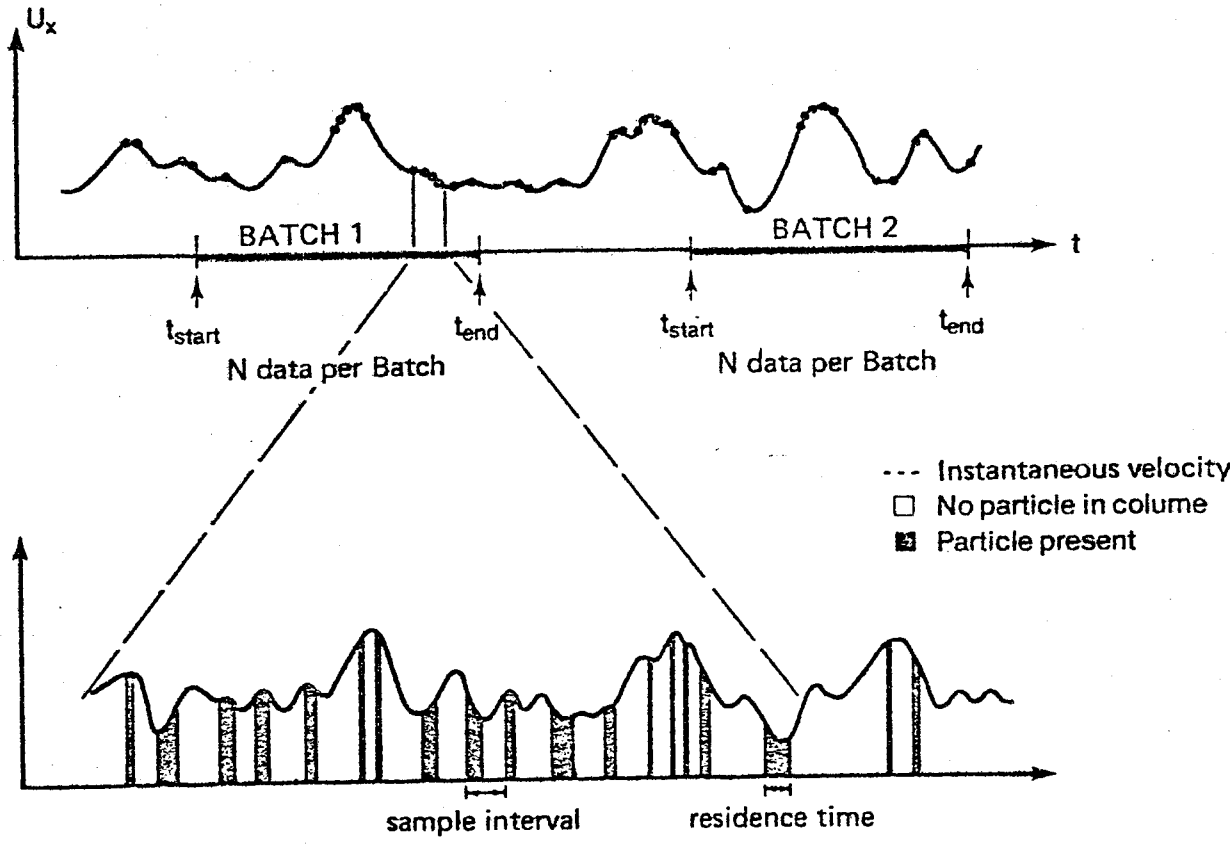

g. 5.

g. 6.

g. 5. Random sampling by burst-type LDA (55L90a LDA COUNTER PROCESSOR).

g. 6. Illustration of typical velocity signal as sampled by individual and randomly arriving particles (see ref. 45).

the flow field using arithmetic averaging will bias the results in favor of the higher velocities.

The correct method of performing the statistical averages on individual realizations was presented by George in 1975 (v. George 1976). This method will be briefly outlined and the major conclusions summarized here. Additional information can be found in George (1978), Buchhave, George, and Lumley (1979) and Buchhave (1979). By initially formulating the averaging process in terms of the Lagrangian flow field, it is possible to remove the statistical dependence between the flow field and the particle arrival rates. The sampled velocity is represented as

$$U_o(t) = \iiint U_L(\underline{a},t)\, g_L(\underline{a})\, w_L(\underline{x}(\underline{a},t))\, da^3 \quad (7.3.1)$$

$U_L(\underline{a},t)$ is the velocity of the fluid at time t with initial position $\underline{a}$ at t=0. The function g_L is a random distribution in space of Dirac functions which accounts for the presence or absence of a particle at position $\underline{a}$ at t=0. Thus, this function selects those points in space where a particle is initially located. The function $w_L(\underline{x})$ turns the signal on (i.e. $w_L(\underline{x})$ equals one) during the interval of time in which the particle passes through the measuring volume and is zero for all other instances in time. When integrating over all space, the product term of these two functions turns the velocity history of the particle, $U_L(\underline{a},t)$, on only when that particle is in the measuring

volume.

It is possible to apply a transformation from a Lagrangian to an Eulerian mapping. A simple example of this type of transformation is explained in Figure 7.3.2. The result is

$$U_o(t) = \iiint U(\underline{x},t)\, g(\underline{x},t)\, w(\underline{x})\, d\underline{x}^3 \qquad (7.3.2)$$

The Lagrangian velocity $U_L(\underline{a},t)$ is mapped to the Eulerian velocity field $U(\underline{x},t)$. The Eulerian distribution function now determines the locations of the particles at a given instant in time. If the distribution function is integrated over an arbitrary volume, V, the result is the number of particles within that volume, n_p.

$$n_p(t) = \iiint_V g(\underline{x},t)\, d\underline{x}^3 \qquad (7.3.3)$$

The ensemble average of the number of particles within that volume is then

$$\overline{n_p} = \iiint_V \overline{g(\underline{x},t)}\, d\underline{x}^3 = \overline{g(\underline{x},t)}\, V \qquad (7.3.4)$$

If the seeding is distributed uniformly in space and is steady with respect to time, then the ensemble average of the distribution function is a constant value (say $\overline{g(x,t)} = \mu_c$). In addition this constant value is simply the particle concentration - the number of particles per unit volume,

$$\overline{g(\underline{x},t)} = \mu_c = \overline{n_p}/V \qquad (7.3.5)$$

The function $w(\underline{x})$ in equation (7.3.2) now turns the

signal on only in the region of space defined by the measuring volume. The function $w(\underline{x})$ defining the measuring volume is a deterministic function equal to one for $\underline{x}$ within the measuring volume, zero elsewhere. The product of $g(\underline{x},t)$ and $w(\underline{x})$ is again non-zero only when a particle is in the control volume. At this point, the analysis is limited to those cases in which only one particle is present within the measuring volume for any instant in time. The function 'turning on' the velocity field is

$$\iiint g(\underline{x},t)\, w(\underline{x})\, d\underline{x}^3 \qquad (7.3.6)$$

Taking its ensemble average yields

$$\iiint \overline{g(\underline{x},t)}\, w(\underline{x})\, d\underline{x}^3 \qquad (7.3.7)$$

This term is one whenever a particle is in the control volume and zero otherwise, so that its average is the fraction of time the signal is non-zero. This quantity is then the sum of the residence times, P_i, over all i realizations divided by the total averaging or sample time, T_s, i.e.

$$\iiint \overline{g(\underline{x},t)}\, w(\underline{x})\, d\underline{x}^3 = \frac{1}{T_s} \sum P_i \qquad (7.3.8)$$

Consider the left hand side. Since the ensemble average of the particle distribution function is constant, $\overline{g(x,t)}$ is taken outside of the integral sign. Since $w(\underline{x})$ is nonzero only within the measuring volume

V_{mv}, the right hand side reduces to

$$\iiint \overline{g(\underline{x},t)}\ w(\underline{x})\ d\underline{x}^3 = \mu_c V_{mv} \qquad (7.3.9)$$

The above two expressions are then solved to determine the particle concentration

$$\mu_c = \frac{1}{T_s}\frac{1}{V_{mv}} \sum P_i \qquad (7.3.10)$$

This equation states that the fraction of time a signal is seen by the counter is exactly the average number of particles in the measuring volume. Further applications of this result are discussed in chapter nine.

Return to equation (7.3.2). Recall that this equation relates the outpnt of the counter to the Eulerian flow field and the instantaneous particle distribution, and that these functions are statistically independent of one another (as seen by their initial formulation in the Lagrangian field). An ensemble average of this quantity is easily performed.

$$\overline{U_o(t)} = \iiint \overline{U(\underline{x},t)}\ \overline{g(\underline{x},t)}\ w(\underline{x})\ d\underline{x}^3 \qquad (7.3.11)$$

Consider the left hand side. The time average of the sampled velocity is the shaded area shown in Figure 7.3.1 divided by the total time interval over which the data is sampled. If U_i is defined as the ith realization of the velocity, the left hand side can be expressed as

$$\overline{U_o(t)} = \frac{1}{T_s}\int_0^{T_s} U_o(t)\ dt = \frac{\sum U_i\ P_i}{T_s} \qquad (7.3.12)$$

The right hand side is now simplified. First, since

the averaged Eulerian velocity is constant, it can be removed outside of the integral sign. The integral term is rearranged using equations (7.3.9) and (7.3.10) to the following form

$$\iiint \overline{U(\underline{x},t)}\ \overline{g(\underline{x},t)}\ w(\underline{x})\ d\underline{x}^3 = \overline{U(\underline{x},t)}\ \mu_c\ V_{mv} \qquad (7.3.13)$$

$$= \frac{\overline{U(\underline{x},t)}}{T_s} \sum P_i$$

Equations (7.3.12) and (7.3.13) are substituted back into equation (7.3.11). The result expresses the Eulerian mean velocity as a function of the instantaneous velocities and residence times.

$$\overline{U(\underline{x},t)} = \frac{\sum U_i\ P_i}{\sum P_i} \qquad (7.3.14)$$

Thus, to measure the correct mean velocity, the velocity points must be weighted with respect to the residence time of the particle within the measuring volume. A similar procedure must be followed for the higher moments. For example

$$\overline{u_i^2} = \frac{\sum U_i^2\ P_i}{\sum P_i} \qquad (7.3.15)$$

Expressions can also be developed for the variance of these time averages as a function of the integral scale, τ_u, the time interval over which the data is taken, τ_s, and the mean data rate, γ_r. Thus, if we define the velocity covariance and the time integral scale of the turbulence as

$$B(\tau) = \overline{u(t)u(t+\tau)}$$

$$\tau_u = \frac{1}{\overline{u^2}} \int_0^\infty B(\tau)\, d\tau \qquad (7.3.16a)$$

then it can be shown (George 1978) that

$$\text{var}[\bar{U}] = \overline{u^2} \left[\frac{2\tau_u}{T_s} + \frac{1}{\gamma_r T_s} \right] \qquad (7.3.16b)$$

$$\text{var}[\overline{u^2}] = (\overline{u^4}) \left[\frac{2\tau_u}{T_s} + \frac{1}{\gamma_r T_s} \right] \qquad (7.3.16c)$$

Note that for a high data rate, the variance is essentially that of a continuous time function - it is dominated by the term $2\tau_u/T_s$, the ratio of the integral scale to the total averaging time. For low data rates, all data points become statistically independent and the variance is determined by $1/\gamma_r T_s$, the number of independent samples.

The above theory has assumed that during the time interval over which the data is taken, all realizations are stored and utilized in the residence time computation of the velocity values. In actual practice in fluid media with high particle concentration values, this will result in a large number of data points. A large high speed memory or a computer fast enough to perform real-time manipulation of the incoming data will then be required. For experimental situations, Buchhave (1979) has recommended repeatedly taking small batches of data to avoid large data storage requirements. Residence time weighting techniques are used to compute velocity values for each batch, and the results

of all the batches are averaged arithmetically. The interval between successive batches should be separated by at least two integral scales to insure that each batch is statistically independent. If σ_B^2 is the variance of the value from one batch (obtained using equations 7.3.14 and 7.3.15), the final variance of the value computed by averaging the N_B batch values is given by

$$Var[X] = \frac{\sigma_B^2}{N_B} \qquad (7.3.17)$$

There is further discussion of this in Section 8.1.

Section 7.4: Bias Due to Dropout and Correction with Frequency Shift

There is an additional source of contamination of LDA counter measurements. The counter hardware described in chapter seven requires a minimum number of fringe crossings (eight for the DISA counter) to validate and record a burst. Any particles moving parallel to the fringes will be ignored and the counter is insensitive to velocity vectors in this 'dead zone'. The dropout of validated signal in this region causes an angular bias because specific values of the velocity vector will not be recognized by the LDA hardware. However, if the particle trajectory does not cross a sufficient number of fringes, a velocity may be imposed upon the fringes (with the use of the frequency shift unit) so that the fringes cross the particle path the required minimum number of times.

How much frequency shift is enough? Buchhave's analysis (1976) provides a quantitative formulation to estimate the required frequency shift. The ellipsoidal optical probe volume (with half axes a, b, and c) is again defined as the $1/e^2$ boundary of the optical fringe boundary. Define N_e as the minimum number of fringe crossings required by the counter hardware and N_f as the number of fringes in the volume at any instant in time. The ratio of these two numbers is defined as $Q_N = N_e/N_f$. The total number of fringes is a function of the beam separation, D_2, and the beam waist diameter before the focusing lens, d_2. The number of fringes required for a validated measurement is determined by the counter hardware and set at a constant value of eight, i.e.

$$N_f = \frac{4D_2}{\pi d_2} \qquad Q_N = \frac{2\pi d_2}{D_2} \qquad (7.4.1)$$

Consider the plane containing the ellipsoid's center and normal to the velocity vector. The area of the plane enclosed by the ellipse (i.e. the projection of the optical probe volume onto the normal plane) is the optical probe cross-section, S_p, for the given velocity vector. For example, if the velocity is directed along the x-axis, its value is πbc. When the velocity is parallel to the z-axis, the optical probe cross-section is πab. The value of S_p for an arbitrary velocity vector is

$$S_p(\underline{U}) = \pi abc\ R \qquad (7.4.2)$$

where $$R = \frac{1}{|\underline{U}|}\left[\left[\frac{U}{a}\right]^2 + \left[\frac{V}{b}\right]^2 + \left[\frac{W}{c}\right]^2\right]^{1/2}$$

The measuring volume cross section, S_m, is the area normal to the instantaneous velocity within which a set of parallel particle trajectories will produce a validated measurement. As a result, it is not only a function of the velocity vector, but is dependent upon the optical and electronic hardware as well. The relative cross section, σ_s, is the ratio of optical probe cross-section to the measuring volume cross section. This quantity is always less than or equal to one. Since the probe volume should be identical to the measuring volume to avoid directional bias, the relative cross section should be constant and equal to one regardless of the particle trajectory. Buchhave derived a relation for S_m as a function of Q_N, the velocity vector $\underline{U}$, and the velocity of the moving fringes, U_s. For convenience, $Q_s = |\underline{U}|/U_s$ is defined as the frequency shift factor.

$$\sigma_s = S_m/S_p = 1 - a^2 Q_N^2 R \frac{|\underline{U}|^2}{(U - U_s)^2} \qquad (7.4.3)$$

where as before

$$R = \frac{1}{|\underline{U}|}\left[\left[\frac{U}{a}\right]^2 + \left[\frac{V}{b}\right]^2 + \left[\frac{W}{c}\right]^2\right]^{1/2}$$

For a two-dimensional velocity field, this function is plotted in polar coordinates in Figure 7.4.1. Figure 7.4.1a provides a simple example to interpret the plot. The radial coordinate is the relative cross section, . The circle is

FIGURE 7.4.1

ANGULAR BIAS

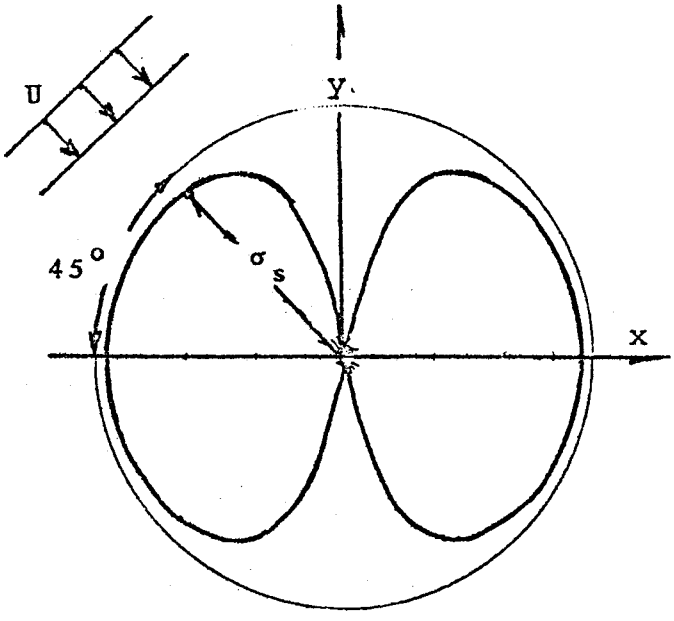

Fig. a, $U_s = 0$

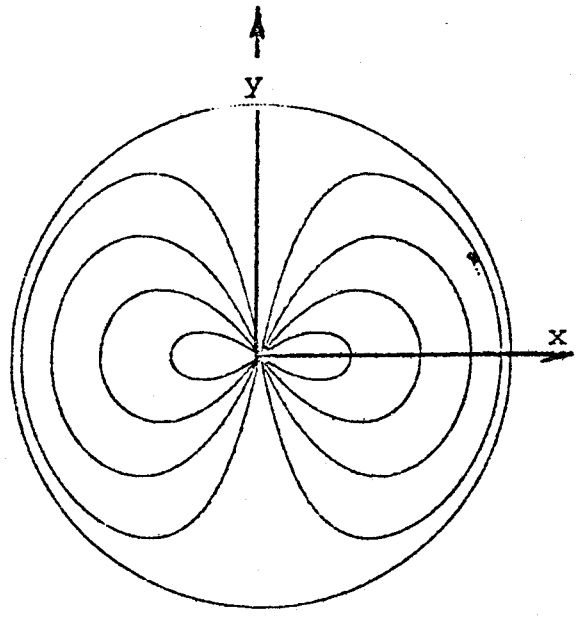

Fig. b, $U_s = 0$

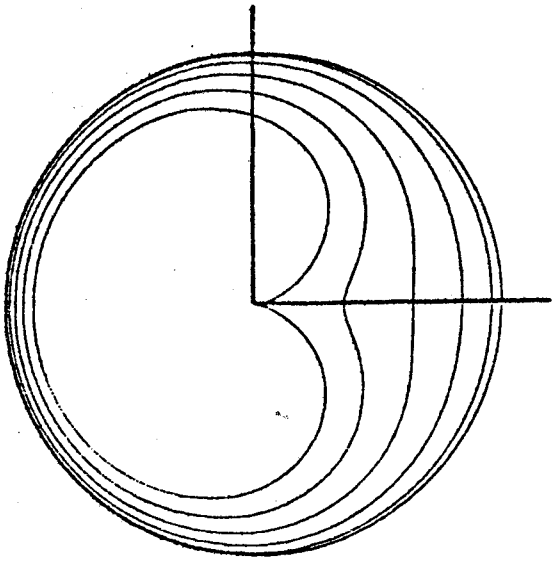

Fig. c, $U_s = 2U$

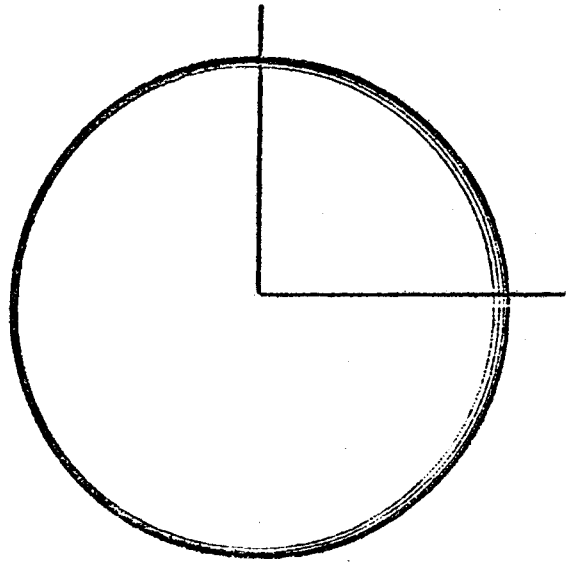

Fig. d, $U_s = 5U$

the locus of points for which the probe volume is identical to the measuring volume (i.e. $\sigma_s = 1$). The curve within the circle is a plot of the relative cross section for a case without frequency shift and $Q_N = 0.2$. The angular coordinate identifies the orientation of the velocity vector (i.e. $\xi = \arctan(U/V)$). As a specific example, suppose the relative cross section is wanted for a velocity vector where the horizontal velocity component is equal to the vertical component. In this case ξ equals forty-five degrees, and the relative cross section is $\sigma_s = 0.98$. There is also a distinct range of angles for wich the measuring cross section is zero. This region corresponds to the dead zone of the counter.

Figure 7.4.1b plots the same situation for different values of Q_N. Increasing values of Q_N increase the dead zone region and decrease the measuring cross section. Obviously, the optical parameters should be set to minimize Q_N by maximizing N_f, the total number of fringes in the measuring volume. Since Q_N is proportional to the beam separation, the beam separation should be as large as possible.

Of course, the other alternative is to increase the frequency shift. Figure 7.4.1c demonstrates the effect on the measuring volume when the frequency shift is twice the expected velocity. Angular bias effects become significant for Q_N greater than 0.2. If the frequency shift is five

times the expected velocity magnitude, as in 7.4.1d, the bias becomes negligible. It must be noted that this last operating condition is overly stringent. In a flow field such as the jet, it is reasonable to expect that the magnitude of the velocity is roughly correlated with direction. A high velocity is more likely to be pointed downstream than upstream. Q_U is dependent on direction. The tendency for the relative cross-section to decrease as the angle increases is offset by the decrease in Q_U. Still, to be safe, it is tempting to avoid angular bias by using a large value for the frequency shift.

Unfortunately, large values of frequency shift, f_s, are undesirable for a number of reasons. First, higher shift values require the counter to process higher frequency signals. Experience in the laboratory has proven that the better quality Doppler signals are those at low frequency. Second, to measure the Doppler frequency due only to the velocity of the particle, f_D, the frequency shift must be subtracted from the frequency of the signal detected by the counter f_d, i.e.

$$f_D = f_d - f_s \qquad (7.4.4)$$

If the shift is large compared to the Doppler frequency, the Doppler frequency is the small difference between two large numbers. This can induce significant error. To maximize resolution of the Doppler frequency, the detected signal and the Doppler frequency should be of the

same order of magnitude.

The final reason is the accuracy of the digital clock. Recall that to measure the Doppler frequency, the counter counts the number of clock ticks for eight cycles of the burst. The precision of the measurement is directly proportional to the length of time over which the measurement is taken or inversely proportional to the frequency of the burst. Thus, due to the design of the counter hardware (see section 8.5) the burst time has a better resolution for lower frequencies.

It may be concluded that to maximize the precision of the counter measurements, the frequency shift should be no greater than the minimum amount required to avoid angular bias. Note that when dealing with highly turbulent flows, it may be necessary to increase the frequency shift so that the mean of the detected frequency is centered in the counter's bandwidth.

Section 7.5: Hardware Accuracy of Burst Time and Doppler Frequency

The frequency information, f_d, detected by the counter is computed using the total time period for eight cycles. This quantity has already been identified as the burst time, P_8. During this time period, the pulses from the 500 MHz clock (two nanoseconds period) are counted and stored in the high count register. The high count register is a 21 bit binary counter. Suppose the frequency of the detected signal is 500 kHz. The total time for eight

periods of this signal is two microseconds so that the high count register counts 2000 pulses.

As seen in Figure 7.5.1, the largest possible error will be a timing error of plus or minus one clock pulse, t_c. Define e_{Pc} as the absolute error for the measured time period of eight cycles.

$$e_{Pc} = P_8(\text{actual}) - P_8(\text{measured}) \qquad (7.5.1)$$

The probability function for this error term is depicted at the bottom of Figure 7.5.1. It is a top hat function since all values are equally probable. This behavior is analogous to the quantization error of an ideal A/D converter. The mean value and standard deviation of the error are easily calculated.

$$E\langle e_{Pc}\rangle = 0 \qquad S\langle e_{Pc}\rangle = t_c^2/3 = 1/3f_c^2 \qquad (7.5.2)$$

The relative error for the burst time estimate, ε_{Pc}, is calculated using the standard deviation of the probability function.

$$\varepsilon_{Pc} = \frac{S\langle e_{Pc}\rangle}{P_8} \times 100\% = 7.2\ (f_d/f_c) \qquad (7.5.3)$$

The relative error of the burst time is directly proportional to the frequency of the detected signal and inversely proportional to the frequency of the clock. This is as expected. The lower the detected frequency, the longer is the elapsed time period for eight cycles of the Doppler burst. The longer the time period, the higher is the number of ticks counted by the digital clock and the

FIGURE 7.5.1

DIGITAL CLOCK MEASUREMENT ERROR

Clock Measurement Short One Period

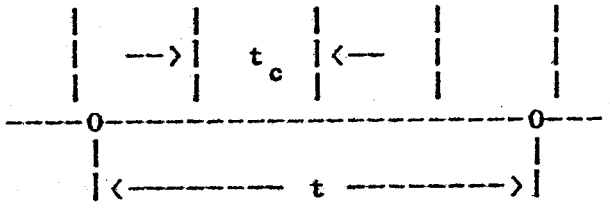

Elapsed time = 4 t_c

Measured time = 3 t_c

Clock error = $-t_c$

Clock Measures One Additional Period

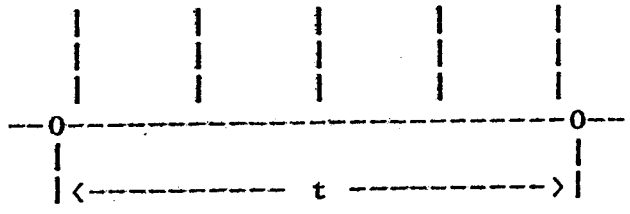

Elapsed time = 2 t_c

Measured time = 3 t_c

Clock error = t_c

Clock Error Probability Density Function

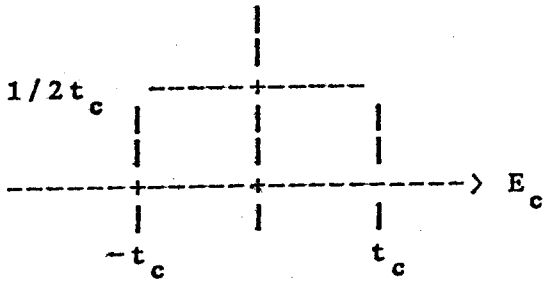

Mean Value $\bar{E}_c = 0$

Variance $\overline{e_c^2} = t_c^2/3$

greater is the relative accuracy. Since the counter's clock has a fixed value, the only varying parameter affecting the relative error is the detected frequency. For the measurements recorded in this dissertation, the largest value is less then 0.02%. Thus, the contribution of the clock towards any measurement error seems negligible.

The relative error of the Doppler frequency, f_D, is also of primary importance. Recall that the detected frequency is obtained directly from the burst time. The Doppler frequency is obtained by subtracting the frequency shift, f_s, from the detected frequency, i.e.

$$f_D = f_d - f_s \qquad (7.5.4)$$

Inaccurracies in the measurements are suspected if the frequency shift is large compared to the Doppler frequency. It is relatively easy using the above equations to obtain an exact relation for the size of this error. To begin, note that the value for the relative error of the burst time is also equivalent to the relative error of the detected frequency. Thus, the relative error of frequency of the detected signal, ε_{dc}, can easily be determined as follows

$$\varepsilon_{Pc} = \varepsilon_{dc} = \Delta f / f_d \text{ X } 100\% \qquad (7.5.5)$$

To find the error relative to the Doppler frequency, ε_{Dc}, multiply equation (7.5.3) by the detected frequency, then divide by the Doppler frequency. The detected frequency is then expressed as the sum of the Doppler frequency and frequency shift to yield the final result,

$$\varepsilon_{Dc} = \Delta f/f_D \times 100\% = 7.2\ (f_D/f_c)(1 + f_s/f_D)^2 \qquad (7.5.6)$$

The relative error for the Doppler frequency varies inversely with the clock frequency, but also is a function of the frequency shift. The above limits illustrate two essential behavior patterns. When either the frequency shift is much less than the Doppler frequency or the frequency shift is zero, the detected and Doppler frequencies are equivalent. The relative error for both the detected and Doppler frequencies are the same. The more interesting behavior occurs in the second limit, when the frequency shift is much greater than the Doppler frequency. In practical applications, such instances are more likely to occur when the flow velocity approaches zero. For such cases, the Doppler frequency is the small difference between two large values. Here, the relative error is inversely proportional to the Doppler frequency. The relative error of the Doppler frequency has a maximum value as the Doppler frequency approaches zero.

Figure 7.5.2 shows the relative error for frequency shifts of 0, 250, and 500 kHz. The 500 kHz value is the upper limit for the range of frequency shift used in this experiment. The positive values of Doppler frequency are plotted for a counter with a bandwidth set to accept signals between 64 kHz to 1 MHz. Since the detected frequency is limited to 1 MHz, the maximum possible Doppler frequency is given by this value minus the frequency shift. For example,

FIGURE 7.5.2

PERCENTAGE CLOCK ERROR VS DOPPLER FREQUENCY (HZ)

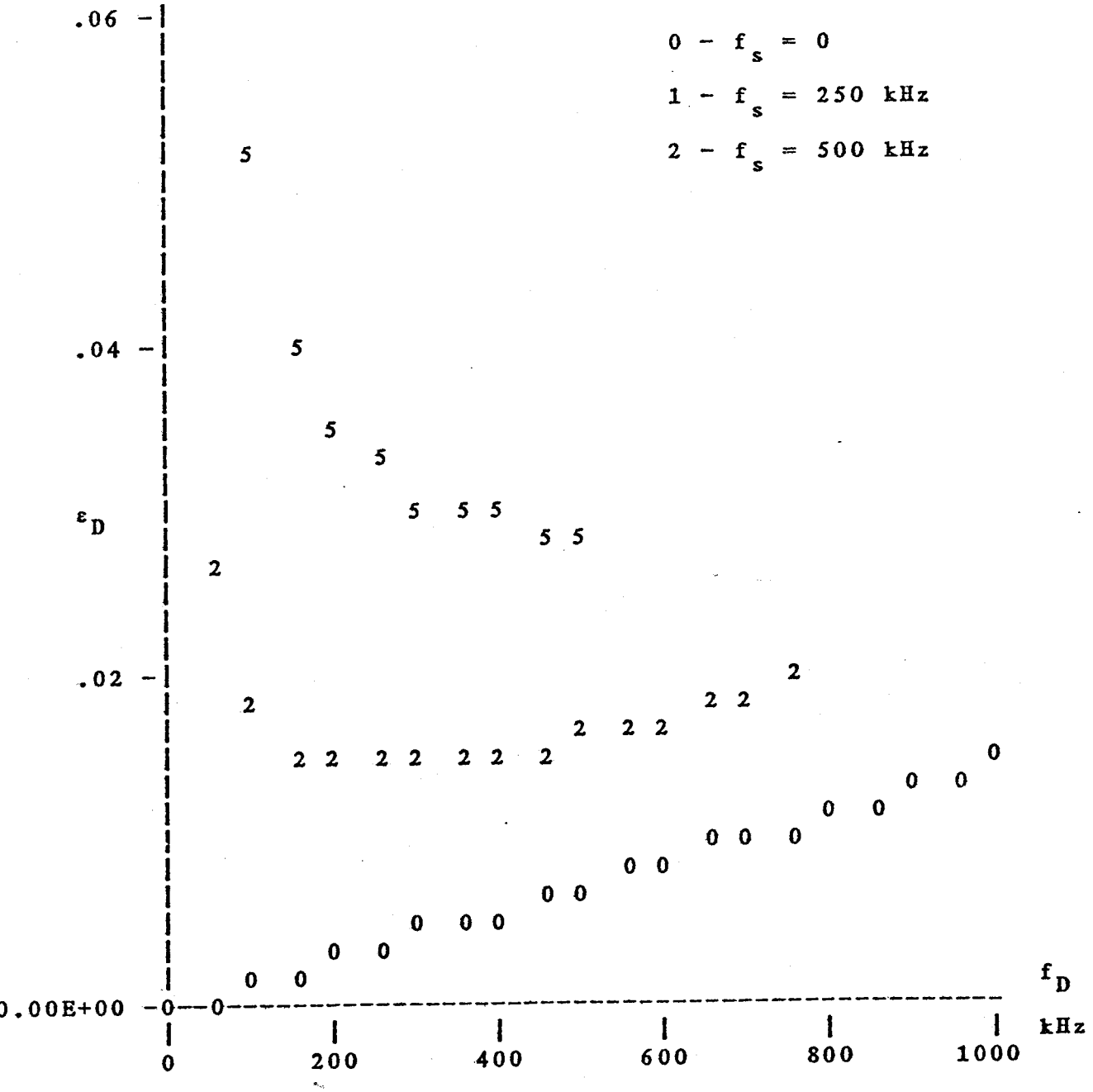

given a frequency shift of 250 kHz, the maximum Doppler frequency is

$$f_D = 1\text{MHz} - 250\ \text{kHz} = 750\ \text{kHz}.$$

For zero shift, the presence of the high pass filter prohibits signal frequencies below 64 kHz.

For zero shift, the relative error is directly proportional to the Doppler frequency. Equation (7.5.6) reduces to a straight line depicted by the bottom curve in Figure 7.5.2. If this line is extended beyond the high-pass filter cut-off frequency, it would pass through the origin.

With nonzero shift, the $1/f_D$ dependence near the origin becomes clear. For a given Doppler frequency, increasing values of shift increase the relative error. If the Doppler frequency could increase indefinitely, these curves would eventually merge with the zero shift case. Fortunately, the relative error is still only fractions of a percent. Given a 500 kHz shift, the relative error is 3% for a Doppler frequency of 1200 Hz (approximately 1.3 cm/s). It may be concluded that the effect of clock error is negligible for the equipment used in the velocity field under investigation.

Once the measurement is completed, the contents of the high count register are hardware transformed to floating point format (see Figure 7.5.3). The ten most significant bits of the high count register are stored in the mantissa. Rounding does not occur, the remaining bits are ignored.

FIGURE 7.5.3

COUNTER TRUNCATION OF BURST TIME

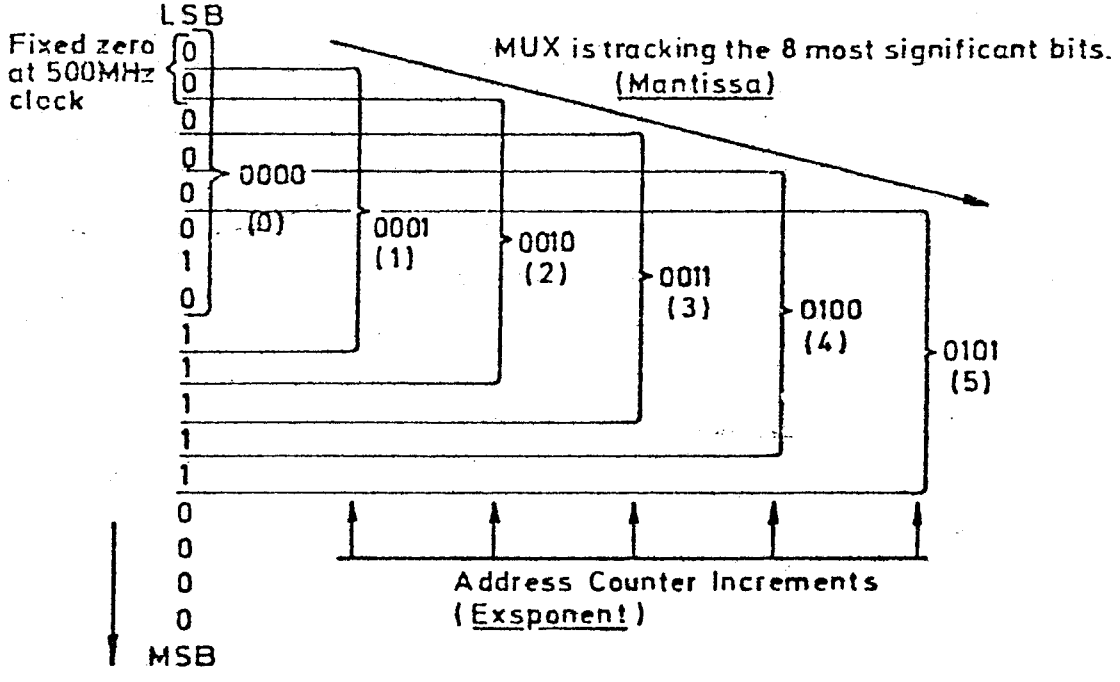

9. The contents of the binary counter may have a value of up to 21 bits. These data are not transmitte 21 bits of data, but divided into 8 bits mantissa multiplied by the 4 bit exponent. The figure illustrate v the data format is formed. The Multiplexer board follows the eight most significant bits at any tim en the 8 bits shifts from 1111 1111 to 0000 0000 and the succeeding bit shifts to logic '1', the mult xer jumps one step up and still "looks at" the 8 most significant bits. At the same time the ADDRES UNTER states the exponent.

The largest error condition will occur when the MSB is set to one, the remaining nine bits of the mantissa are zero, and the truncated bits are all ones. For this case the relative error is one part in 2^9. The relative error due to truncation is expected to have the following range of values.

$$\varepsilon_{Pt} = \frac{P_8(\text{actual}) - P_8(\text{truncated})}{P_8} \times 100\% \qquad (7.5.7)$$

$$100/2^9 > \varepsilon_{Pt} > 0$$

$$0.19 > \varepsilon_{Pt} > 0$$

The same analysis presented previously in this section is now repeated. Assume the probability density function (p.d.f.) for the relative error is a top hat function. The mean value of the p.d.f. is adopted as the final estimate to the relative error. In general, for a mantissa with b bits,

$$\varepsilon_{Pt} = 2^{-b} \times 100\% \qquad (7.5.8)$$

$$\varepsilon_{Pt} = 0.39 \text{ for 8 bit mantissa}$$

$$\varepsilon_{Pt} = 0.098 \text{ for 10 bit mantissa}$$

The procedure to obtain the relative error of the Doppler frequency from the burst time error is the same as before

$$\varepsilon_{Dt} = \varepsilon_{dt} \, (f_d/f_D) = 2^{-b} \, (1 + f_s/f_D) \times 100\% \qquad (7.5.9)$$

The above equation is plotted in Figure 7.5.4 for a ten bit mantissa (for an 8 bit mantissa, simply multiply the

FIGURE 7.5.4

PERCENTAGE TRUNCATION ERROR VS DOPPLER FREQUENCY

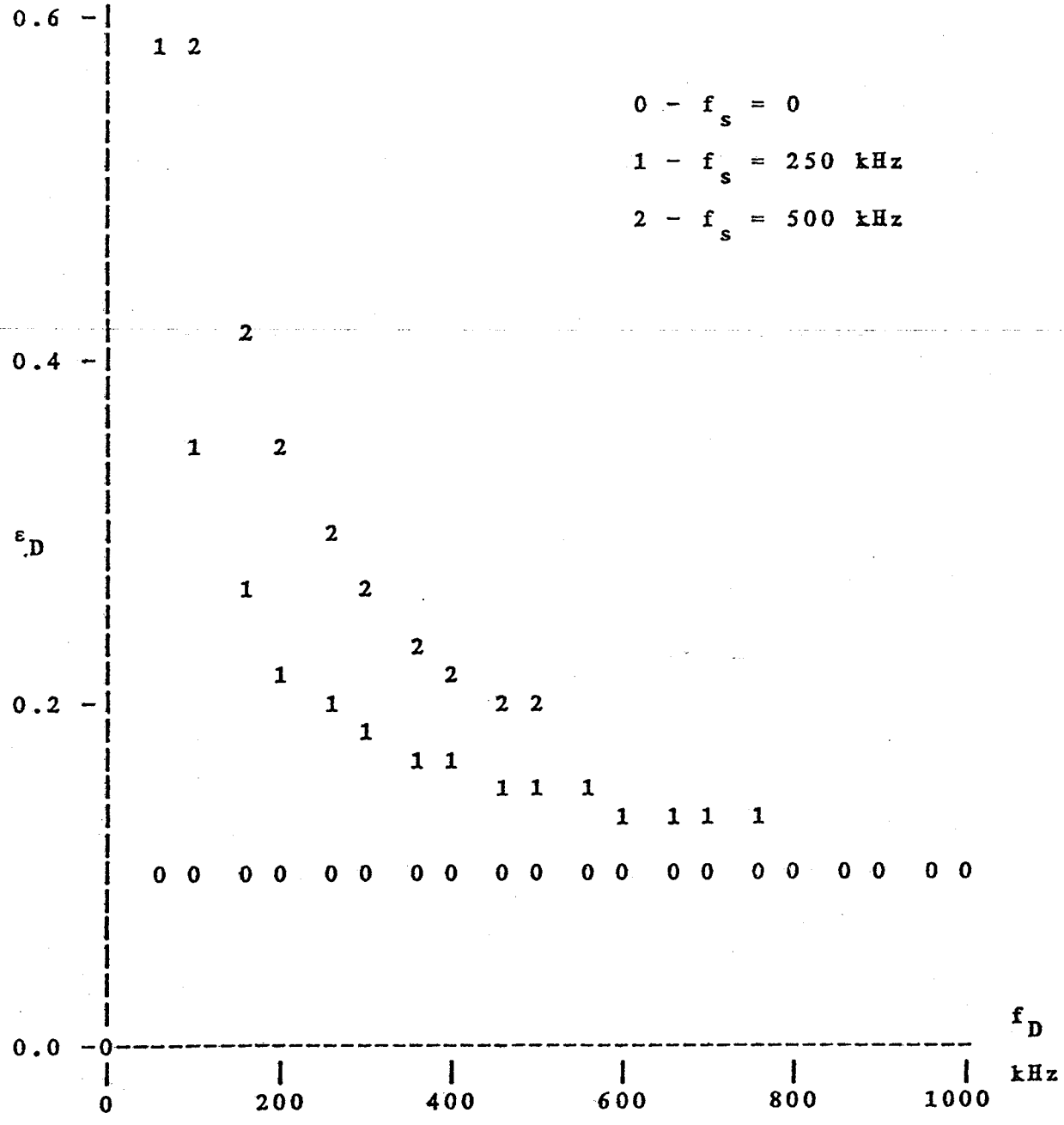

constant relative error for the burst time (regardless of frequency shift) and the Doppler frequency for a zero shift. Higher values of shift increase the error inherent in the Doppler frequency. Although the relative error due to truncation is an order of magnitude greater than the clock error, its effect still seems to be small. For example, even with a 500 kHz shift, the error in measuring a Doppler frequency of 50 kHz (about 54 cm/sec) is about one percent.

It has been shown that in most cases, the truncation error, not the clock error, is the source of greatest error. However, even the truncation error is normally a fraction of a percent. The major source of error in the estimate of the burst time and Doppler frequency is not in the digital hardware, but in the noise inherent in the received Doppler signal. It is the level of accuracy in 5:8 comparison test that limits the accuracy of the burst time and frequency measurements. For the DISA 55L90 counter, the minimum error is therefore 1.5%.

Section 7.6: Hardware Accuracy of Sample Inverval

The sample interval clock has a hardware design different from the electronics measuring the burst time. The period of the pulses, t_b, of the master or time base clock used to measure the sample interval time between successive data realizations, T, is user selected. These

time base pulses are counted in the eight bit T_m mantissa counter. The counter is incremented with each time base pulse and has an absolute error of plus or minus one time base clock pulse. At this point the output is in nonnormalized form. When the clock overflows on 256 counts, the T_x exponent is incremented. At the same time the T_m counter is reset to 128 (see Figure 7.6.1) and the period of the time base clock pulses is doubled. After the first overflow occurs, the accuracy of the sample interval clock is determined by its representation in floating point form. The behavior of the relative error for the sample interval may be treated in a fashion identical to the truncation error of the previous section (see Figure 7.6.2),

$$0 < \varepsilon_T < 2^{-b} \text{ X } 100\%$$
$$0 < \varepsilon_T < 0.39\ \% \qquad (7.6.1)$$
$$E\langle\varepsilon_T\rangle = 0.20\ \%$$
$$S\langle\varepsilon_T\rangle = 0.11\ \%$$

FIGURE 7.6.1

SAMPLE INTERVAL FLOATING CLOCK

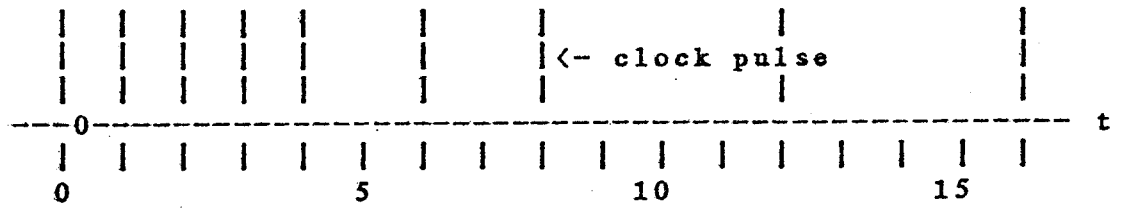

Binary contents of hardware clock for two bit mantissa

t	T_m	T_x
1	01	000
2	10	000
3	11	000
4	10	001
5	10	001
6	11	001
7	11	001
8	10	010

t	T_m	T_x
9	10	010
10	10	010
11	10	010
12	11	010
13	11	010
14	11	010
15	11	010
16	10	011

FIGURE 7.6.2

DIGITAL CLOCK MEASUREMENT ERROR - SAMPLE INTERVAL

Clock Measurement too Short

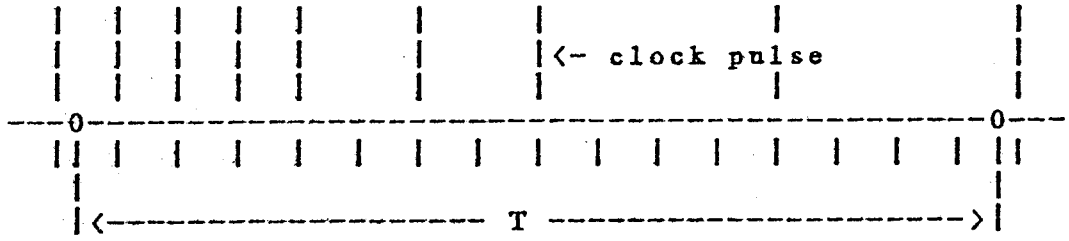

Elapsed time = 16 t_b
Measured time = 12 t_b
Relative error = $(16^b - 12)/16 = 1/4$

Clock Measurement too Long

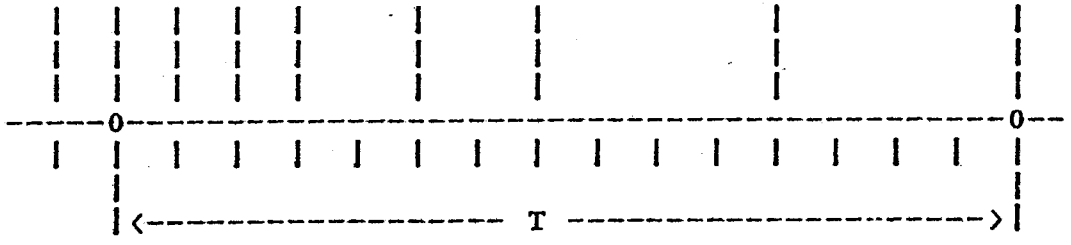

Elapsed time = 15 t_b
Measured time = 16 t_b
Relative error = $(15^b - 16)/15 = -1/15$

Note the measured time can be at most t_b longer than the elapsed time. As the elapsed time becomes large, the relative error approaches zero for those cases in which the clock measurement is too long.

Chapter 8: Validation of Measurement Techniques

Section 8.1: Software Programming Considerations and Relative Errors of Statistical Estimates

Because of the need to investigate software verification methods for the LDA counter, special software was written for this experiment. The verification methods to be investigated included over a half dozen different statistical functions. Because of the large number of operations to be performed, it was not feasible to analyze the data in real time. Instead, all measurements were to be stored on disk.

In the preceding chapter it has been shown that the computation of the flow field statistics requires residence time weighting to avoid the bias errors arising from the correlation between the sampling rate and flow field. Record lengths or batches longer than two integral scales are taken, then each realization within this period is averaged using residence time weighting, and the results of successive batches are arithmetically averaged to form a final time average. All single channel measurements were recorded using this technique.

Recall that when moments of a p.d.f. are being computed, the statistical convergence of these moments is determined by the number of independent samples (see section 7.3). Since it is often impossible to control the particle seeding accurately enough to guarantee that every sample is

statistically independent and since the residence time weighting requires that every sample to arrive during the sample period be processed, storage space on the disk may not be optimized.

In order to minimize storage space for the two component measurements, the following technique was adopted. The computer records a sample, waits two integral scales, records the next sample to occur, and repeats the cycle until the desired number of realizations have been recorded. Consequently, every recorded value is statistically independent of the other. To calculate the time lag between each measurement, the integral scale, τ_u, is estimated using the data of Wygnanski and Fiedler. For a nondimensional radial coordinate η less than 0.10, the integral scale is inversely proportional to the local mean axial velocity, U and proportional to the axial coordinate, x, thus

$$\tau_u = 0.042\ x/\bar{U} \qquad (8.1.1)$$

For values of η greater than 0.10, the constant in the above equation decreases as η increases. Although the relation does not hold across the entire profile, it does provide a reasonable estimate by which the time lag between samples may be set. Figure 8.1.1 shows the integral scale for the two locations at which profiles were measured. These values were computed using the mean velocity profile of Seif. The increase in the time scale as the radial

FIGURE 8.1.1

VARIATION OF INTEGRAL SCALE ACROSS PROFILE

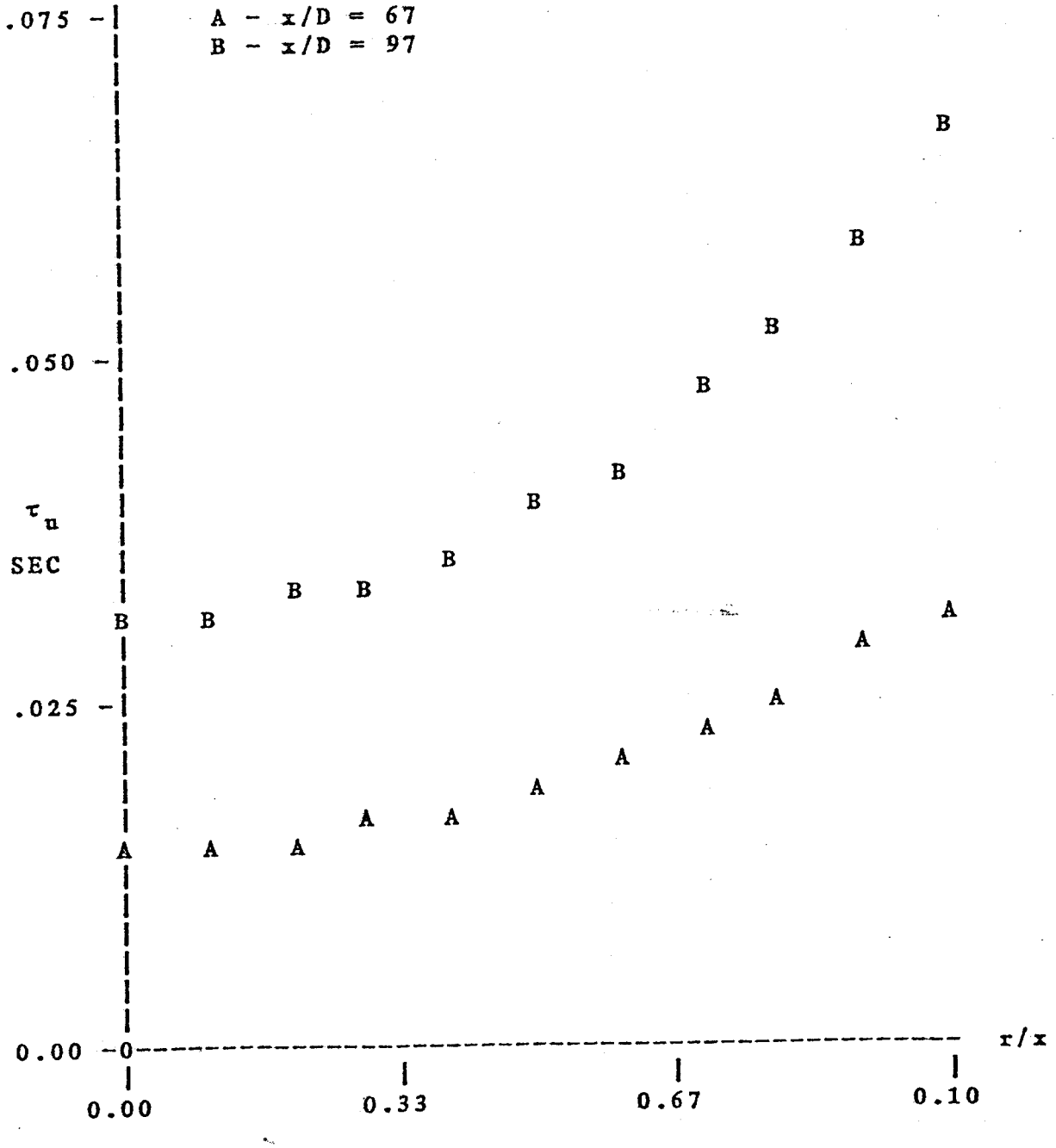

coordinate increases may be attributed to the decrease in the local mean velocity. The eddies are swept past a point at a slower rate, so the integral time scale becomes larger.

Based on these values, the programmed time lag for the two channel measurements was set to 0.1 second. This was not, however, the average time period between samples. Recall that the counter must wait for a validated realization before accepting the measurement. Because of the sparse seeding, a typical data rate was between three to five hertz so that the average time between samples was between 0.2 to 0.3 seconds. For the two component measurements, taken with N statistically independent realizations, the variance of the sample mean, U_{sm}, is related to the variance of the measured velocity, U_M.

$$Var[U_{sm}] = \frac{Var[U_M]}{N} \qquad (8.1.2)$$

The relative error for the sample mean is

$$\varepsilon[U] = \frac{Std[U_{sm}]}{\overline{U}^2} \times 100\% \qquad (8.1.3)$$

The preceding chapter has established that hardware errors are negligilble compared to turbulence intensity levels in the flow. As a result, the variance of the measured velocity is simply the variance of the true velocity field. The relative error for the measurement of the mean velocity is

$$\varepsilon[U] = \frac{1}{N^{1/2}} \frac{u}{U} \times 100\% \qquad (8.1.4)$$

Taking the worst case condition at the outer edge, say a turbulence intensity of 100%, the relative error for the mean velocity is computed. Since 8400 samples were taken per data point, the expected accurracy is roughly 1.1%. The observed scatter was closer to 4% for the mean values.

A similar procedure can be followed for the higher moments. It can be shown that

$$\mathrm{Var}\left[\overline{u_s^n} \right] = \frac{\overline{u^{2n}}}{N} \qquad (8.1.5)$$

The third and fourth moments measured by Wygnanski and Fiedler in the jet exhibited Gaussian behavior up to a radial coordinate of $\eta = 0.10$. Assuming a Gaussian distribution for the velocity, the relative error for the turbulent normal stress can be easily calculated

$$\varepsilon\left[\overline{u^2} \right] = \frac{3}{N^{1/2}} \times 100\% \qquad (8.1.6)$$

Using the above values, a 3% error in the turbulent stress terms is predicted, a number matching the observed scatter. Note that Tennekes and Wyngaard (1972) have shown the error might be considerably higher for a distribution which is not Gaussian.

For the single channel measurements, the flow field was continuously sampled. The seeding rate was increased so that the average data rate was 70 samples per second for a sample period of 0.014 seconds. This rate is high enough so

that the statistics of convergence is essentially dominated by the total sample period. This sample period, T_s, was 250 seconds. When these values are substituted into equation (7.3.16b) with a time scale of .050 seconds, the relative error is

$$\varepsilon[U] = 2\% \qquad (8.1.7)$$

The discrepency between the calculated error bounds and the observed scatter in the data can only be attributed to a slow oscillation or random meandering of the jet. Such an effect is probably due both to the back flow and the nonsymmetric enclosure. The return flow was not a uniform laminar flow, for at times large bursts of fluid could be observed being swept back along the outer edges of the enclosure.

Section 8.2: Particle Path Lengths in Optical Probe Volume

In the next section a probability distribution function is derived for the path length of the particles through the optical probe volume. The 1975 article by Buchhave provides the foundation for this analysis(v. Buchhave 1976). He developed an exact formula for the path length of an arbitrary trajectory through the probe volume. He further developed this relationship to find the surface area in which passing particles would have a path length greater than or equal to a certain value. Buchhave used these results in his investigation of the angular bias discussed

in section 7.4. His analysis is repeated here for completeness. These results are then used in the next section to develop a probability distribution function for the path length in a uniform laminar flow field.

The optics are operating in dual beam, differential Doppler mode. To simplify the mathematics, the optical probe volume and the measuring volume are assumed to be identical. In other words, a signal is seen by the processing hardware whenever a particle is within the optical probe volume. The $1/e^2$-intensity boundaries of the optical probe volume are assumed equivalent to the physical area in space in which a signal from the particle exceedes the counter trigger level. The x, y, z coordinate system is defined with respect to the optic axis of the intersecting laser beams. The plane of fringes is perpendicular to the x-axis. The z-axis is parallel to the fringes and oriented such that the x-z plane contains the intersecting laser beams (see Figure 8.2.1) In this system, the ellipsoidal optical probe volume is given by

$$\left[\frac{x}{a}\right]^2 + \left[\frac{y}{b}\right]^2 + \left[\frac{z}{c}\right]^2 = 1 \qquad (8.2.1)$$

Consider an arbitrary straight line particle trajectory, $\underline{1}$. The line parallel to this path and passing through the origin of the x, y, z coordinate system defines the 1-axis and a second coordinate system. Let α be the angle between the z and 1 axes. The angle between the

FIGURE 8.2.1

PROBE VOLUME COORDINATE SYSTEM

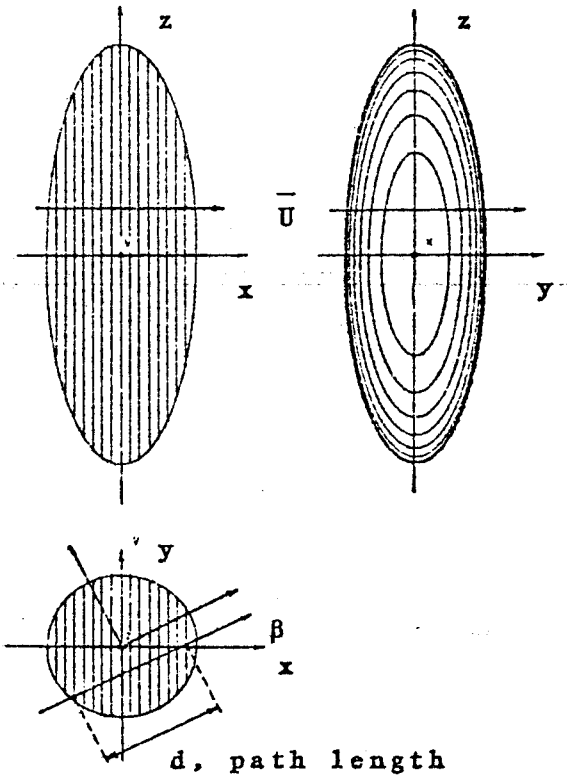

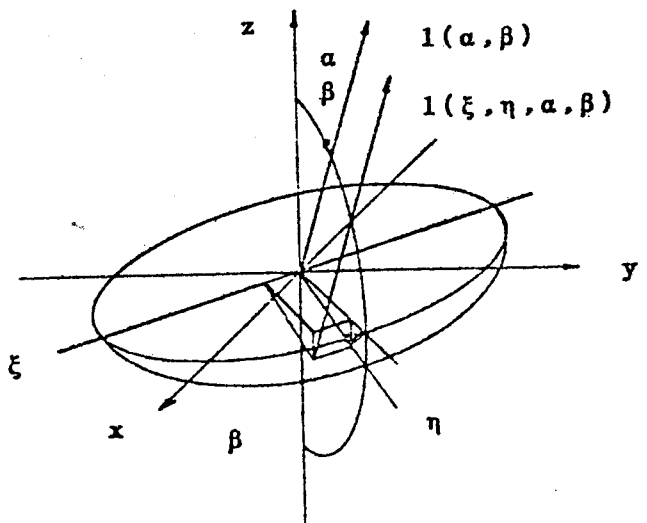

x-axis and the projection of $\underline{1}$ onto the x-y plane is β. The plane perpendicular to $\underline{1}$ and containing the origin of the x, y, z system defines the ξ, η axes, the ξ-axis being the intersection of the x-y plane and the ξ, η plane. The mapping of a point from the second to the first coordinate system is given by

$$\begin{aligned} x &= 1\sin\alpha\cos\beta + \xi\sin\beta + \eta\cos\alpha\cos\beta \\ y &= 1\sin\alpha\sin\beta + \eta\sin\beta\cos\alpha - \xi\cos\beta \\ z &= 1\cos\beta + \eta\sin\beta \end{aligned} \qquad (8.2.2)$$

The surface of the probe volume may now be expressed in the new coordinate system

$$A1^2 + B1 + C = 0 \qquad \text{with the coefficients}$$

$$\begin{aligned} A &= (\cos^2\beta\sin^2\alpha)/a^2 + (\sin^2\beta\sin^2\alpha)/b^2 + (\cos^2\alpha)/c^2 \\ B &= (2\sin\alpha/a^2)(\xi\sin\beta\cos\beta + \eta\cos^2\beta\cos\alpha) \\ &\quad + (2\sin\alpha\sin\beta/b^2)(-\xi\cos\beta + \eta\sin\beta\cos\alpha) \\ &\quad + (-2\eta\sin\alpha\cos\alpha)/c^2 \\ C &= (\xi^2\sin^2\beta + \eta^2\cos^2\beta\cos^2\alpha + 2\xi\eta\sin\beta\cos\beta\cos\alpha)/a^2 \\ &\quad + (\xi^2\cos^2\beta + \eta^2\sin^2\beta\cos^2\alpha - 2\xi\eta\sin\beta\cos\beta\cos\alpha) \\ &\quad + (\eta^2\sin^2\alpha) - 1 \end{aligned} \qquad (8.2.3)$$

The particle path through the measuring/probe volume is uniquely determined by the angles α and β and the coordinates ξ and η. The two values of 1 at which the trajectory intersects the ellipsoid's surface may be found by solving the above equation using the quadratic formula. The solution is

$$1_{\pm} = \frac{B \pm (B^2 - 4AC)^{1/2}}{2A} \qquad (8.2.4)$$

The particle path length, d, is also function of α, β,

ξ and η. Its magnitude is the difference of the two values of 1 given by equation (8.2.4), thus

$$d = (1_+ - 1_-) = \frac{(B^2 - 4AC)^{1/2}}{A} \qquad (8.2.5)$$

The counter can only supply information concerning the x-component of velocity, U, and the total time required to cross the measuring volume, P. For this reason it is convenient to deal with the component of the particle path length along the x-axis, d_x, given by

$$d_x = U\,P = d\,\cos\beta\sin\alpha$$

$$d_x = \frac{(B^2 - 4AC)^{1/2}}{A}\,\cos\beta\sin\alpha \qquad (8.2.6)$$

The path length is maximized for a trajectory passing through the center of the ellipsoid. For such a particle, ξ and η are zero. Using equations (8.2.3) and (8.2.6) it can be shown that the expression for the maximum possible path length, d_{xm}, given a fixed velocity vector is

$$d_{xm} = 2\cos\beta\sin\alpha/A^{1/2} \qquad (8.2.7a)$$

$$d_{xm} = 2a\left[1 + \frac{a^2}{b^2}\tan^2\beta + \frac{a^2}{c^2}\,\frac{1}{\cos^2\beta\tan^2\alpha}\right]^{-1/2}$$

The angles α and β are functions of the velocity vector. The maximum path length can therefore be expressed in terms of the components of the velocity vector (i.e. U, V and W) as

$$\tan\alpha = (U^2 + V^2)^{-1/2}/W$$

$$\cos\beta = U/(U^2 + V^2)^{1/2} \qquad (8.2.7b)$$

$$\tan\beta = V/U$$

$$d_{xm} = 2U \left[\frac{U^2}{a^2} + \frac{V^2}{b^2} + \frac{W^2}{c^2}\right]^{-1/2}$$

Equation (8.2.6) provides greater information if interpreted from a slightly different viewpoint. This relation may be rearranged to determine what values of ξ and η produce a constant path length d_x. Equation (8.2.6) may be represented in the following fashion

$$K\xi^2 + L\eta^2 + M\xi\eta + N = 0$$

$$K = \frac{\sin^2\alpha}{a^2b^2} + \frac{\sin^2\beta\cos^2\alpha}{a^2c^2} + \frac{\cos^2\beta\cos^2\alpha}{b^2c^2} \qquad (8.2.8)$$

$$L = \frac{\cos^2\beta}{a^2c^2} + \frac{\sin^2\beta}{b^2c^2}$$

$$M = 2\sin\beta\cos\beta\cos\alpha \left[\frac{1}{a^2c^2} - \frac{1}{b^2c^2}\right]$$

$$N = -\left[\frac{\cos^2\beta\sin^2\alpha}{a^2} + \frac{\sin^2\beta\sin^2\alpha}{b^2} + \frac{\cos^2\alpha}{c^2}\right](1 - Q^2(1 +$$

$$+ \frac{a^2}{b^2}\tan^2\beta + \frac{a^2}{c^2}\frac{1}{\cos^2\beta\tan^2\alpha}))$$

$$Q = d_x/2a$$

This form is the same as that in Buchhave's publication. For future use, it will prove to be more convenient to represent the coefficient N in terms of A (equation 8.2.3) and the maximum possible path length, d_{xm} in (equation 8.2.7), i.e.

$$N = -A\left[1 - \left[\frac{d_x}{d_{xm}}\right]^2\right] \qquad (8.2.9)$$

Equation (8.2.8) defines an ellipse within the ξ-η plane. Any particle path passing inside the ellipse will have a path length greater than or equal to d_x. To find the area of the ellipse, a third and final coordinate transformation is applied. A new set of axes in the ξ-η plane is defined so that these new axes (ξ' and η') are aligned with the axes of the ellipse given in equation (8.2.8). The new coordinates are defined to remove the cross product term $M\xi\eta$.

$$\begin{aligned} \xi &= \xi'\cos\gamma - \eta'\sin\gamma \\ \eta &= \xi'\sin\gamma + \eta'\cos\gamma \end{aligned} \qquad (8.2.10)$$

This product term is zero when

$$\tan\gamma = \frac{K - L}{M} \pm \left[\left(\frac{K - L}{M}\right)^2 + 1 \right] \qquad (8.2.11)$$

Equation (8.2.8) expressed in the $\xi' - \eta'$ plane is

$$\frac{\xi'^2}{a'^2} + \frac{\eta'^2}{b'^2} = 1$$

$$a'^2 = \frac{N(1 + \tan^2\gamma)}{K - M\tan\gamma + L\tan^2\gamma} \qquad (8.2.12)$$

$$b'^2 = \frac{N(1 + \tan^2\gamma)}{L - M\tan\gamma + K\tan^2\gamma}$$

The area enclosed by the ellipse is

$$S = \pi a'b' = \pi\left[\frac{N^2(1 + \tan^2\gamma)^2}{(K-M\tan\gamma+L\tan^2\gamma)(L-M\tan\gamma+K\tan^2\gamma)}\right]^{1/2} \qquad (8.2.13)$$

The above expression was used by Buchhave in his analysis of angular bias. The counter's requirement for a

minimum number of fringe crossings may be viewed in terms of a minimum path length. For a given frequency shift and velocity vector, he calculated the minimum path length needed to validate a signal. Suppose N_e fringes are needed for a measurement in the optical probe volume. This requires a minimum expected residence time P_e such that

$$P_e = \frac{N_e}{f_D + f_s} \tag{8.2.14}$$

As before, f_D is the Doppler frequency and f_s the frequency shift. The required minimum path length d_{xe} is then

$$d_{xe} = \frac{U\ N_e}{f_D + f_s} \tag{8.2.15}$$

This may be expressed in terms of the total number of fringes in the control volume (N_f) and the fringe velocity, U_s.

$$d_{xe} = 2a\ \frac{N_e}{N_f}\ \frac{1}{1 + U_s/U} \tag{8.2.16}$$

Note that as the frequency shift is increased, the minimum path length required is also decreased. This above relation may be used in equation (8.2.13) to evaluate the measuring area in the ξ-η plane. Any particle traveling through this measuring cross-section will produce a validated signal. Any particle path crossing the ξ-η plane outside of the measuring area will not cross enough fringes to produce a validated measurement.

Section 8.3: Probability Distribution Function for Particle Path Length in Laminar Flow

The results of the previous section can also be used to develop an expression for the probability distribution function for the path length in a laminar flow field. For uniform seeding, the point at which a particle crosses the $\xi-\eta$ plane is arbitrary and can be regarded as a random variable. All points in the $\xi-\eta$ plane have an equal probability of being in the crossing path. Because the x-component of the path length, d_x, is a function of this intersection point, it also is a random variable. It is expected that the exact form of the probability distribution function is dependent on probe volume size (a, b, c) and the the velocity vector (i.e. α and β are a function of $\underline{U}$). The number of particles crossing a surface in the $\xi-\eta$ plane is directly proportional to the surface's area. If a detector is sensitive only in the area defined by this surface, the probability of detecting a particle within a fixed period of time is clearly a function of the area. If the area is doubled, the probability of detecting a particle within that fixed time span would also be doubled. In a similar fashion, it can be said that the probability of a detected particle having a path length greater than δ may be determined by taking the surface area through which a particle will have a path length greater than δ, say $S(\delta)$) and dividing this quantity by the measuring area $S(d_{xe})$, i.e.

$$P[d_x > \delta] = \frac{S(\delta)}{S(d_{xe})} \qquad (8.3.1)$$

The probability for $P[d_x > d_{xe}]$ is equal to one. This is as expected since all detected particles must have a path length greater than d_{xe}, the minimum path length required for a particle to be detected. As δ increases, the area containing path lengths greater than or equal to this value decreases, so the probability of such an event decreases. Eventually, for large enough δ, $S(d_x=\delta)$ equals zero and the probability of finding a path length greater than this value is also zero. Examination of equation (8.2.8) reveals that the expression for S contains the functions K, L, M, N, Q and $\tan\gamma$. Note that K, L, M and $\tan\gamma$ are dependent on a, b, c, ξ and η only and are independent of the path length, d_x. Upon substitution of equations (8.2.8) and (8.2.9) into (8.3.1), the terms containing these functions cancel and equation (8.3.1) reduces to

$$P[d_x > \delta] = \frac{N(\delta)}{N(d_{xe})} = \frac{R(\delta)}{R(d_{xe})} \qquad (8.3.2)$$

for $R(\delta)$ given by

$$R = 1 - \left[\frac{\delta}{d_{xm}}\right]^2$$

Examining the above expression for the function R, it is clear that the mathematics can be further simplified when expressed in a non-dimensional form. The normalizing factor

is the maximum possible path length, d_{xm}.

$$\lambda = d_x/d_{xm} \qquad \lambda_e = d_{xe}/d_{xm} \tag{8.3.3}$$

$$P[\lambda>\delta] = \frac{1 - \lambda^2}{1 - \lambda_e^2} \quad \text{for } \lambda_e \leq \lambda \leq 1$$

The utility of such a form is apparent when this variable is expressed in terms of either the fringe count, N, or the residence time, P.

$$\lambda = \frac{d_x}{d_{xm}} = \frac{UP}{UP_m} = \frac{P}{P_m} \tag{8.3.4}$$

$$\lambda = \frac{P}{P_m} = \frac{N/(f_D + f_s)}{N_m/(f_D + f_s)} = \frac{N}{N_m}$$

The cumulative distribution function (F) is given by

$$F[\delta] = P[\lambda<\delta] = 1 - P[\lambda>\delta] \tag{8.3.5}$$

$$F[\lambda] = \frac{\lambda^2 - \lambda_e^2}{1 - \lambda_e^2} \qquad \text{for } \lambda_e<\lambda<1$$

The probability distribution function of a variable is the derivative of the cumulative distribution function with respect to that variable. The derivative of the preceding equation is

$$P[\lambda] = \frac{2\lambda}{1 - \lambda_e^2} \qquad \text{for } \lambda_e<\lambda<1 \tag{8.3.6}$$

The probability distribution function of λ given $\underline{U}$ is a straight line. It does not matter whether the path length, fringe count or residence time is being examined, for when expressed in suitable nondimensional form all variables have the same probability distribution function.

To measure this function, the following steps must be performed. First, the velocity vector of the laminar flow must be known. Based on the orientation of the velocity vector with respect to the axes of the optical probe volume, α and β are determined. The x-component of the maximum possible path length is then computed using equation (8.2.7). This may then be used to compute the normalizing coefficient.

Such a procedure is followed for the histogram produced in Figure 8.3.1. This is the only plot presented in this dissertation which is not data resulting from the use of the five watt Argon-ion laser. Instead, a second Disa 55X optical system with a Helium-Neon laser as the light source was used for the measurements. For maximum signal strength, these measurements were also taken in a forward scatter mode. The seeding technique was unchanged.

The x-axis of the probe volume is aligned with the direction of the flow (i.e. V=W=0). The spacing between fringes, δ_f, is approximately 15 μm with a maximum path length along the x-axis of .23 mm. The measurements were recorded with a frequency shift of 200 kHz. The non-dimensional path length is expressed in terms of the fringe count since the fringe count is an integer value. An integer value requires less storage space (one word for an integer value versus two words for a single precision real value) and arithmetic operations involving integers may be

FIGURE 8.3.1

PROBABILITY DISTRIBUTION FUNCTION OF λ IN A LAMINAR FLOW

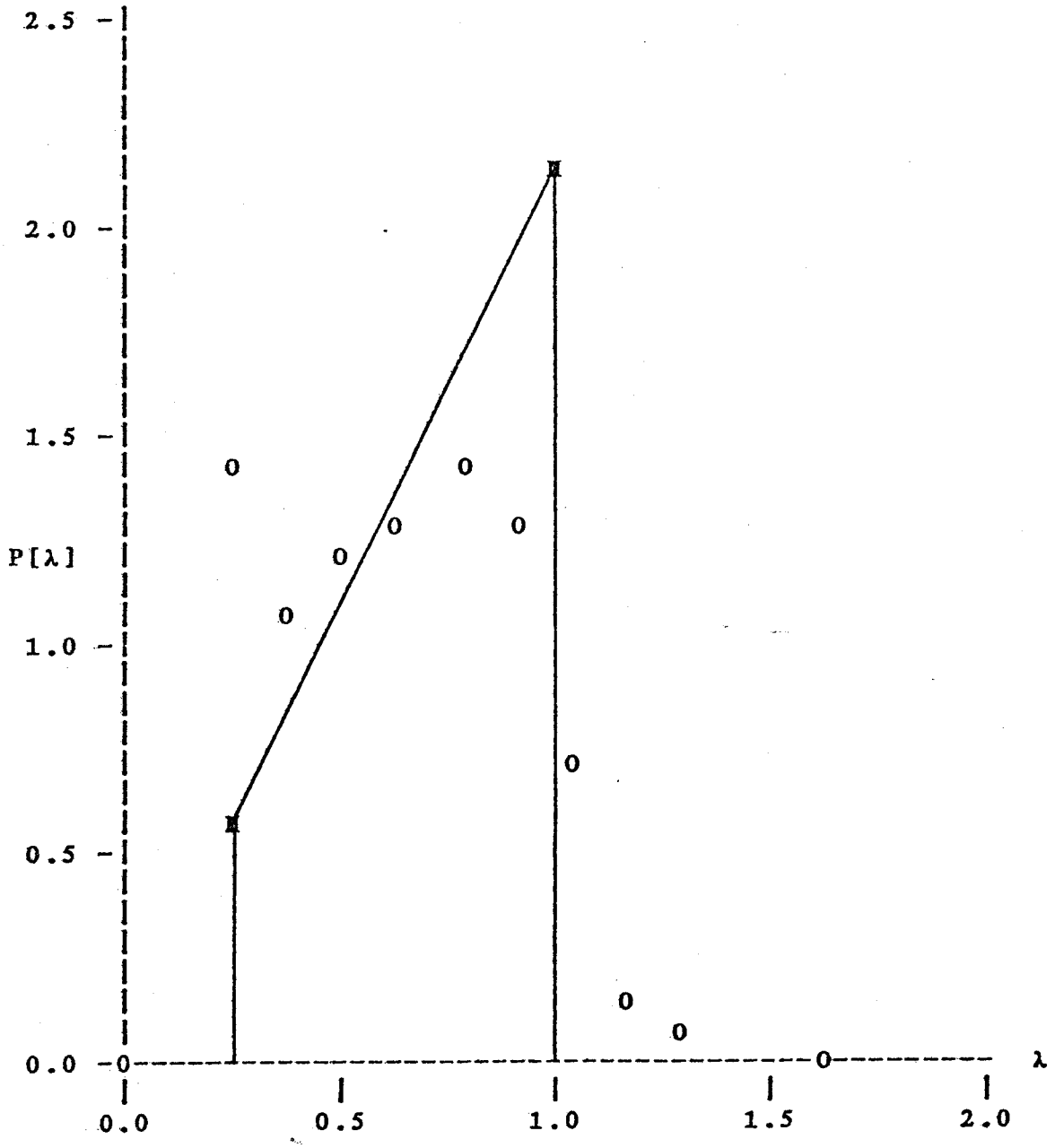

performed at a faster rate than real operations. The maximum number of expected fringes is estimated as follows:

$$f_D = U/\delta_f = 0.19 \text{ MHz}$$
$$P_m = 2a/U = 81 \ \mu s \qquad (8.3.7)$$
$$N_m = (f_D + f_s) P_m = 31 \text{ fringes}$$

Unfortunately, the theoretical prediction differs from the actual measurements. The experimental values for the distribution function have a significantly higher value for the lower values of λ (i.e. low burst times and low fringe counts). The p.d.f. does not peak as high as expected, but the cut-off point is correctly predicted. It is believed the reason for this behavior is found in the range of particle sizes. Recall the derivation for the angular bias and the probability distribution function of the non-dimensional path length has assumed the counter trigger level to be equivalent to the $1/e^2$ intensity level of the intersecting laser beams. However, the intensity of the scattered light has a strong functional dependence upon the particle size. Smaller diameter particles will produce recognizable signals only over a smaller measuring volume size. They will therefore have smaller values for the maximum possible values of path length, burst time, or fringe count. Thus lower values become more probable than would be expected from the nondisperse theory developed here.

Such an effect might also be due to high particle

concentrations. Suppose a particle is in the measuring volume and has crossed enough fringes to fulfill the 5-8 comparison test. A second particle now enters the volume and the signals from the two particles interfere with one another. The amplitude modulation of the resultant signal (see Figure 8.3.1) can cause the counter to prematurely mark the end of a burst and reset before the first particle leaves the measuring volume. The measured path length, fringe count, and residence time are truncated. For the measurements shown in Figure 8.3.1, the low seed concentrations and visual observation of the filtered Doppler signal during the sampling interval indicate that this error condition was rare. It seems the difficulty in matching theoretical and experimental result to the probability distribution function is primarily due to the spread in particle size. There seems to be no practical way to account for the effect of particle size upon the distribution function.

Section 8.4: Probability Distribution Function for Fringe Count in Turbulent Flow

For turbulent flow, a more serious implication of the results of Figure 8.3.1 are revealed if the effects of angular bias are reconsidered. Buchhave's analysis has assumed that the particle produces a measurable signal when the particle is the optical probe volume. The intensity of

the scattered light is a function of particle size. Larger particles reflect a stronger Doppler signal. For smaller particles the volume which produces a measurable signal is reduced and these smaller particles travel a shorter distance in which they must cross the required minimum number of fringes. As a result, the predicted amount of frequency shift required to produce an unbiased result for the smaller particles is underestimated. It is therefore suggested that before any data is taken, the experimenter check the characteristics of the seeding particles by examining a plot such as that presented in Figure 8.3.1. Although it can provide no quantitative data for the amount of frequency shift required, it can warn the experimenter if the initial conditions of Buchhave's model is applicable (i.e. given sufficient frequency shift, is the measuring volume the same as the optical probe volume for all particle sizes?).

The problem of angular bias arises because the counter requires a minimum number of crossings to validate a measurement. A crude indicator of angular bias can be found by examining the probability distribution of the fringe count. Infrequent occurrences of low fringe count values indicates the shift has been correctly set. If a significant number of realizations have a fringe count equal to or near the minimum requirement, it is probable that there has been a significant fraction of undetected

particles which have failed to cross the minimum number of fringes. A high incidence of low fringe counts indicates angular bias.

The results of the preceeding section can be used to predict the expected shape of the fringe count distribution function. Equation (8.3.4) can be regarded as a conditional distribution function when dealing with turbulent flows. Given a velocity vector, it determines the probability of the nondimensional path length. The nondimensional path length may be expressed as the fringe count divided by the maximum possible fringe count for that velocity vector (equation 8.3.6). By changing variables from λ to N, equation (8.3.4) can be used to determine the functional form for the probability of the fringe count given the velocity vector, thus

$$P[N|\underline{U}] = \frac{2N}{N_m^2 - N_e^2} \qquad (8.4.1)$$

$$N_m = \frac{d_{xm}}{C} |1 + f_s/f_D|$$

where C is the calibration factor given in equation 6.1.2 and d_{xm} is a function of $\underline{U}$ as given in equation 8.2.7.

Once a distribution function is defined for the velocity vector, the distribution function for the fringe count may be found using

$$P[N] = \int P[N|\underline{U}]\, P[\underline{U}]\, d\underline{U} \qquad (8.4.2)$$

The above equation is integrated over all possible velocity vectors. The results of a numerical integration

using the above approach are depicted in Figure 8.4.1. The parameters of the optical probe volume used in the integration are identical to those of the optics used in the jet experiment. For this plot, the mean velocity and frequency shift are held constant while the turbulence intensity is varied to determine its effect upon the probability distribution function of the fringe count. A normal distribution (or Gaussian distribution) is assumed for the flow field, i.e.

$$P[U] = \frac{e^{-(U - \bar{U})^2/2\sigma^2}}{\sigma\ (2\pi)^{-1/2}} \qquad (8.4.3)$$

where $\sigma^2 = \overline{u^2}$

A mean flow velocity of two meters per second with a frequency shift of 400 kHz is chosen to simulate the flow field seen towards the outer edge of the jet. The probability distribution function for the fringe count is shown for turbulent intensity levels of 10, 25 and 50%. The range of the numerical integration of the velocity field is plus or minus three standard deviations about the mean. Each step of the integration is 1/100 of the integration range. As a check, the distribution function of the fringe count is integrated and in all cases is within two percent of the expected value of one.

For a simple flow such as this, the velocity vector is always directed along the x-axis. The maximum path length for the theoretical model is therefore independent of the

FIGURE 8.4.1

THEORETICAL PREDICTION OF FRINGE COUNT HISTOGRAM
VARIATION WITH HIGHER TURBULENCE INTENSITY LEVELS

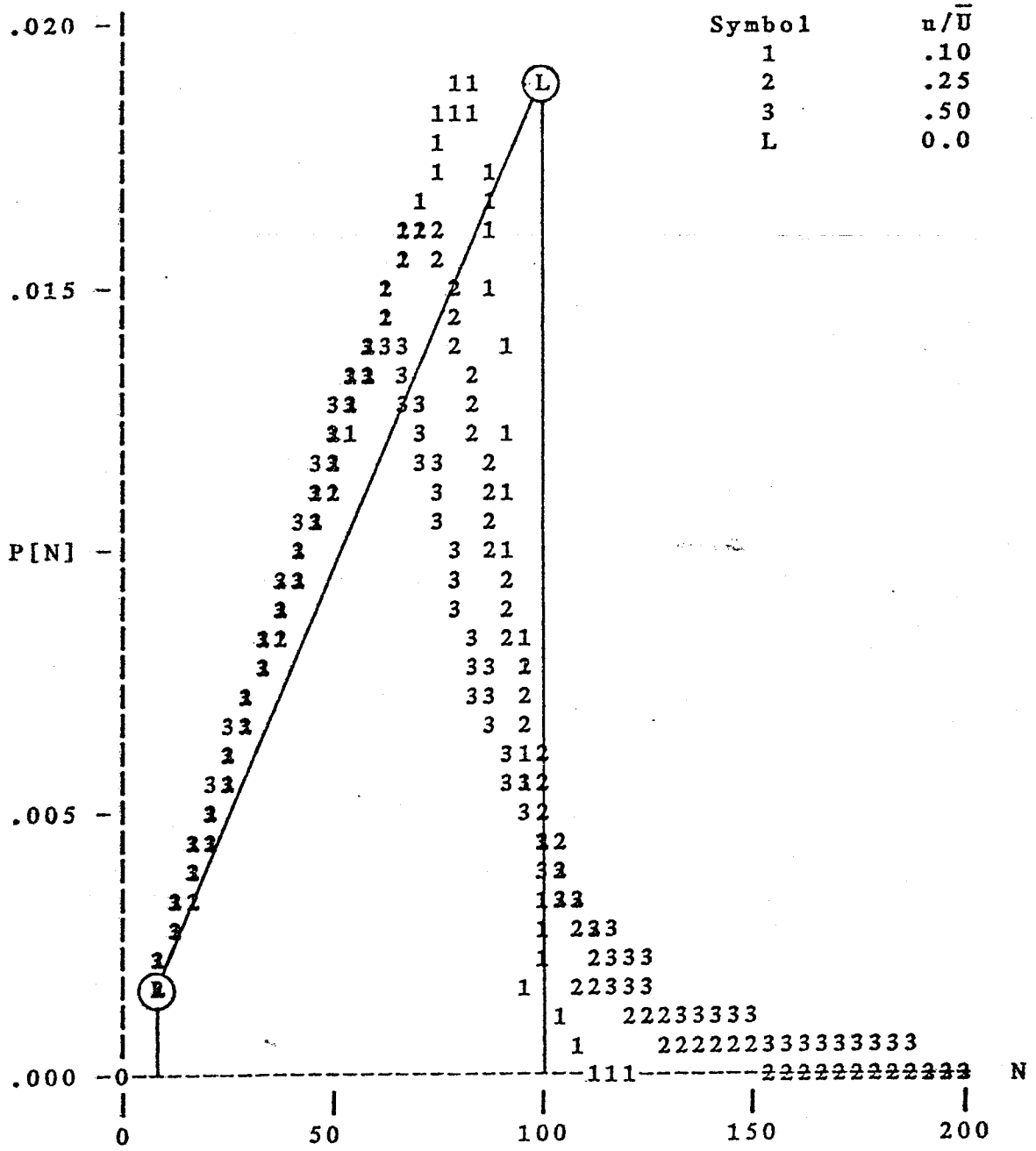

Mean velocity is two meters/second for all cases.
Frequency shift is 400 kHz.

velocity magnitude and is a constant with value 2a. This behavior pattern is not followed by the fringe count. Because of the frequency shift, the number of fringes a particle traverses in its flight across the measuring volume is a function of the residence time within the volume. Given the same path, a slower particle will cross more fringes than a particle moving at a higher speed. As the turbulence intensity is increased, the incidence rate of slower moving particles increases so that the probability of a higher fringe count also increases. In contrast to the sharp cut-off of the distribution function in laminar flow, the occurence of lower velocities with increasing turbulence levels cause a gradual decay of the fringe count distribution function. As in the laminar case, the distribution function of the fringe count for a turbulent flow initially displays linear behavior. The initial behavior seems to be largely governed by the mean velocity and frequency shift. It is a very weak function of the turbulence intensity level.

Of course, turbulence is a three-dimensional phenomena. The one-dimensional flow field used above does not reveal behavior patterns for those cases where the instantaneous velocity vector is not aligned with the x-axis. In Figure 8.4.2, the fringe count distrbution function is plotted for both one and two dimensional flow fields. A bivariate normal distribution models the turbulence. The correlation

FIGURE 8.4.2

THEORETICAL PREDICTION OF FRINGE COUNT DISTRBUTION FUNCTION
SHIFT FROM 1-D TO 2-D TURBULENT FLOW FIELD

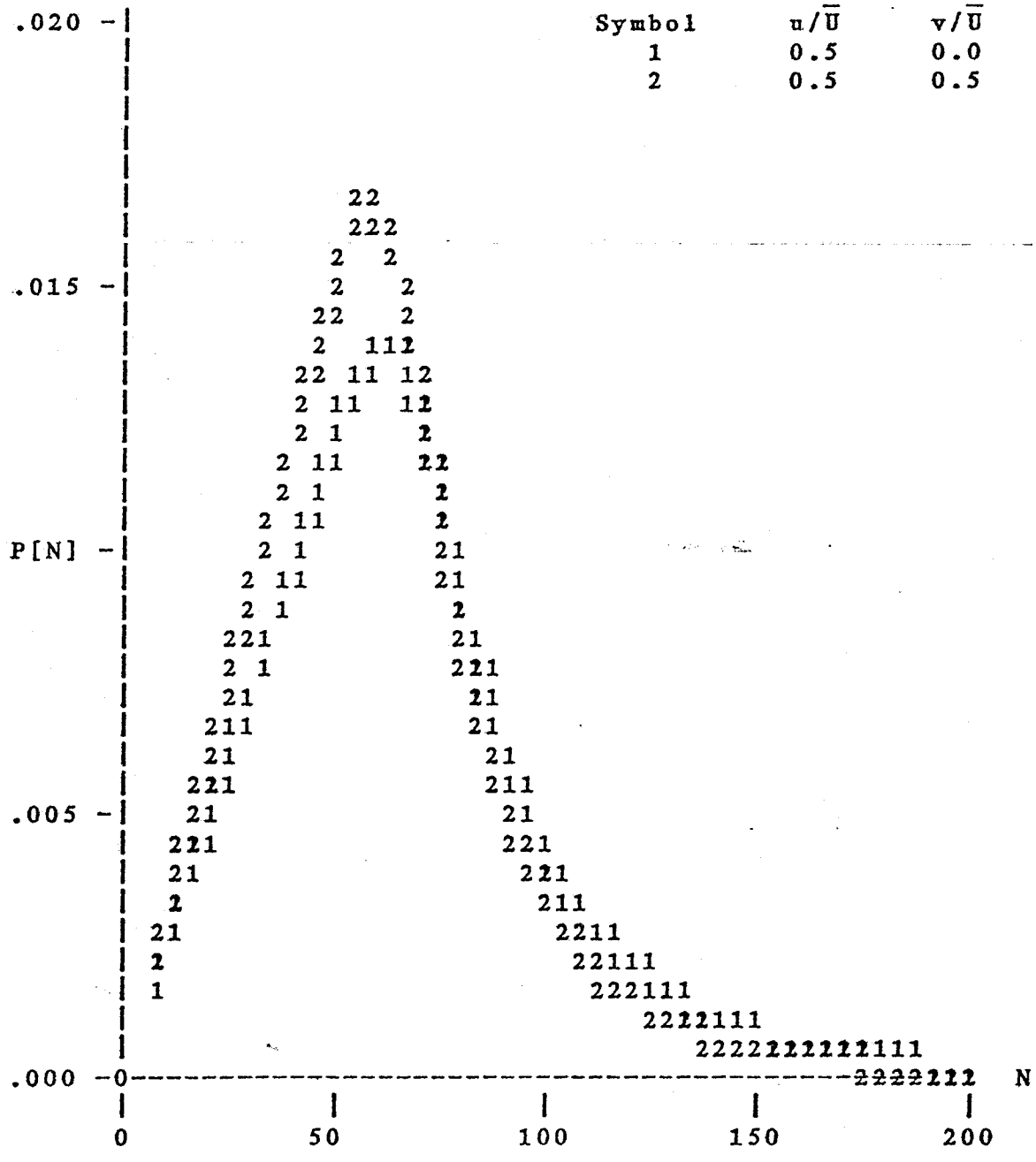

Mean velocity is two meters/second for both cases.
Frequency shift is 400 kHz.

coefficient between the two velocities, uv, is zero. The mean velocity is again directed along the x-axis with a value of two meters per second. The normal Reynold's stresses of both velocity components are assumed equal. The turbulence intensity level is fifty percent. The probablity distribution for the velocity field under these constraints is

$$P[N] = \frac{e^{-((U - U)^2 + W^2)/2\sigma^2}}{2\pi\ \sigma^2} \qquad (8.4.4)$$

where $\sigma^2 = \overline{u^2} = \overline{v^2}$

Note the component of velocity perpendicular to the optic axis and parallel to the fringe plane, V, is chosen as the second component of velocity. A shift of the velocity vector toward this axis causes a greater decrease in the maximum possible path length than when the velocity is directed along the optic axis. For example, suppose U is equal to W, and V is set to zero. Using equation (8.2.7) it can be shown that the maximum path length is still approximately the same as the beam waist diameter (0.32 mm). If U is equal to V while V is zero, the maximum path length is roughly 70% of the beam waist diameter (0.22 mm).

The fringe count distribution for the 2-D case is very similar in nature to the simple 1-D prediction. The initial behavior is again linear with a slightly larger slope. The peak of the distribution function is also higher so there is a slight increase in the probability of lower fringe count

values. On the other hand, the tail of the distribution decays faster than in the 1-D case.

This behavior may be easily explained. Recall for the 1-D case that the maximum path length is constant and independent of the velocity value. This is not true for the 2-D case. As the velocity vector swings away from the x-axis to the y-axis, the path length decreases. The shorter path length results in a lower fringe count. The higher incidence of low fringe counts in the 2-D model may be attributed to this angular effect.

How well does theory agree with experimental results? Figure 8.4.3 demonstrates the contrast. The experimental data is computed from one of the single channel mode realizations (i.e. only one velocity component is recorded). For this case, the fringe plane is perpendicular to the jet axis. The data point location is $x/D = 67.25$ and $\eta = 0.09$. The measured mean velocity at this point is 2-3 meters/second with a local turbulence intensity level of 50%. The frequency shift is 300 kHz. The theoretical prediction is based on a 2-D flow field (equation 8.4.4) with the above characteristics. Considering the error induced by varying particle sizes as revealed in Figure 8.3.1, the agreement is very satifactory. Both experimental data and theoretical predictions clearly display an initial region of linear growth leading to a peak in the fringe count distribution. This trend is then followed by a

FIGURE 8.4.3

PROBABILITY DISTRIBUTION OF FRINGE COUNT
THEORETICAL AND EXPERIMENTAL RESULTS

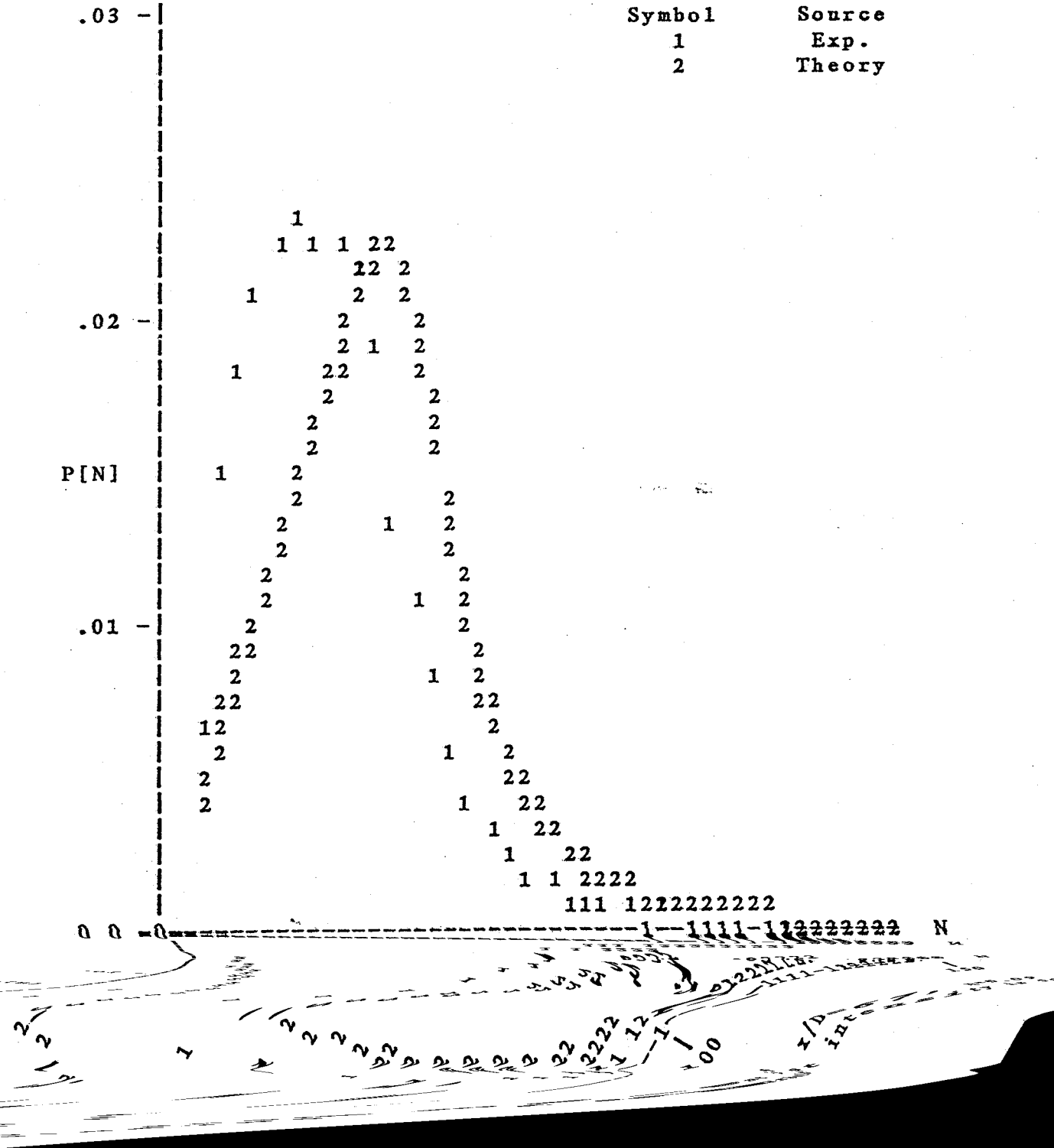

FIGURE 8.4.4

PROBABILITY DISTRIBUTION OF FRINGE COUNT
THEORETICAL AND EXPERIMENTAL RESULTS
REDUCTION OF MEASURING VOLUME IN NUMERICAL MODEL

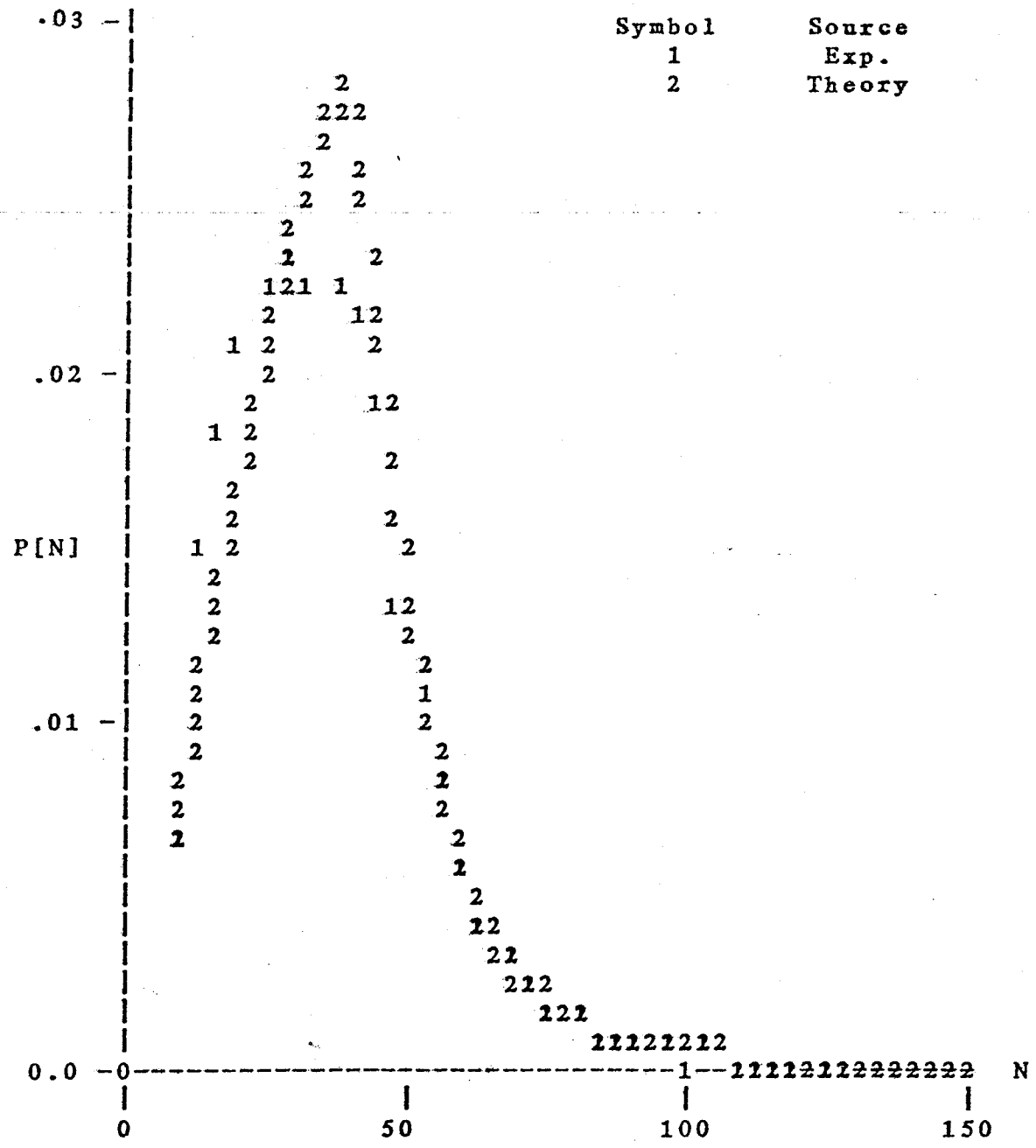

Location of experimental measurement is x/D=67, η=0.09 .
Mean velocity is 2.3 meters/sec, turbulent intensity is 50%.
Frequency shift is 300 kHz.
Beam waist diameter is reduced by 20% in theoretical model

gradual decay. The peak of the experimental results occurs at an earlier value and is wider then the model. This behavior can be attributed to the smaller particles seeing a smaller measuring volume size.

Results for the two channel mode are found in Figure 8.4.5. For these measurements, the line perpendicular to the fringe plane is at an angle of 45° with respect to the jet axis. The behavior of the fringe count distribution across the jet cross section is shown here. The same characteristics are displayed, with an initial linear behavior leading to a peak followed by gradual decay. The decrease in the mean velocity with increasing radial coordinate lowers the slope of the linear region and the peak of the distribution function. The increase in turbulence intensity with the radial coordinate spreads the distribution function. None of the results seem to indicate angular bias – there is not an unusually high incidence of low fringe counts.

An important departure from the general characteristics in the distribution is seen for the data set at the very edge of the jet. The eight bit binary counter which tracks the fringe crossings overflows on the 256th count and since the carry bit is lost the value of the fringe count effectively resets to zero. For example, the standard hardware is incapable of differentiating between eight fringes and 264 fringes! Due to the low mean velocities at

FIGURE 8.4.5

PROBABILITY DISTRIBUTION OF FRINGE COUNT
VARIATION ACROSS JET AXIS FOR TWO CHANNEL DATA

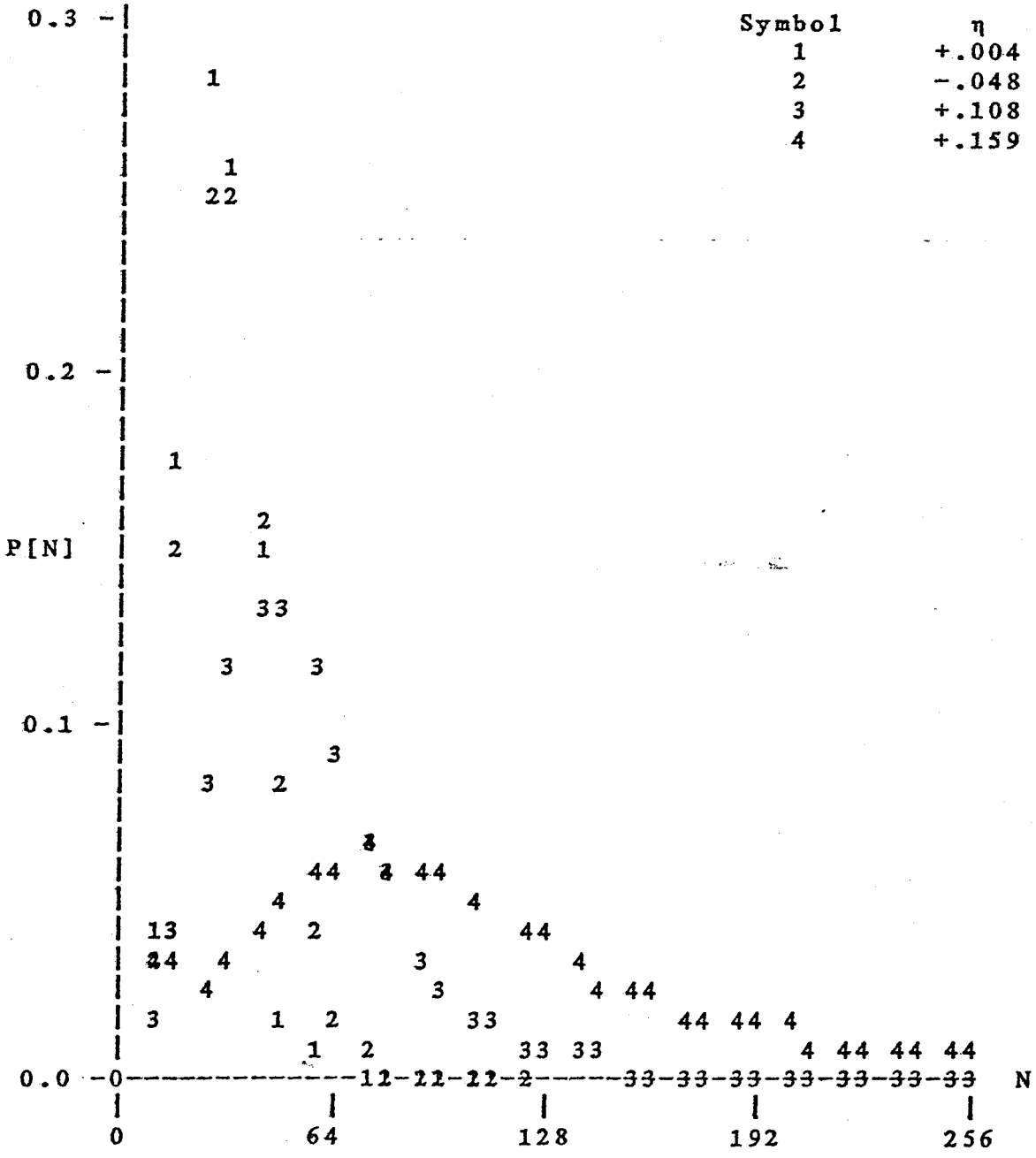

Axial coordinate is x/D=67 for all cases.

the outer edge of the jet, the distribution function clearly indicates a significant number of occurrences near the 256 count upper limit. Fringe counts above 255 are reflected back to lower values at the inner region of the distribution function. This is clearly highlighted in Figure 8.4.6.

It is simple to estimate the velocities at which overflow is expected. The maximum number of fringes a particle may encounter given the velocity vector has already been presented in equation (8.4.1). It is repeated here for convenience,

$$N_m = \frac{d_{xm}}{C} |1 + f_s/f_D| \qquad (8.4.5)$$

Obviously, as the Doppler frequency approaches zero, the fringe count becomes large. Figure 8.4.7 demonstrates how this function may be used to indicate the viable measurement zone of the counter. Given a velocity vector, the maximum path length, d_{xm}, is calculated using equation (8.2.7). As an example, suppose the velocity vector is aligned with the x-axis. Assume the beam waist diameter is .32 mm, the calibration factor is 11 meters/sec/MHz and the frequency shift is 400 kHz. Since at least eight fringes must be crossed, the lower limits of the measurement zone may be calculated by substituting eight into the left hand side of the above equation. For the above conditions the counter will correctly measure velocities down to -2.6 meters/second (point A). Any lower velocities (i.e. those

FIGURE 8.4.6

FRINGE COUNT OVERFLOW

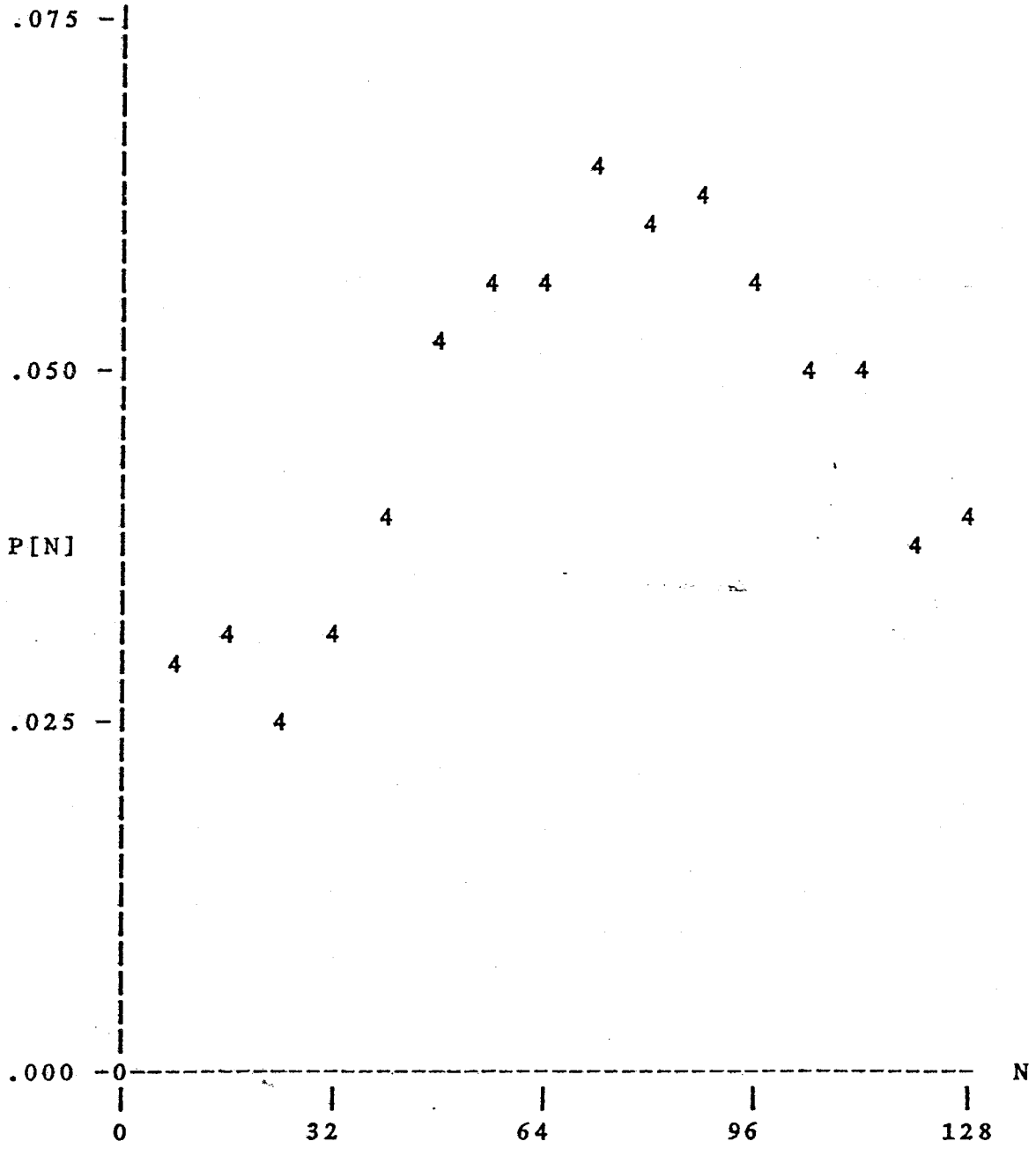

Coordinate location is x/D=67, η=0.16 .

FIGURE 8.4.7

FRINGE COUNT VS DOPPLER FREQUENCY

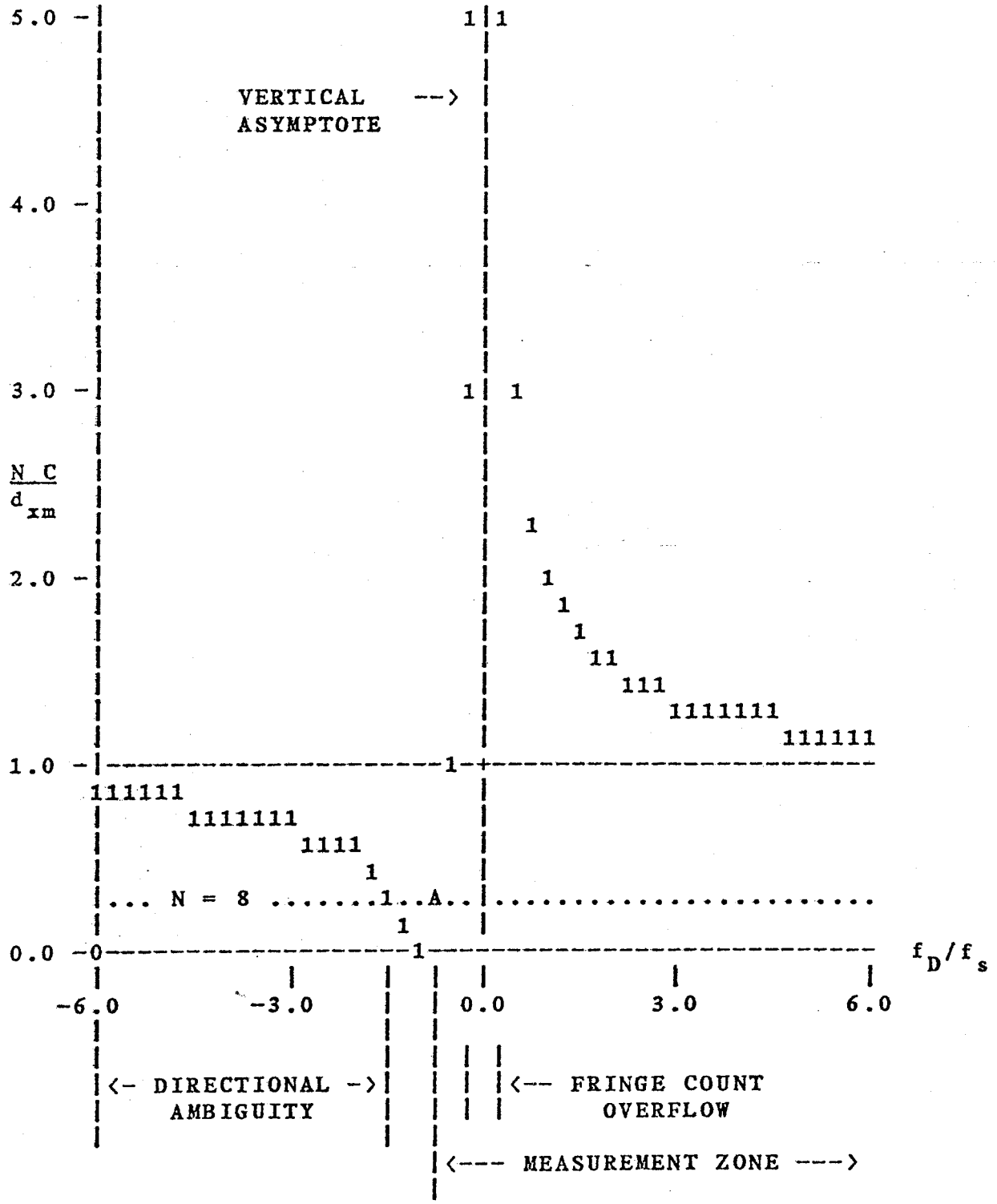

points to the left of A) are subject to directional uncertainty and will be interpreted by computer software as positive velocity vectors. The condition for fringe count overflow may also be evaluated using equation (8.4.5). A count of 256 cycles for the above values gives an overflow range from −56 cm/second to 44 cm/second.

Fringe count overflow does not affect the velocity estimate since this value is inversely proportional to the burst time for eight fringes, P_8, and independent of the fringe count, N. However, its immediate effect is to underestimate the residence time, P, since this value is computed using both the fringe count and the burst time for eight fringes, i.e.

$$P = N P_8/8 \qquad (8.4.6)$$

Because only the residence time is affected, this overflow condition is serious only in turbulent flows, for it is under these flow conditions that a reliable estimate of the residence is needed to avoid bias. Since the residence time for velocities near zero is underestimated, the weighting factor for these velocities is too small. The mean velocity will therefore be overestimated. Figures 8.4.5 and 8.4.6 indicate that fringe count overflow is a rare condition for the recorded data of the jet experiment and its effect on the calculated parameters of the flow field has been negligible.

In conclusion, it has been demonstrated that monitoring

the fringe count distribution function can provide very useful qualitative and quantitative information. First it can be used to estimate the measuring volume size seen by the particles. Second, it can also give warning of increased angular bias effects due to small particle sizes. Finally, it can indicate fringe count overflow and the resulting contamination of time averages using residence time weighting. The attractiveness of monitoring incoming data using the fringe count has an additional benefit since the fringe count is an integer value. Arithmetic operations on the computer are processed much faster then would occur when dealing with real values.

Section 8.5: Software Verification Techniques

In this section, possible software verification techniques are presented. Although offering little in the way of solid quantitative results, it is hoped future experience will show they can provide a qualitative guide by which the seeding density and noise characteristics of the LDA signal can be judged. Since this is the first experiment in which these tools have been applied, an accurate evaluation of their worth is not possible. This measurement program should be viewed as the first in a series of investigations to provide an empirical guide to interpreting their meaning.

In Section 7.3 it was shown how the statistical

dependence of the sampling process on the flow field can bias counter measurements when arithmetic averages are used in processing the data. It has been demonstrated that residence time weighting correctly processes the data without making any assumptions concerning arrival time statistics. The derivation of this technique only mandates that the particle seeding must be statistically uniform. As a secondary result of the derivation, it was shown that the average number of particles per unit volume was

$$\mu_c = \frac{1}{T_s V_{mv}} \sum P_i \qquad (8.5.1)$$

where μ_c is the number of particles per unit volume, T_s is the total length of time for the sampling period, V_{mv} is the measuring volume, and P_i the residence time for the ith realization. It must be emphasized that this is the particle concentration seen by the counter, and not necessarily the concentration in the fluid. This is because the measured value is sensitive both to the particle density in the fluid flow as well as the adjustment of the optical and counter hardware. In addition, if one were to obtain a quantitative value, the measuring volume must be known. The previous section's investigation into the fringe count probability distribution function has demonstrated the measuring volume's dependence on particle size. Because of these uncertainties, the above equation is useful only in a qualitative sense.

FIGURE 8.5.1

PARTICLE CONCENTRATION SEEN BY COUNTER

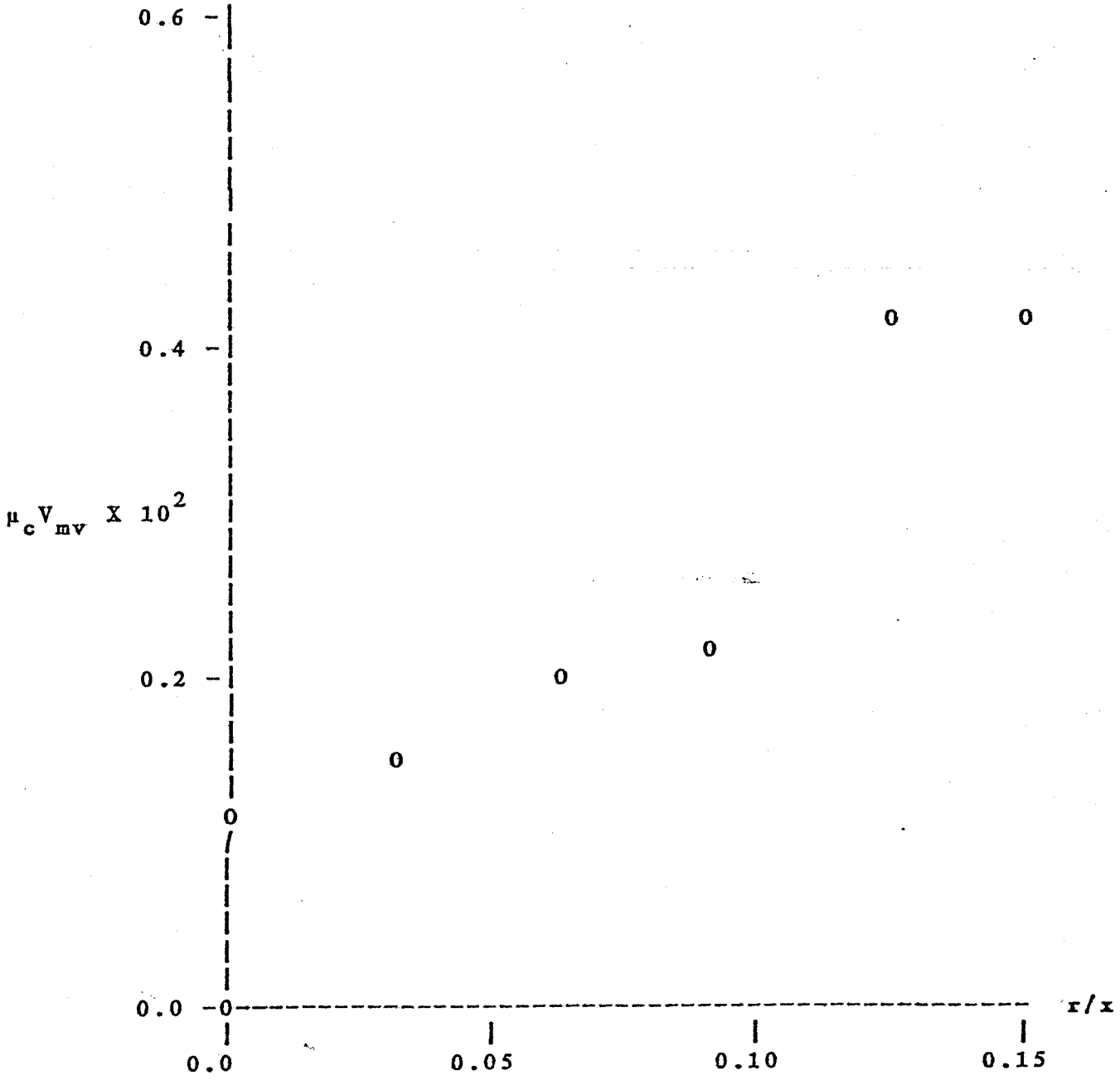

Measured values of the concentration across the profile are shown in Figure 8.5.1. Instead of expressing the concentration in terms of particles per unit volume, the percentage of time a particle is in the measuring volume is presented. This value is determined by shifting the measuring volume to the left hand side of equation (8.5.1). On an average, validated bursts occupy 0.2 % of the total sampling period. These data points were not taken simultaneously in time, so it is impossible to separate time and spatial variations. Although the jump at the outer edge is large on a relative basis, the difference is small when expressed as an absolute value. The low value for the concentration also indicates that the occurrence of multiple particles in the measuring volume was rare during the course of the experiment. Based on these results, it seems safe to assert that the enclosure was uniformly seeded.

Although the experimenter can frequently judge his signal quality by monitoring the Doppler signal on an oscilloscope, few have tried to present a feel for the signal quality of their measurements in their publications. It is for this reason that the two following parameters are proposed. They are to serve as a means for providing the reader with a feeling of how well the LDA system is tuned.

For a single channel system, the correlation coefficient between the velocity and residence time is defined as covariance between the residence time and the

velocity, σ_{PU}, normalized by the standard deviation of the residence time, σ_p, and the standard deviation of the velocity, σ_U, i.e.

$$\rho_p = \frac{\sigma_{PU}}{\sigma_p \sigma_U} \qquad (8.5.2)$$

The higher the velocity, the shorter the residence time, so the two values should be negatively correlated. Of course, a perfect correlation is unexpected since the residence time is a function of the velocity vector and the particle path. When plotted across the jet profile as shown in Figure 8.5.2, the value is fairly consistent at a value of -0.6. Recall the local turbulence intensity u/U in the jet was a minimum value of 27% at the jet centerline and rapidly increased with the radial coordinate to levels above 50% at η=0.10. The constant value for the correlation coefficient, ρ_{PU}, is very encouraging, since it implies the correlation coefficient is largely independent of turbulence intensity.

Dual channel systems present one additional possiblilty. For cases where the focal length is large, the measuring volumes of the two beams are nearly coincident. For these cases, it is expected that the residence time originating from each counter should be the same. As before, a correlation coefficient is defined, only this time the two variables are the residence times from each counter

$$\sigma_{P1P2}$$

FIGURE 8.5.2

RESIDENCE TIME - VELOCITY CORRELATION COEFFICIENT

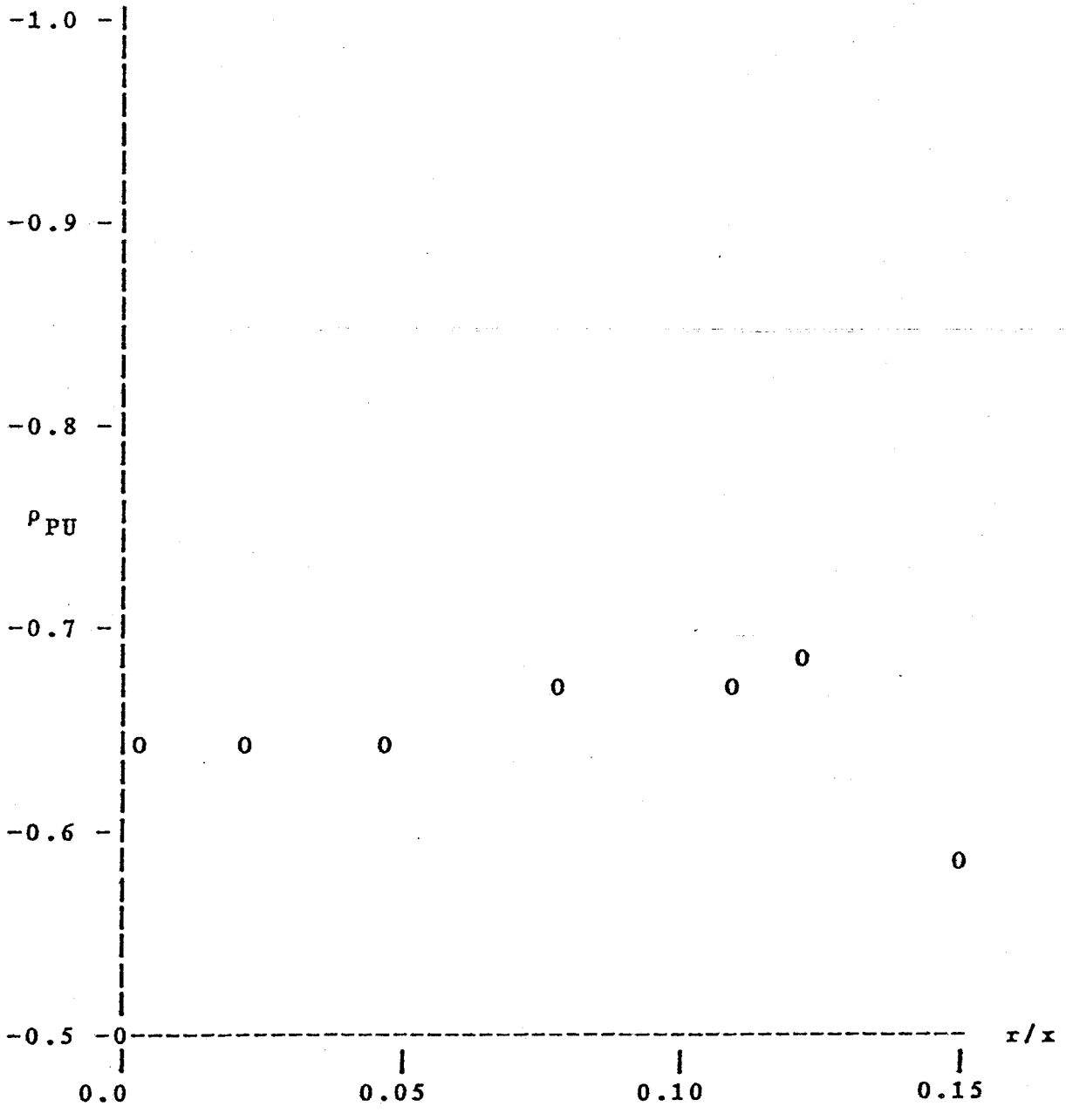

FIGURE 8.5.3

RESIDENCE TIME - RESIDENCE TIME CORRELATION COEFFICIENT

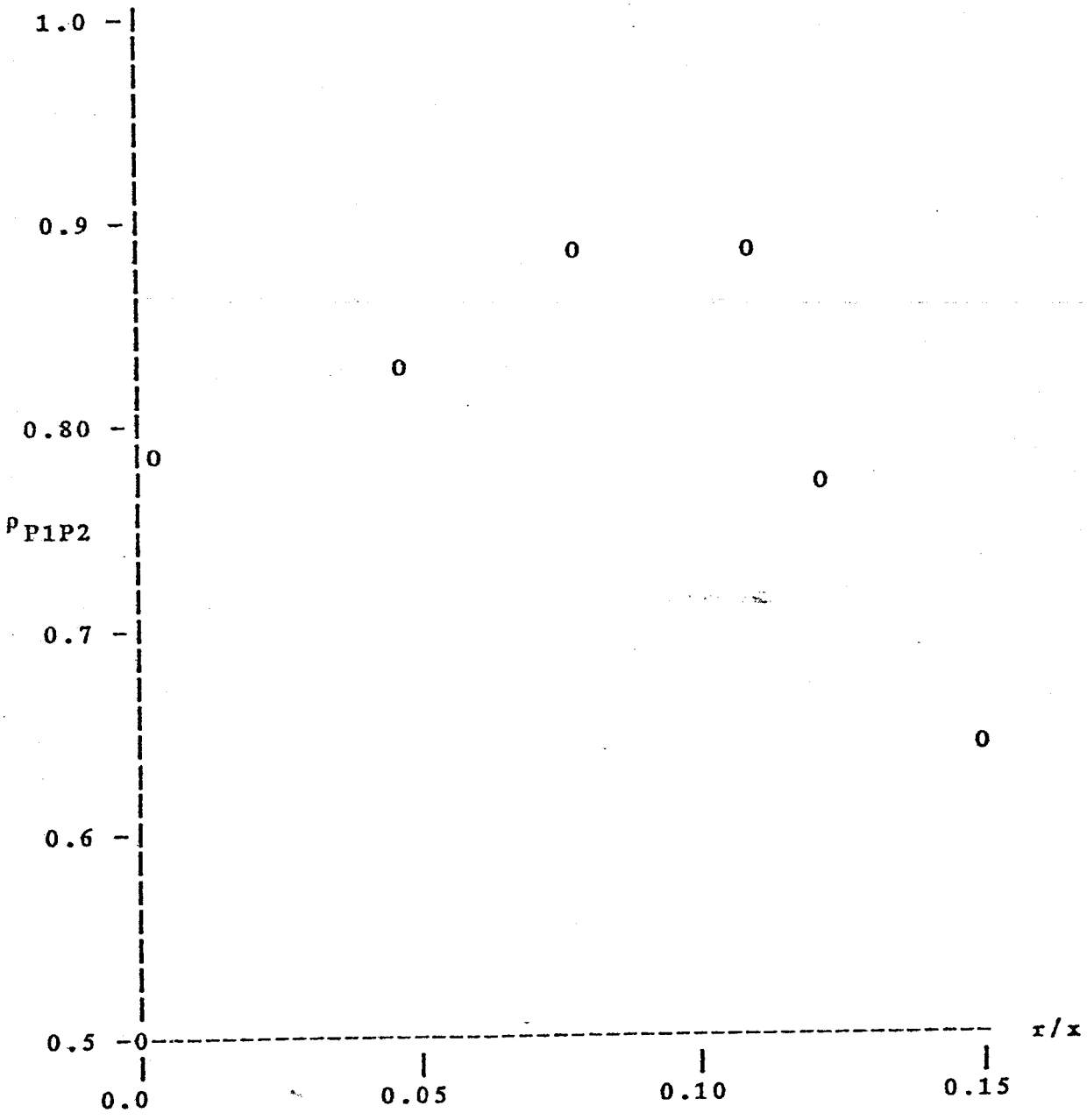

These values are seen to be highly correlated with a value between 0.8 to 0.9 across the profile, with a slight decrease at the outer edges. Again, it is difficult to draw conclusions since similar measurements in other flows are unavailable.

Section 8.6: Summary and Conclusions

The development in the second part of this dissertation has focused upon the correct use of the LDA burst processor. A derivation has been presented for the probabilty distribution function of the path length in a uniform velocity field. It was shown that the path length could easily be expressed in terms of the fringe count or residence time. The distribution function proved to be a straight line function, the larger values of the path length having a higher probabiltiy. This distribution function can be viewed as a conditional distribution function for use in a turbulent flow field. If one adopts a reduced measuring volume size to account for small particle effects, reasonable results can be produced. Unfortuantely, the calculation time is excessive for real time data acquisition and there is no way to predetermine a reliable measuring volume size.

The most serious consequence of this analysis is in terms of angular bias. Buchhave's equation for the measuring volume cross section (equation 7.4.3) is a

function of velocity vector, frequency shift, and measuring volume size. By measuring the probabiltiy distribution function of the path length in a laminar flow, it is possible to crudely determine the true measuring volume. This information can then be used to determine the appropriate frequency shift.

It is suggested that the fringe count is the better variable to use when computing the distribution function. Since it is an integer value, the computer can execute mathematical functions at a faster rate. Also, the fringe count has two other distinct advantages. The distribution function of the fringe count is the only way to detect the condition of fringe count overflow and the subsequent severe underestimate of the residence time (although it must be noted that this is a very rare case indeed). Secondly, a crude method of checking for the absence of angular bias is to ensure a high incidence of high fringe count in the LDA data. It is highly recommended that a data acquistion routine therefore compute in real time the distribution function of the fringe count. To ensure that the band-pass filters are correctly set, it is also recommended that the distribution function for the detected frequency (i.e. the signal input to the counter uncorrected for frequency shift) also be presented on a real time basis.

The correct method of data processing to avoid bias is residence time weighting. Practically speaking, this method

must be done in the batch mode with each batch covering a fixed length of time, not a fixed number of samples. Each batch should be separated in time by at least two flow integral scales. For further information on this technique, consult the references mentioned in section 7.3. For residence time averaging, both the residence time, P, and particle velocity, U, are required. These parameters are also those required to implement the software verification methods presented in section 8.5. There is no additional cost in program storage. The additional cost in processing time is insignificant, considering the useful information it can provide. Calculation of the effective particle concentration may be used to evaluate if the seeding is statistically uniform (required for residence time averaging). Correlation coefficients between the velocity and residence time (for single channel LDA) and the residence times from separate channels (for two channel LDA where the measuring volumes are coincident) may in the future provide a reasonable guide toward signal quality. The experimental results of this investigation indicate a good quality signal in a highly turbulent flow can be expected to have correlation coefficients with the following values

$$\sigma_{PU} = -0.6 \qquad \sigma_{P1P2} = 0.8 \rightarrow 0.9 \qquad (8.6.1)$$

It is hoped that these parameters may prove to be a useful tool in setting standards by which the scientific community

REFERENCES

Abbiss, J.B., Bradbury, J.S., and Wright, M.P. (1975). 'Measurements on an Axi-Symmetric Jet Using a Photon Correlator, The Accuracy of Flow Measurements by Laser Doppler Methods'. Proceedings LDA-Symposium, Copenhagen, 319-335.

Adrian, R.J., and Orloff, K.L. (1977). 'Laser Anemometer Signals: Visibility Characteristics and Application to Particle Sizing'. Applied Optics, Vol. 16, pp. 677-684.

Adrian, R.J. (1979). 'Estimation of LDA Signal Strength and Signal- to-Noise Ratio'. TSI Quart., Vol. 5 pp. 3-8.

Adrian, R.J. (1980). 'Laser Velocimetry'. T.A.M. Report No. 442, Dept. Theor. and Appl. Mech., Univ. of Ill. at Urbana-Champaign.

Agarawal, J.K. and Keady, P. (1980). 'Theoretical Calculation and Experimental Observation of Laser Velocimeter Signal Quality'. TSI Quart., Vol. 6, pp. 3-10.

Baker, C.B. (1980). 'An Analysis of the Turbulent Buoyant Jet'. Ph.D. Dissertation, Pennsylvania State University.

Beuther, P.D. (1980) 'Experimental Investigation of the Turbulent Buoyant Axisymmetric Plume', Ph.D. Dissertation, State University of New York at Buffalo, June 1980.

Brockmann, E. (1979). 'Computer Simulation of Laser Velocimeter Signals'. Laser Velocimetry and Particle Sizing, Proceedings of the Third International Workshop on Laser Velocimetry, July 11-13, 1978, Purdue Univ., Hemisphere Publishing, New York.

Buchhave, P. (1976). 'Biasing Errors in Individual Particle Measurements with the LDA-Counter Signal Processor.' In Proc. LDA Symp., Copenhagen, 1975, 258-78.

Buchhave, P. (1979). 'The Measurement of Turbulence with the Burst-Type Laser Doppler Anenmmeter - Errors and Correction Methods'. Ph.D. Dissertation, State University of New York at Buffalo.

Buchhave, P., Geroge, W.K., Jr., Lumley, J.L. (1979). 'The Measurement of Turbulence with the Laser-Doppler Anemometer'. Annual Review of Fluid Mech., V. 11, 443-503, Annual Reviews, Inc., Palo Alto, Calif.

Champagne, F.H. (1978). 'The Fine-Scale Structure of the Turbulent Velocity Field'. J.F.M., Vol. 86, pp. 67-108.

Corrsin, S. (1943). Natl. Advisory Comm. Aeronaut. Wartime Repts., No. 94.

Corrsin, S., and Uberoi, M.S. (1949). Natl. Advisory Comm. Aeronaut. Tech. Notes, No. 1865.

Corrsin, S., and Uberoi, M.S. (1950). Natl. Advisory Comm. Aeronaut. Tech. Notes, No. 2124.

Corrsin, S., and Kistler, A.L. (1954). Natl. Advisory Comm. Aeronaut. Tech. Notes, No. 3133. Durst, F., Melling, A., Whitelaw, J.H. (1976). 'Principles and Practice of Laser-Doppler Anemometry'. New York: Academic Press.

Erdmann, J.C. and Gellert, R.I. (1976). 'Particle arrival Statistics in Turbulent Flow.' Appl. Phys. Letters, Vol 29, pp. 408-411.

Farmer, W.M. (1972). 'Measurement of Particle Size, Number Density and Velocity Using a Laser Interferometer'. Appl. Optics, Vol. 11, pp.2603-2609.

George, W.K. (1976) 'Limitations to Measuring Accuracy Inherent in the Laser Doppler Signal' The Accuracy of Flow Measurements by Laser Doppler Methods, Proc. LDA Symp. Copenhagen 1975, 20,63.

George, W.K., (1978) 'Processing of Random Signals', in Dynamic Meas. in Unsteady Flows, Proc. Dyn. Flow Conf. 1978, (PO Box 121, DK-2740 Skovlunde, Denmark), p. 757-800.

George, W.K., Seif, A.A. and Baker, C.B. (1982) 'Momentum Balance Considerations in Axisymmetric Turbulent Jets', Rept. No. TRL-119, Turbulence Research Laboratory, SUNY/Buffalo.

Greated, C.A. and Durrani, T.S. (1977). 'Laser Systems in Flow Measurement'. Plenum Press, New York.

Hinze, J.O., and B.G. van der Hegge Zijnen (1949). 'Transfer of Heat and Matter in the Turbulent Mixing Zone of an Axially Symmetrical Jet'. Appl. Sci. Research, V. 1A, 435-461.

Hinze, J.O. (1975, 2nd Ed.). 'Turbulence'. McGraw-Hill, Inc.

Hussain, AMKF (1981) Private communication.

Khwaja, M.S.S. (1980). 'Ivestigation of the Turbulent Axisymmetric Jet Mixing Layer'. M.S. Thesis, SUNY at Buffalo.

Morel, T. (1975). 'Comprehensive Design of Axisymmetric Wind Tunnel Contractions'. J. Fluids Eng. ASME Trans. Sect. I, V. 97 2, 225-233.

McLaughlin, P.K. and Tiedeman, W.G. (1973) 'Biasing Correction for Individual Realization Laser Anemometer Measurement in Turbulent Flows, Phys. Flds., 16, 12, 2082-2088.

Nee, N. (1983). 'Turbulence Measurements in an Axisymmetric Jet Using a LDA'. M.S. Thesis, SUNY at Buffalo.

Reed, X.B., Spiegel, L., and Hartland, S. (1977). 'Some Measurements of Spatial Correlations in an Axisymmetric Turbulent Jet'. Proc. Symp. on Turbulent Shear Flows. Penna. State Univ., College Park, Pa., 223-232.

Reichardt, H. (1951, 2nd Ed.). Forsch. Gebiete Ingenieurw., No. 414.

Roberds, D.W. (1977). 'Particle Sizing Using Laser Interferometry'. Appl. Optics, Vol. 16, pp. 1861-1865.

Robinson, D.M. and Chu, W.P. (1975). 'Diffraction Analysis of Doppler Signal Characteristics For a Cross Beam Laser Doppler Velocimeter'. Appl. Optics, Vol. 14, pp. 2177-2181.

Rodi, W. (1975). 'New Method of Analyzing Hot-Wire Signals in Highly Turbulent Flow and its Evaluation in Round Jets'. Disa Information No. 17.

Rudd, M.J. (1969). 'A New Theoretical Model for the Laser Doppler Meter'. J. Phys. E. Sci. Instrum., Vol. 4, pp. 723-726.

Schlichting, H. (1968, 6th Ed.). 'Boundary-Layer Theory'. McGraw-Hill, Inc.

Seif, A.A. (1981). 'Higher Order Closure Model for Turbulent Jets'. Ph.D. Thesis, SUNY at Buffalo.

Tan-Atichat, J. (1980) 'Effects of Axisymmetric Contractions on Turbulence of Various Scales'. Ph.D. Thesis, IIT.

Tennekes, H. and Lumley, J.L. (1972). 'A First Course in Turbulence'. M.I.T. Press.

Tennekes, H. and Sygnanski, J.C. (1972) 'The Intermittent Small Scale Structure of Turbulence: Data Processing Hazards, JFM, 55, 1, 93.

Tutu, N.K. and Chevray, R. (1975) Cross-wire Anemometry in High Intensity Turbulence, JFM, 71, 785.

Wygnanski, I., Fiedler, H.E. (1969). 'Some Measurements in the Self-Preserving Jet'. J. Fluid Mech. 38, 577-612.

REFERENCES

Abbiss, J.B., Bradbury, J.S., and Wright, M.P. (1975). 'Measurements on an Axi-Symmetric Jet Using a Photon Correlator, The Accuracy of Flow Measurements by Laser Doppler Methods'. Proceedings LDA-Symposium, Copenhagen, 319-335.

Adrian, R.J., and Orloff, K.L. (1977). 'Laser Anemometer Signals: Visibility Characteristics and Application to Particle Sizing'. Applied Optics, Vol. 16, pp. 677-684.

Adrian, R.J. (1979). 'Estimation of LDA Signal Strength and Signal- to-Noise Ratio'. TSI Quart., Vol. 5 pp. 3-8.

Adrian, R.J. (1980). 'Laser Velocimetry'. T.A.M. Report No. 442, Dept. Theor. and Appl. Mech., Univ. of Ill. at Urbana-Champaign.

Agarawal, J.K. and Keady, P. (1980). 'Theoretical Calculation and Experimental Observation of Laser Velocimeter Signal Quality'. TSI Quart., Vol. 6, pp. 3-10.

Baker, C.B. (1980). 'An Analysis of the Turbulent Buoyant Jet'. Ph.D. Dissertation, Pennsylvania State University.

Beuther, P.D. (1980) 'Experimental Investigation of the Turbulent Buoyant Axisymmetric Plume', Ph.D. Dissertation, State University of New York at Buffalo, June 1980.

Brockmann, E. (1979). 'Computer Simulation of Laser Velocimeter Signals'. Laser Velocimetry and Particle Sizing, Proceedings of the Third International Workshop on Laser Velocimetry, July 11-13, 1978, Purdue Univ., Hemisphere Publishing, New York.

Buchhave, P. (1976). 'Biasing Errors in Individual Particle Measurements with the LDA-Counter Signal Processor.' In Proc. LDA Symp., Copenhagen, 1975, 258-78.

Buchhave, P. (1979). 'The Measurement of Turbulence with the Burst-Type Laser Doppler Anenmmeter - Errors and Correction Methods'. Ph.D. Dissertation, State University of New York at Buffalo.

Buchhave, P., Geroge, W.K., Jr., Lumley, J.L. (1979). 'The Measurement of Turbulence with the Laser-Doppler Anemometer'. Annual Review of Fluid Mech., V. 11, 443-503, Annual Reviews, Inc., Palo Alto, Calif.

Champagne, F.H. (1978). 'The Fine-Scale Structure of the Turbulent Velocity Field'. J.F.M., Vol. 86, pp. 67-108.

Corrsin, S. (1943). Natl. Advisory Comm. Aeronaut. Wartime Repts., No. 94.

Corrsin, S., and Uberoi, M.S. (1949). Natl. Advisory Comm. Aeronaut. Tech. Notes, No. 1865.

Corrsin, S., and Uberoi, M.S. (1950). Natl. Advisory Comm. Aeronaut. Tech. Notes, No. 2124.

Corrsin, S., and Kistler, A.L. (1954). Natl. Advisory Comm. Aeronaut. Tech. Notes, No. 3133. Durst, F., Melling, A., Whitelaw, J.H. (1976). 'Principles and Practice of Laser-Doppler Anemometry'. New York: Academic Press.

Erdmann, J.C. and Gellert, R.I. (1976). 'Particle arrival Statistics in Turbulent Flow.' Appl. Phys. Letters, Vol 29, pp. 408-411.

Farmer, W.M. (1972). 'Measurement of Particle Size, Number Density and Velocity Using a Laser Interferometer'. Appl. Optics, Vol. 11, pp.2603-2609.

George, W.K. (1976) 'Limitations to Measuring Accuracy Inherent in the Laser Doppler Signal' The Accuracy of Flow Measurements by Laser Doppler Methods, Proc. LDA Symp. Copenhagen 1975, 20,63.

George, W.K., (1978) 'Processing of Random Signals', in Dynamic Meas. in Unsteady Flows, Proc. Dyn. Flow Conf. 1978, (PO Box 121, DK-2740 Skovlunde, Denmark), p. 757-800.

George, W.K., Seif, A.A. and Baker, C.B. (1982) 'Momentum Balance Considerations in Axisymmetric Turbulent Jets', Rept. No. TRL-119, Turbulence Research Laboratory, SUNY/Buffalo.

Greated, C.A. and Durrani, T.S. (1977). 'Laser Systems in Flow Measurement'. Plenum Press, New York.

Hinze, J.O., and B.G. van der Hegge Zijnen (1949). 'Transfer of Heat and Matter in the Turbulent Mixing Zone of an Axially Symmetrical Jet'. Appl. Sci. Research, V. 1A, 435-461.

Hinze, J.O. (1975, 2nd Ed.). 'Turbulence'. McGraw-Hill, Inc.

Hussain, AMKF (1981) Private communication.

Khwaja, M.S.S. (1980). 'Ivestigation of the Turbulent Axisymmetric Jet Mixing Layer'. M.S. Thesis, SUNY at Buffalo.

Morel, T. (1975). 'Comprehensive Design of Axisymmetric Wind Tunnel Contractions'. J. Fluids Eng. ASME Trans. Sect. I, V. 97 2, 225-233.

McLaughlin, P.K. and Tiedeman, W.G. (1973) 'Biasing Correction for Individual Realization Laser Anemometer Measurement in Turbulent Flows, Phys. Flds., 16, 12, 2082-2088.

Nee, N. (1983). 'Turbulence Measurements in an Axisymmetric Jet Using a LDA'. M.S. Thesis, SUNY at Buffalo.

Reed, X.B., Spiegel, L., and Hartland, S. (1977). 'Some Measurements of Spatial Correlations in an Axisymmetric Turbulent Jet'. Proc. Symp. on Turbulent Shear Flows, Penna. State Univ., College Park, Pa., 223-232.

Reichardt, H. (1951, 2nd Ed.). Forsch. Gebiete Ingenieurw., No. 414.

Roberds, D.W. (1977). 'Particle Sizing Using Laser Interferometry'. Appl. Optics, Vol. 16, pp. 1861-1865.

Robinson, D.M. and Chu, W.P. (1975). 'Diffraction Analysis of Doppler Signal Characteristics For a Cross Beam Laser Doppler Velocimeter'. Appl. Optics, Vol. 14, pp. 2177-2181.

Rodi, W. (1975). 'New Method of Analyzing Hot-Wire Signals in Highly Turbulent Flow and its Evaluation in Round Jets'. Disa Information No. 17.

Rudd, M.J. (1969). 'A New Theoretical Model for the Laser Doppler Meter'. J. Phys. E. Sci. Instrum., Vol. 4, pp. 723-726.

Schlichting, H. (1968, 6th Ed.). 'Boundary-Layer Theory'. McGraw-Hill, Inc.

Seif, A.A. (1981). 'Higher Order Closure Model for Turbulent Jets'. Ph.D. Thesis, SUNY at Buffalo.

Tan-Atichat, J. (1980) 'Effects of Axisymmetric Contractions on Turbulence of Various Scales'. Ph.D. Thesis, IIT.

Tennekes, H. and Lumley, J.L. (1972). 'A First Course in Turbulence'. M.I.T. Press.

Tennekes, H. and Sygnanski, J.C. (1972) 'The Intermittent Small Scale Structure of Turbulence: Data Processing Hazards, JFM, 55, 1, 93.

Tutu, N.K. and Chevray, R. (1975) Cross-wire Anemometry in High Intensity Turbulence, JFM, 71, 785.

Wygnanski, I., Fiedler, H.E. (1969). 'Some Measurements in the Self-Preserving Jet'. J. Fluid Mech. 38, 577-612.